

CRANFIELD UNIVERSITY

FALIANG WANG

THE COMPARISON OF AERODYNAMIC AND STABILITY
CHARACTERISTICS BETWEEN CONVENTIONAL AND BLENDED
WING BODY AIRCRAFT

SCHOOL OF ENGINEERING
MSc by Research

MSc by Research
Academic Year: 2011 - 2012

Supervisor: Prof Howard Smith
January 2012

CRANFIELD UNIVERSITY

SCHOOL OF ENGINEERING
MSc by Research

MSc by Research

Academic Year 2011 - 2012

FALIANG WANG

THE COMPARISON OF AERODYNAMIC AND STABILITY
CHARACTERISTICS BETWEEN CONVENTIONAL AND BLENDED
WING BODY AIRCRAFT

Supervisor: Prof Howard Smith
January 2012

© Cranfield University 2012. All rights reserved. No part of this
publication may be reproduced without the written permission of the
copyright owner.

ABSTRACT

Aircraft with advanced wing geometry, like the flying wing or blended wing body configuration, seems to be the seed candidate of future aircraft. Compared with conventional aircraft, there are significant aerodynamic performance improvements because of its highly integrated wing and fuselage configuration. On the other hand, due to its tailless configuration, the stability characteristics are not as good as conventional aircraft.

The research aims to compare the aerodynamic and stability characteristics of conventional, flying wing and blended wing body aircraft. Based on the same requirement—250 passenger capability and 7,500 nautical miles range, three different configurations—conventional, flying wing and blended wing body options were provided to make direct comparison.

The research contains four parts. In the first part, the aerodynamic characteristics were compared using empirical equation ESDU datasheet and Vortex-Lattice Method based AVL software. In the second part, combined with the aerodynamic data and output mass data from other team member, the stability characteristics were analysed. The stability comparison contains longitudinal, lateral-directional static stability and dynamic stability. In the third part, several geometry parameters were varied to investigate the influence on the aerodynamic and stability characteristics of blended wing body configuration. In the last part, a special case has been explored in an attempt to improve the static stability by changing geometry parameters. The process shows that the design of blended wing body is really complex since the closely coupling of several parameters.

Keywords:

ESDU, AVL, tailless configuration, geometry parameter, influence.

ACKNOWLEDGEMENTS

Over the Year from Feb, 2011 to Feb, 2012, I have been fortune to study in School of Engineering, Cranfield University. My education in Cranfield University is sponsored by AVIC and China Scholarship Council. Thanks for providing me this valuable opportunity.

Sincerely thanks to my supervisor Prof.Howard Smith, for his valuable instructions, inspiring guidance, and encouragement to me during the research.

I would also appreciate Prof.John Fielding, Mr P.Stocking, Dr.Shijun Guo,Dr Craig Lawson,Dr Helen Lockett and other staff in School of Engineering for their advices and discussions during the Group Design.

I also consider my lucky to study with my colleagues and classmates.

A special acknowledge goes to Matylda and Jonathan for their kindly help. I really cherish the friendship.

I am extremely grateful to my family members for their constant support. I can always feel your love to inspire me to get through all the difficulties. I love you, ever and forever!

TABLE OF CONTENTS

ABSTRACT	i
ACKNOWLEDGEMENTS.....	iii
LIST OF FIGURES.....	ix
LIST OF TABLES	xiii
LIST OF EQUATIONS.....	xvii
LIST OF ABBREVIATIONS.....	xxi
1 Introduction.....	1
1.1 Research Process.....	1
1.1.1 The Group Design Project (GDP).....	1
1.1.2 The Individual Research Project (IRP)	2
1.2 Objectives	3
1.3 Thesis structure	4
2 Literature Review	7
2.1 Review of history of tailless aircraft.....	7
2.2 Aerodynamic studies of tailless aircraft.....	10
2.3 Stability studies of tailless aircraft	13
2.3.1 Longitudinal stability	13
2.3.2 Lateral-directional stability	13
2.3.3 Flying quality requirements	13
2.4 Geometry parameter influence	15
2.5 Summary	17
3 Methodology.....	19
3.1 Aerodynamic force calculation	19
3.1.1 Lift	21
3.1.2 Drag	23
3.2 Stability calculation	27
3.2.1 Longitudinal stability calculation	27
3.2.2 Lateral-directional stability calculation	29
3.3 Support tools.....	30
3.3.1 ESDU	30
3.3.2 AVL	30
3.3.3 XFLR	30
3.4 Research flow chart	32
4 Validation.....	33
4.1 Mesh number	33
4.1.1 Case introduction	33
4.1.2 Case setting	34
4.1.3 Results and discussion.....	35
4.2 Mesh distribution.....	36
4.2.1 Case introduction	36

4.2.2 Case setting	37
4.2.3 Results and discussion.....	38
4.3 Sweep.....	39
4.3.1 Case introduction	39
4.3.2 Case setting	40
4.3.3 Results and discussion.....	41
4.4 Twist	42
4.4.1 Case introduction	42
4.4.2 Case setting	43
4.4.3 Results and discussion.....	43
4.5 Stability calculation	45
4.5.1 Case introduction	45
4.5.2 Case setting	46
4.5.3 Result and discussion	46
4.6 Summary of validation	47
5 Model Description.....	49
5.1 Conventional configuration--CB	49
5.1.1 Three-view drawing.....	49
5.1.2 Geometry parameter	49
5.1.3 Mass and CG data	51
5.2 Flying Wing configuration--FW.....	52
5.2.1 Three-view drawing of FW	52
5.2.2 Geometry parameter	53
5.2.3 Mass and CG data	55
5.3 Blended Wing Body configuration--BWB	56
5.3.1 Wing geometry	56
5.3.2 Geometry parameter	57
5.3.3 Mass and CG data	59
5.4 AVL models	60
5.5 Summary	61
6 Aerodynamic Characteristics Comparison.....	63
6.1 Lift.....	63
6.2 Drag.....	64
6.3 Pitching moment.....	66
6.4 Aerodynamic derivatives.....	68
6.5 Summary	71
7 Stability Characteristics Comparison.....	73
7.1 Calculation condition.....	73
7.2 Longitudinal static stability characteristics	73
7.2.1 Static margin	73
7.2.2 Trim.....	75
7.3 Longitudinal dynamic stability characteristics	79

7.3.1 Phugoid mode	79
7.3.2 Short period mode.....	80
7.4 Lateral-Directional static stability characteristics.....	81
7.4.1 Lateral static stability	81
7.4.2 Directional Static stability	82
7.5 Lateral-Directional dynamic stability Characteristics	83
7.5.1 Dutch roll mode	83
7.5.2 Roll mode	84
7.5.3 Spiral mode	85
7.6 Summary	85
8 Parameter Influence on The Aerodynamic and Stability Characteristics of BWB Configuration.....	87
8.1 Influence of twist	87
8.2 Influence of sweep angle	92
8.3 Summary	94
9 Improve Static Margin Through Changing Parameters	97
9.1 Introduction	97
9.2 Iteration steps	97
9.2.1 Step 1: change sweep angle	98
9.2.2 Step 2: check trim ability	99
9.2.3 Step 3: arrange the twist	103
9.3 Other concerns	105
9.4 Summary	106
10 Conclusions and Suggestions	107
10.1 Conclusions of present work.....	107
10.2 Limitation of present research.....	108
10.3 Suggestions of future work	109
REFERENCES.....	111
APPENDICES	117
APPEXDIX REFERENCES	131

LIST OF FIGURES

Figure 1-1 Conventional configuration ^[1] (Unit:m)	1
Figure 1-2 Flying wing configuration ^[1]	2
Figure 1-3 Blended wing body configuration ^[3]	3
Figure 2-1 Aircraft classification by Lippisch ^[4]	7
Figure 2-2 Northrop YB-49 ^[6]	8
Figure 2-3 Integrated Wing Body of TsAGI ^[7]	8
Figure 2-4 BWB of Boeing ^[8]	9
Figure 2-5 B-2 Spirit Bomber ^[10]	9
Figure 2-6 Reflex camber airfoil	11
Figure 2-7 Supercritical airfoil.....	12
Figure 2-8 Wing parameters ^[22]	16
Figure 2-9 13 different wing planforms ^[22]	16
Figure 2-10 the aspect ratio influence on mean lift ^[22]	17
Figure 3-1 The horseshoe vortex layout (classical VLM method) ^[52]	20
Figure 3-2 PG correction factor	22
Figure 3-3 Wing geometry parameter.....	31
Figure 3-4 XFLR interface with AVL	31
Figure 3-5 Research flow chart	32
Figure 4-1 2D flat plate (Unit:m)	33
Figure 4-2 Different mesh density	34
Figure 4-3 2D Cp of different mesh number compare to theory value.....	35
Figure 4-4 Warren 12 planform (Unit:m).....	36
Figure 4-5 Uniform and cosine distribution ^[25] (1).....	37
Figure 4-6 Uniform(left) and cosine (right) distribution (2)	38
Figure 4-7 0 sweep and 35 sweep wing configuration (Unit:ft)	39
Figure 4-8 0 sweep and 35 sweep wing AVL model.....	40
Figure 4-9 NACA1422 wing planform ^[35]	42
Figure 4-10 NACA1422 model for AVL	43

Figure 4-11 Lift distribution curve	44
Figure 4-12 Lift coefficient versus alpha (angle of attack) curve.....	44
Figure 4-13 Sailplane AVL simulation	46
Figure 5-1 Three-view drawing of CB ^[1] (Unit:m).....	49
Figure 5-2 NACA SC2-0714	50
Figure 5-3 NACA SC2-0610	51
Figure 5-4 Internal arrangement of CB ^[3]	51
Figure 5-5 Three-view drawing of FW ^[1]	52
Figure 5-6 Wing geometry of FW ^[3] (Unit:m)	53
Figure 5-7 NASA SYM SC.....	54
Figure 5-8 NASA RC-SC2	55
Figure 5-9 Internal arrangement of FW ^[3]	55
Figure 5-10 Wing geometry of BWB ^[3]	57
Figure 5-11 Eppler 332 airfoil	58
Figure 5-12 NASA SC (2) 0010 airfoil	58
Figure 5-13 Internal arrangement of BWB ^[3]	59
Figure 5-14 Conventional AVL model.....	60
Figure 5-15 Flying wing AVL model.....	61
Figure 5-16 Blended wing body AVL model	61
Figure 6-1 Drag Polar	66
Figure 6-2 C_M-C_L curve.....	67
Figure 7-1 Elevator deflection angle (Forward CG, Ma=0.82)	76
Figure 7-2 Elevator deflection angle (Forward CG, Ma=0.2)	77
Figure 7-3 Elevator deflection angle (Aft CG, Ma=0.82).....	78
Figure 7-4 Elevator deflection angle (Aft CG, Ma=0.2).....	79
Figure 7-5 Lateral static stability	82
Figure 7-6 Directional static stability	83
Figure 8-1 Twist angle through the spanwise	90
Figure 8-2 Elliptic lift distribution	90

Figure 8-3 Triangle lift distribution	91
Figure 8-4 Different sweep angle models	93
Figure 9-1 Three sweep angles.....	98
Figure 9-2 Elevator deflection angle (Forward CG, Ma=0.82)	100
Figure 9-3 Elevator deflection angle (Aft CG, Ma=0.82).....	101
Figure 9-4 Elevator deflection angle (Forward CG, Ma=0.2)	102
Figure 9-5 Elevator deflection angle (Aft CG, Ma=0.2).....	103
Figure 9-6 Spanwise lift distribution of different twists.....	105
Figure Appendix -1 Wing sections and start point of each section	118
Figure Appendix -2 Inboard and outboard airfoil	119
Figure Appendix -3 Spanwise twist and thickness ratio variation	119
Figure Appendix -4 Spanwise lift distribution.....	120

LIST OF TABLES

Table 2-1 Short period mode damping ratio requirement ^[21]	14
Table 2-2 Phugoid mode damping ratio requirement ^[21]	14
Table 2-3 Dutch roll mode frequency and damping requirement ^[21]	15
Table 2-4 Roll mode time constant requirement ^[21] (Unit: s)	15
Table 2-5 Spiral mode minimum double amplitude time requirement ^[21] (Unit: s)	15
Table 3-1 Mach number PG correction	22
Table 4-1 2D flat plate parameter.....	34
Table 4-2 Simulation condition	35
Table 4-3 Warren 12 geometry parameter	36
Table 4-4 Mesh distribution methodology.....	37
Table 4-5 Comparison between calculation and theoretical data	38
Table 4-6 Wing geometry parameter	40
Table 4-7 Simulation condition	41
Table 4-8 Summary of 0 leading sweep angle wing	41
Table 4-9 Summary of 35 leading sweep angle wing	42
Table 4-10 Different twist and dihedral of three wings.....	43
Table 4-11 Parameters of sailplane ^[36]	45
Table 4-12 Simulation condition ^[36]	46
Table 4-13 Eigen roots and related modes ^[36]	47
Table 5-1 Geometry parameters	50
Table 5-2 Mass, moments of inertia and CG of CB ^[3]	52
Table 5-3 Geometry parameters	53
Table 5-4 Mass, moments of inertia and CG for FW ^[3]	56
Table 5-5 Geometry parameters	57
Table 5-6 Mass, moments of inertia and CG for BWB ^[3]	59
Table 6-1 Lift curve slope of different Mach number (unit: rad ⁻¹)	63
Table 6-2 Zero lift angle of attack of different Mach number	63

Table 6-3 Lift coefficient	64
Table 6-4 Form drag and wave drag at Mach 0.82.....	65
Table 6-5 Lift to drag ratio on cruise condition.....	66
Table 6-6 Zero lift pitching moment and $CM - CL$ slope.....	68
Table 6-7 Aerodynamic derivatives data of CB at different Mach numbers	68
Table 6-8 Aerodynamic derivatives data of FW at different Mach numbers	69
Table 6-9 Aerodynamic derivatives data of BWB at different Mach numbers...	69
Table 7-1 Mass, CG and moments of inertia	73
Table 7-2 CG position and static margin of CB ^[3]	74
Table 7-3 Static margin of FW ^[3]	75
Table 7-4 Static margin of BWB ^[3]	75
Table 7-5 Phugoid mode damping ratio and frequency	80
Table 7-6 Short period mode damping ratio and frequency	80
Table 7-7 Dutch roll mode damping ratio and frequency	84
Table 7-8 Roll mode time constants	84
Table 7-9 Spiral mode stability judgement	85
Table 8-1 Elliptic lift distribution	89
Table 8-2 Triangle lift distribution	89
Table 8-3 Induced drag and pitching moment coefficient comparison.....	91
Table 8-4 Lift curve slope comparison (Unit: rad^{-1}).....	93
Table 8-5 Neutral point comparison (Unit: MAC).....	93
Table 8-6 Lateral stability derivative comparison.....	94
Table 9-1 Comparison of NP and CG of different sweep angles	99
Table 9-2 Comparison of zero lift pitching moment coefficient	99
Table 9-3 Forward CG and Aft CG of different sweep angle	99
Table 9-4 Sweep influence on CG position and pitching moment coefficient CM	103
Table 9-5 Comparison of the twist.....	104
Table 9-6 Comparison of induced drag	105
Table 9-7 Lift curve slope (Unit: rad^{-1})	106

LIST OF EQUATIONS

(3-1).....	19
(3-2).....	20
(3-3).....	20
(3-4).....	20
(3-5).....	20
(3-6).....	21
(3-7).....	21
(3-8).....	21
(3-9).....	21
(3-10).....	23
(3-11).....	23
(3-12).....	24
(3-13).....	24
(3-14).....	24
(3-15).....	24
(3-16).....	24
(3-17).....	25
(3-18).....	25
(3-19).....	25
(3-20).....	25
(3-21).....	25
(3-22).....	25
(3-23).....	25
(3-24).....	25
(3-25).....	26
(3-26).....	26
(3-27).....	26
(3-28).....	26

(3-29).....	26
(3-30).....	27
(3-31).....	27
(3-32).....	27
(3-33).....	28
(3-34).....	28
(3-35).....	28
(3-36).....	28
(3-37).....	28
(3-38).....	29
(3-39).....	29
(3-40).....	29
(3-41).....	29
(3-42).....	29
(4-1).....	41
(4-2).....	41
(4-3).....	41
(6-1).....	65
(6-2).....	65
(6-3).....	65
(7-1).....	73
(7-2).....	74
(7-3).....	81
(7-4).....	82
(8-1).....	87
(8-2).....	87
(8-3).....	88
(8-4).....	88
(8-5).....	88

(8-6).....	88
(8-7).....	88
(9-1).....	101

LIST OF ABBREVIATIONS

CU	Cranfield University
AoA	Angle of attack
AR	Aspect Ratio
AVL	Athena Vortex Lattice
BWB	Blended Wing Body
CB	Conventional Baseline
FW	Flying Wing
NP	Neutral Point
VLM	Vortex Lattice Method
b	Wing span
ζ_{sp}	Short period damping ratio
ζ_p	Phugoid damping ratio
ω_d	Dutch roll frequency
ζ_d	Dutch roll damping ratio
$\zeta_d \omega_d$	Dutch roll damp
C_{df}	Skin friction drag coefficient
C_{dw}	Zero-lift wave drag coefficient
C_{d0}	Zero-lift drag coefficient
K	Lift to drag ratio
\bar{c}	MAC (Mean aerodynamic chord)
α	Angle of attack
α_0	Zero-lift angle of attack
C_L	Lift coefficient
C_D	Drag coefficient
C_M	Pitching moment coefficient
C_{M0}	Zero-lift pitching moment coefficient
C_{Mq}	Pitching damping derivative
$C_{M\dot{\alpha}}$	Downwash lag damping derivative
C_{lr}	Lateral static stability derivative
C_{lp}	Roll damping derivative

$C_{n\beta}$	Directional static stability derivative
C_{nr}	Yaw damping derivative
q	Pitching rate
θ	Pitching angle
h	Altitude
K_n	Longitudinal static margin
ρ	Air density
S	Wing area
I_{xx}	Moment of inertia in roll
I_{yy}	Moment of inertia in pitch
I_{zz}	Moment of inertia in yaw

1 Introduction

During the academic year from 21st Feb 2011 to 20th Feb 2012, the author has been involved in two main projects, the Group Design Project (GDP) and the Individual Research Project (IRP). Following sections will give the brief introduction about the two projects.

1.1 Research Process

1.1.1 The Group Design Project (GDP)

The Group Design Project is a three-year cooperative training programme between AVIC (Aviation Industry Corporation of China) and Cranfield University. The main objective of this programme is to design a 250-seat flying wing civil airliner. In 2011, twenty-two AVIC students have finished the conceptual design, followed by the preliminary design in 2012 and detail design in 2013.

The Group Design Project contains three phases. In the first phase, the design requirements were fixed after analysing the market, estimating the risk and considering the strategy. According to the requirement, the airplane should have the ability to take 250 passengers fly over 7,500 nautical miles.

In the second phase, an aircraft with conventional configuration was designed. The general configuration of conventional is shown in Fig 1-1. In the following chapters, this configuration will be called CB in short, which means conventional baseline option.

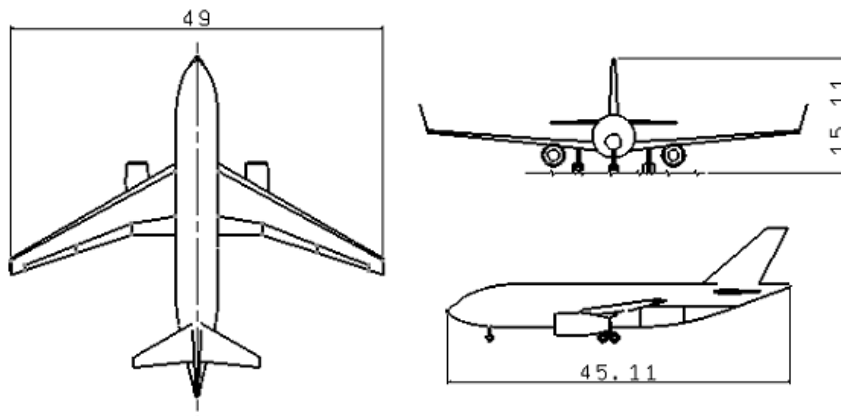


Figure 1-1 Conventional configuration ^[1] (Unit:m)

In the third phase, a flying wing configuration was designed based on the same requirements as the conventional one. The general configuration of flying wing is shown in Fig 1-2. In the following chapters, this configuration will be called FW in short, which indicates it is a flying wing option.

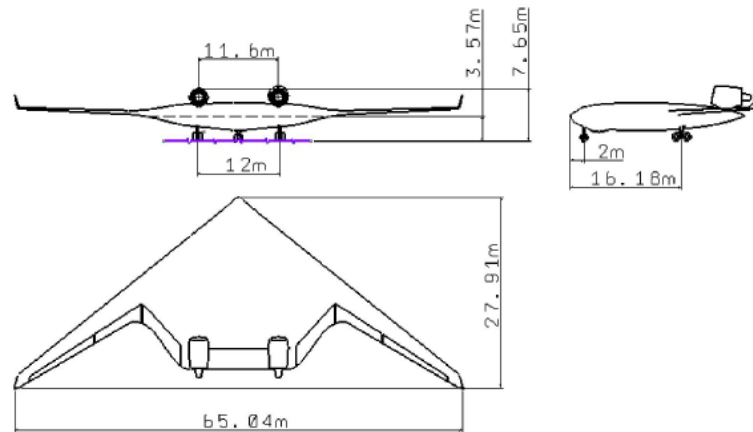


Figure 1-2 Flying wing configuration^[1]

During the group design project, the author was in charge of aerodynamic design of the conventional configuration and flying wing configuration.

1.1.2 The Individual Research Project (IRP)

Besides the option of conventional and flying wing configuration, there is a third option--blended wing body configuration. The overall configuration has taken the reference of BW-11^[2]. The cabin, cargo and fuel tanks are rearranged for the same requirement as 250 passenger seats and 7,500 nautical miles range. In the following chapters, this configuration will be called BWB in short, which indicates it is a blended wing body option.

Based on the Group Design Project design, some extension work has been done. The individual research made the comparison of aerodynamic and stability characteristics between those three configurations. The influence of changing geometry parameters on aerodynamic and stability character was also investigated. Finally, based on the previous study, a case was set up to improve the stability through modifying the geometry parameters.

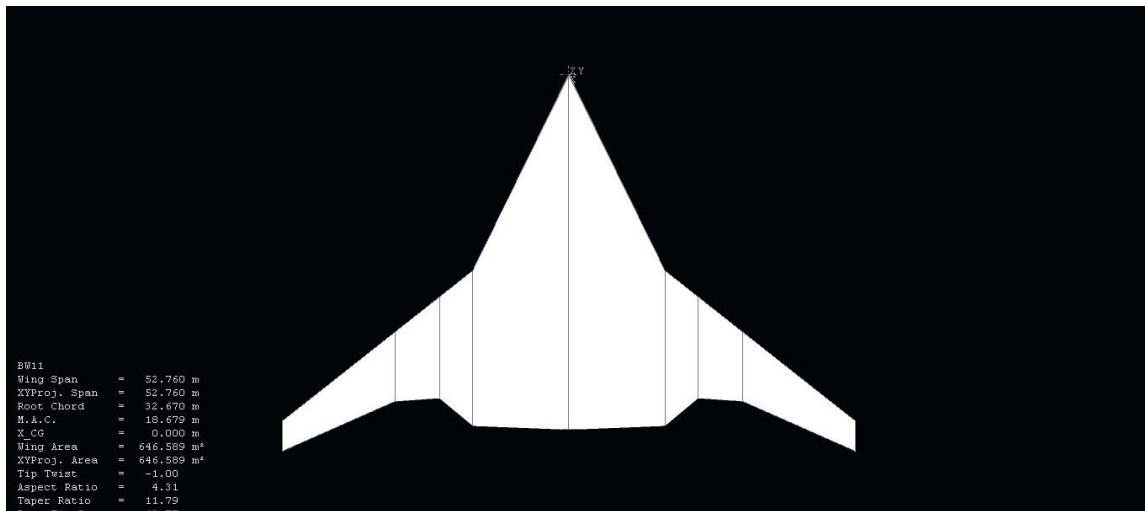


Figure 1-3 Blended wing body configuration ^[3]

1.2 Objectives

The author's research work covers four main objects:

1. Make a comparison of aerodynamic characteristics between the conventional (CB), flying wing (FW) and blended wing body (BWB) options. Some crucial characteristics like lift, drag, pitching moment and aerodynamic derivatives are compared and discussed.
2. Analyse the stability characteristics of conventional (CB), flying wing (FW) and blended wing body (BWB) options. The stability characteristics could be analysed based on the mass data from Zhang Jin ^[3] and aerodynamic data calculated by author. The longitudinal static stability and dynamic stability, lateral-directional static stability and dynamic stability are discussed separately.
3. Investigate the effect of changing geometry parameters on the aerodynamic and stability characteristics of the blended wing body configuration. Since the blended wing body is highly integrated with wing and body, it seems quite sensible for verifying parameters. The effects of twist and sweep angle are evaluated in this section.
4. Explore a case to improve the static stability by changing geometry parameters.

1.3 Thesis structure

The thesis is organized as follow structure:

Chapter 2 presents an overall review of tailless aircraft history and previous studies on blended wing body .The challenges of designing blended wing body aircraft are highlighted, especially on aerodynamic and stability point of view. Besides, the airworthiness requirements are also concluded.

Chapter 3 illustrates the methodology used for calculating the aerodynamic and stability data. With some useful tools, the model set up and calculation iterations are really high efficiency.

Chapter 4 verifies the methods introduced in Chapter 3. Several specific examples are chosen to validate the methods are reliable.

Chapter 5 gives a general description of the three different configurations. Both the three configurations are based on the same requirements, although the configurations are quite different.

Chapter 6 compares the aerodynamic characteristics differences between the three configurations. Three main aspects— lift; drag and pitching moment are discussed. The trim ability for different CG position and Mach numbers are checked, which is of vital importance for tailless configuration. A series of aerodynamic derivatives are provided to make a comparison.

Chapter 7 focuses on the stability characteristics of the three configurations. The differences on longitudinal static stability and dynamic stability, lateral-directional static stability and dynamic stability are compared, and the reasons of these differences are also discussed.

Chapter 8 investigates the geometry parameters influences on the aerodynamic and stability characteristics of blended wing body configuration. The effects of changing parameter are estimated.

Chapter 9 explores a special case to improve the static stability by changing geometry parameters. The process shows that the design of blended wing body is really complex since the closely coupling of several parameters

Chapter 10 summarises the whole research work and conclude the results. The limitations of present research are pointed out and the directions of future work are advised.

2 Literature Review

This literature review chapter contains four aspects. The first part presents the review of the blended wing body aircraft development, followed by the second part focuses aerodynamic study of tailless configuration. Then, the main concern of third part is the stability and control of tailless aircraft. The last part is about the geometry parameter influence on the aerodynamic and stability characteristics.

2.1 Review of history of tailless aircraft

Lippisch^[4] suggested that the aircraft could be classified by its planform shape. The conventional aircraft have wing, fuselage and tail. For the aircraft without tail could be classified to tailless aircraft.

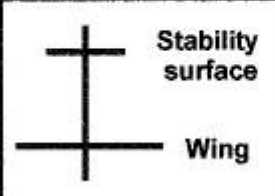
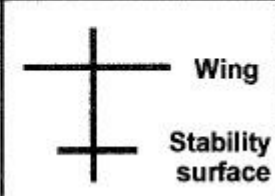
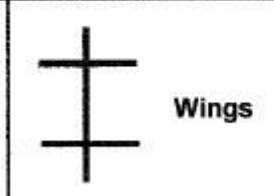

Canard	Conventional	Tandem	Tailless
			

Figure 2-1 Aircraft classification by Lippisch^[4]

According to the description of Castro^[5],The flying wing configuration is no obvious boundary between central body and wing. The blended wing body is the configuration with thick central body integrated on the wing.

There is a quite long history since engineers started the research and develop the flying wing and blended wing body. Richard M.Wood^[6] documented the previous study on the flying wing and flying fuselage configuration.

The most famous flying wing design pioneers are the Horten brothers in German. Started with gliders, they developed over twenty flying wing aircrafts. The first turbo-jet engine flying wing was also invented by them.

In United States, Northrop made great contribution to the development of flying wing.

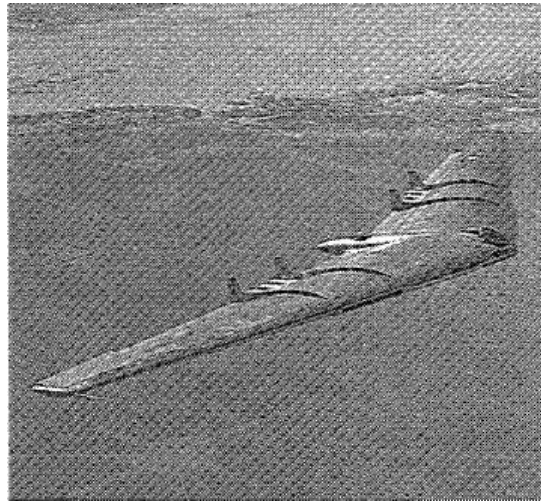


Figure 2-2 Northrop YB-49^[6]

Bolsunovsky et al^[7] mentioned that TsAGI started their research on flying wing configuration since mid 1980s, and the layout provided by TsAGI is shown in Figure2-3.

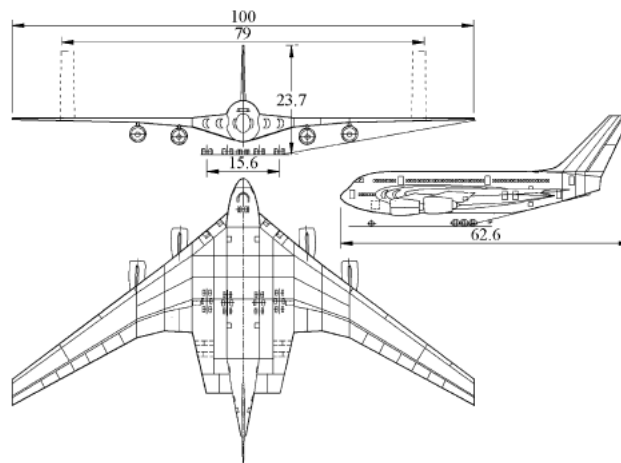


Figure 2-3 Integrated Wing Body of TsAGI^[7]

Sponsored by NASA, Boeing has been continuously improving its BWB concept. Liebeck^[8,9] systematically introduces Blended-Wing-Body airplane concept development in Boeing. The aim of the design is taking about 800 passengers flying across 7,000 nautical miles. Based on the same requirements,

comparisons have been made between the BWB configuration and conventional configuration. Further description on the design from many aspects as configuration definition, aerodynamics, wind tunnel test, stability and control, propulsion, structure, safety and environmental effects are also provided.

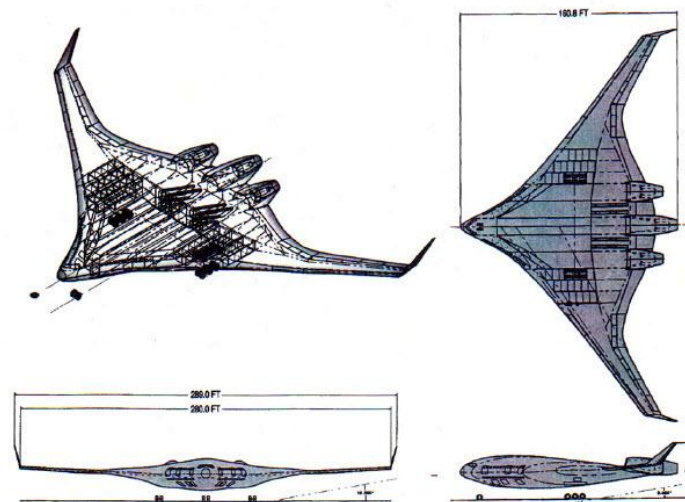


Figure 2-4 BWB of Boeing ^[8]

The most famous flying wing airplane is Northrop B-2 Spirit Bomber. The pure flying wing configuration benefits B-2 with high aerodynamic performance. Therefore, it could take a huge amount of weapon payload to conduct cross continent mission.



Figure 2-5 B-2 Spirit Bomber ^[10]

Although there strong enthusiasm on researching the blended wing body configuration, however, up to now, there is no civil airliner with flying wing or blended wing body configuration.

2.2 Aerodynamic studies of tailless aircraft

Tjoek Eko Pambag ^[11] mentioned there are at least two main benefits from tailless configuration:

For the cruise condition, the most significant advantage of blended wing body aircraft is its high lift to drag ratio. This is achieved by two aspects. Firstly, the body of blended wing body generates lift; secondly, the blended wing body has less wetted area than the conventional, which means the reduction of drag.

For the take-off and landing condition, because of its comparatively low wing loading, only simple high lift devices are needed. That will reduce the design complexity as well as manufacture difficulty of the high lift devices.

At the first glance, the aerodynamic design of a blended wing body aircraft seems to be an easy task. However, several difficulties will emerge when studying this issue in-depth.

D.Roman et al ^[12] mentioned a host of challenges faced by the designers who want to develop a blended wing body aircraft. The first question is higher thickness to chord ratio beyond the normal transonic airfoil due to the volume requirement for containing the cabin, cargo and system. The second tricky is trim at cruise condition should minimise the nose-down pitching moment. The buffet and stall character should also be well considered. The location and function of control surfaces are really hard issue. Besides, some other important points such as the propulsion/airframe integration, landing attitude and speed, and manufacture are discussed.

Since the challenges have been presented, solutions of some problems can be provided.

In order to balance the controversial requirements in aerodynamic and stability, choosing the suitable airfoil for tailless aircraft is of vital importance. Liebeck^[8,9]

pointed out that the reflex airfoil could be used in the centre body in order to meet the trim requirements while the supercritical airfoil is used in the outboard section to achieve high aerodynamic performance.

Eppler^[13] has nearly 30 years working experiences on airfoil design. He points out that the principle of designing the airfoil for tailless airplane is to achieve high C_{Lmax} with a given C_{M0} . Then, some airfoils he suggested (Eppler325, Eppler 327...etc.) could be used on tailless airplane. The most obvious characteristic of this series is their reflex camber line, which will decrease the aft loading of airfoil and then give positive contribution to C_{M0} .

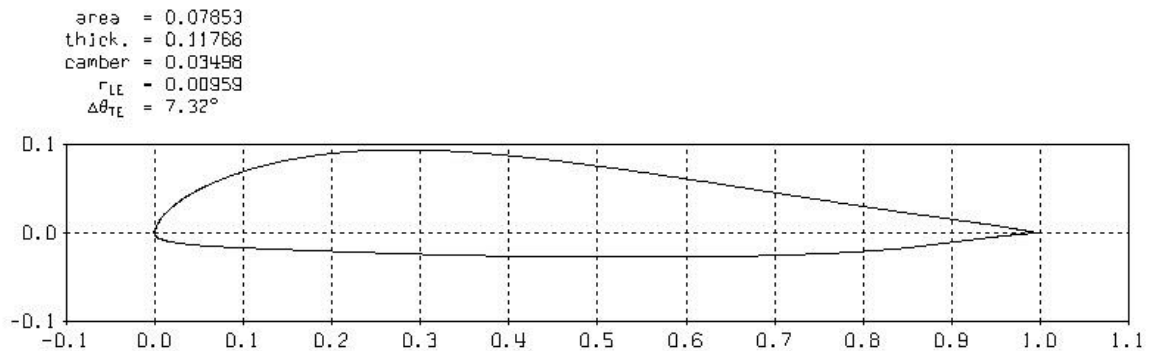


Figure 2-6 Reflex camber airfoil

Harris Charles D^[14] summarized the history of NASA's efforts on developing supercritical airfoil from slotted type to integral shape. The general design philosophy is illustrated and then the impacts of thickness, curvature and camber on airfoil are discussed. Finally a series of supercritical airfoils are presented.

Compared to the conventional airfoil, the significant differences of supercritical airfoil and previous airfoils are as follows: large leading-edge radius flatted upper surface and high aft camber at tailing-edge. The main benefits of this configuration are that the strength of shock wave is weakened and the drag divergent Mach number is postponed.

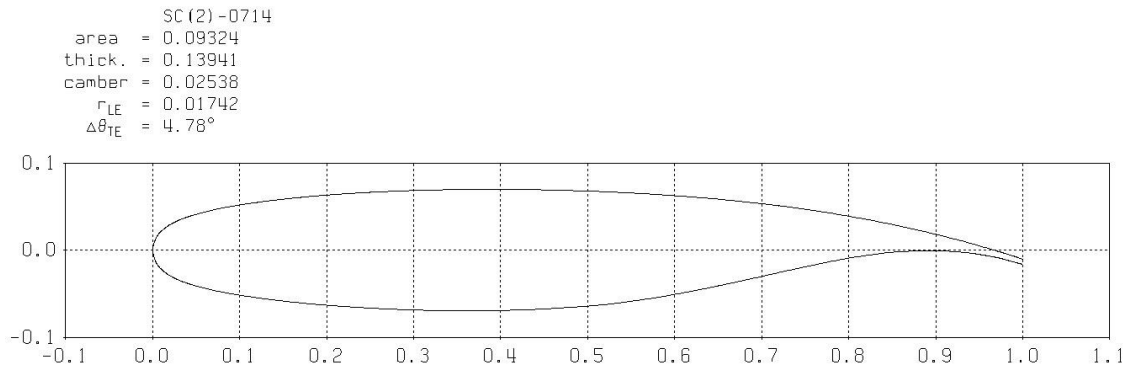


Figure 2-7 Supercritical airfoil

Bolsunovsky et al^[7] points out those full span trailing edge control surfaces like elevons and split rudders could provide control forces for pitch, yaw and roll control. Besides, fins with rudder placed on the wingtip will combine the function of winglet and vertical tail.

Henne,P,A^[15] indicates that Computational Fluid Dynamics is a useful tool when designing a new airplane. This book is a collection of application of computational fluid dynamics to nearly whole design circle of a new airplane. Different CFD tools are chosen in order to meet the different needs of the whole design circle. The CFD tools plays an important role in all this phases, from the beginning of airfoil design, followed by wing design, then wing-body, as well as high-lift systems and propulsion systems.

Paul F. Roysdon.et al^[16] investigates the blended wing body aerodynamic characteristics through two phases: in the first stage, the lower order method based on vortex lattice method is used to get an overall understanding of aerodynamic characteristics; in the second stage, the higher order method CFD codes are used to optimise the performance.

As a conventional aircraft with wing and fuselage, according to the classical lifting line theory, the elliptic lift distribution could produce the minimum induced drag for a give lift and aspect ratio. For the BWB aircraft, the central body and the wing are integrated together, that means the aircraft should be treated as a whole system. N.Qin et al^[17, 18] suspect the opinion of elliptic spanwise lift

distribution and gives the initial discussion, and then an average triangle and elliptic shape lift distribution is suggested.

2.3 Stability studies of tailless aircraft

2.3.1 Longitudinal stability

Some previous work has been done for the stability of tailless aircraft.

In terms of longitudinal dynamics of tailless aircraft, for the phugoid mode, Northrop^[19] found that the flying wing aircraft seems to have less damping than the conventional aircraft because of relatively low drag. For the short period mode, Northrop^[19] commented that the flying wing seems highly damped than conventional one. However, Wilkinson et al^[50] mentioned that flying wing seems to have less damping than the conventional configuration.

2.3.2 Lateral-directional stability

In terms of lateral-directional static stability tailless aircraft, Castro^[5] pointed out that the main problem is its low directional static stability, $C_{n\beta}$. For lateral – directional dynamic stability, Northrop^[19] mentioned out that the two factors- low weather stability and low value of damping yaw coefficient contributing the Dutch roll mode is a long period comparatively. The relative lower damping coefficient in yaw contributes less damping in Dutch roll mode.

2.3.3 Flying quality requirements

The flying and handling qualities of an airplane are those properties “which describe the effectiveness and ease with which it responds to pilot commands in performing flight task”, defined by M.V.Cook^[20].

Several documents regulating the flying quality requirements have been published by airworthiness agencies over the world. Among those, one of the most representative documents is American Military Specification MIL-F-8785C.

Up to now, there is no airworthiness document specified for Blended Wing Body or Flying Wing configuration aircraft. However, MIL-F-8785C has notified that

“The requirements of this specification shall apply for all configurations required or encountered in the applicable Flight Phases.”^[21]

MIL-F-8785C also sets the different airplane category, flight phases and flying quality levels. The research object in this thesis is 250 seats, 7500 nautical mile airliner; flying condition is mainly on cruise trim condition. Accordingly, the Class III aircraft is suitable, category B flight phase and level 1 is suitable.

The longitudinal and lateral-directional flying quality requirements set by MIL-F-8785C are illustrated as follows:

In terms of longitudinal dynamics, the short period mode and phugoid mode are concerned.

Longitudinal short period mode is a relatively fast mode. The pitching angle, angle of attack and flight path may change quickly in this mode. The acceptable criterion of the damping ratio of short period is presented in Table 2-1.

Table 2-1 Short period mode damping ratio requirement^[21]

Level 1	Level 2
$0.3 \leq \zeta_{sp} \leq 2$	$0.2 \leq \zeta_{sp} \leq 0.3$

Longitudinal phugoid mode is a relatively slow mode. Acceptable limit of damping ratio of phugoid mode is listed in Table 2-2.

Table 2-2 Phugoid mode damping ratio requirement^[21]

Level 1	Level 2	Level 3
$\zeta_p \geq 0.04$	$\zeta_p > 0$	$T_2 \geq 55 (s)$

In terms of lateral-directional dynamics, Dutch roll mode, roll mode and spiral mode are involved.

Dutch roll mode is a typical damped oscillation in yaw direction. The requirements of Dutch roll mode damping ratio, damping and frequency are shown in Table 2-3.

Table 2-3 Dutch roll mode frequency and damping requirement ^[21]

	Level 1	Level 2	Level 3
MIN ζ_d	0.08	0.02	0
MIN $\zeta_d \omega_d$	0.15	0.05	--
MIN ω_d	0.40	0.40	0.40

Roll mode is a non-oscillatory lateral characteristic, and the acceptable roll mode time constant requirements are shown in Table 2-4.

Table 2-4 Roll mode time constant requirement ^[21] (Unit: s)

Level 1	Level 2	Level 3
$T_r < 1.4$	$T_r < 3$	$T_r < 10$

Spiral mode is also a type of non-oscillatory mode. For a stable spiral mode, the time constant is irrespective. For an unstable spiral mode, the requirement for minimum double amplitude time is listed in Table2-5.

Table 2-5 Spiral mode minimum double amplitude time requirement ^[21] (Unit: s)

Level 1	Level 2	Level 3
$T_2 \geq 20$	$T_2 \geq 8$	$T_2 \geq 4$

2.4 Geometry parameter influence

Salman A.Ansari ^[22] investigated the influences of wing geometry on the aerodynamic characteristics. The wing geometry contained a series of wing planforms as well as other parameters such as the aspect ratio, wing length, wing area, and wing –offset distance, pitching-axis location. Three main aerodynamic characteristics: lift, lift-to-drag ratio and lift-to-torque ratio were studied using both CFD tools and experiments.

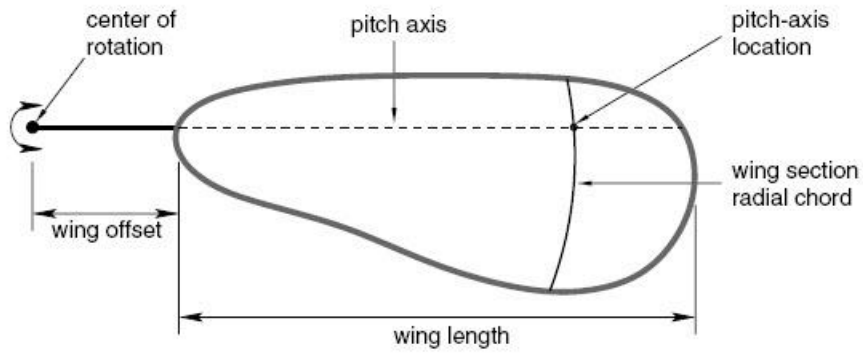


Figure 2-8 Wing parameters^[22]

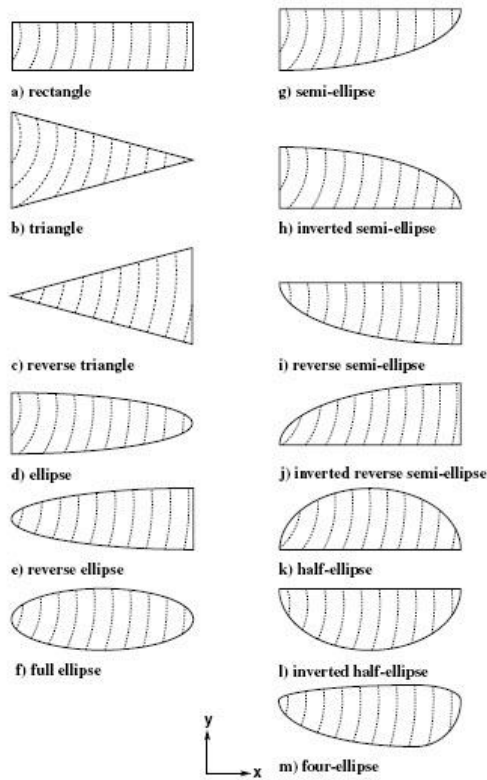


Figure 2-9 13 different wing planforms^[22]

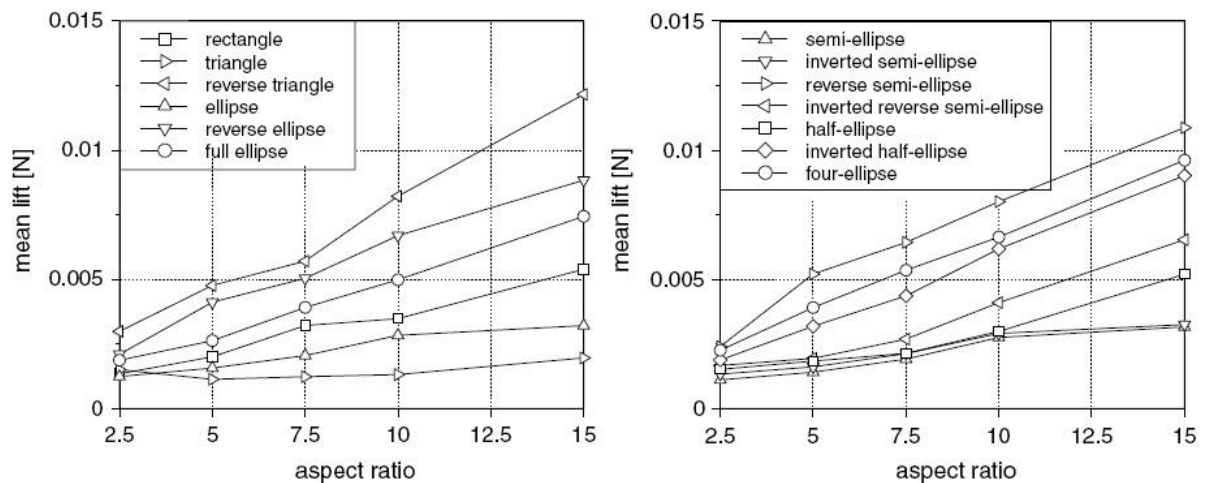


Figure 2-10 the aspect ratio influence on mean lift [22]

Lv Xinbo^[23] focused on the aerodynamic characteristics as well as flying qualities on the box-wing configuration aircraft. Horizontal distance from fore-wing to aft-wing, sweep angle and dihedral angle influences the aerodynamic characteristics and flying qualities were studied.

Ralph Paul^[24] studied the effects of reducing the size of F-16's vertical tail, more specifically, the lateral-directional dynamics. The results shown that, during the subsonic regime from the Mach 0.17 to Mach 0.6, the Dutch roll mode was severely influenced by reducing the tail size. That mode used to be stable and lightly damped with full size tail, then became unstable after scaling 20% less tail size.

2.5 Summary

The previous researches provide some valuable experiences:

1. At the initial stage, some low-order methods could be used for quick estimation. During the conceptual phase, for the aerodynamic calculation, the simple methods like Vortex-Lattice Method or panel method seems to be good choice. During the detail design phase, more advanced, high-order methods, like Navier-Stokes Formula based CFD code will plays important role in the optimisation design work.
2. In order to investigate the influence of changing parameter, only one parameter is varied at a time, the other parameters are keeping at the same

value. This strategy not only reducing the workloads but also making the results comparable.

3 Methodology

This chapter illustrates the calculation methods for the aerodynamic forces and stability derivatives. The method calculating the aerodynamic force is introduced firstly, followed by the stability calculation, and last the support tools used for calculation are introduced.

3.1 Aerodynamic force calculation

Vortex Lattice Method is a reliable method to quickly produce aerodynamic and stability data. The governing equation of VLM method is Laplace's equation. Several codes based on VLM have been developed, such as AVL ^[25] and Tornado ^[26].

W.H.Mason^[52] introduces the procedure of Vortex Lattice Method, which could be simply illustrated as follow steps:

Step1: Divide the planform into a series of panel meshes, and then put one horseshoe vortex on each panel.

Step2: In each panel, the bound vortex is placed on the one-quarter chord line of each panel;

Step3: Place control point in each panel, the chordwise position is located at the 3/4 chord length while the spanwise position is at the midpoint.

Step4: As the classical method, assume a flat wake.

Step5: Solving a system of linear equations, compute the strengths of each Γ_n required to satisfy the boundary conditions.

Figure 3-1 illustrates the horseshoe vortex layout of the classical VLM method. On the basis of the Kutta- Joukowski Theorem, the force could be calculated by Equation 3-1:

$$\mathbf{F} = \rho \mathbf{V} \times \Gamma \tag{3-1}$$

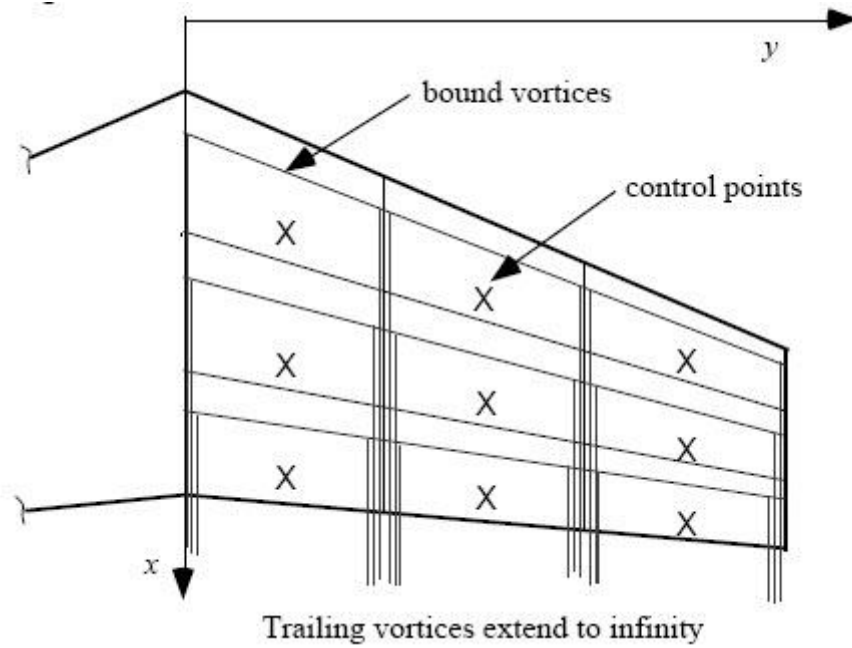


Figure 3-1 The horseshoe vortex layout (classical VLM method) ^[52]

According to introduction in Ref ^[52], for the velocity induced by single horseshoe vortex, the C_{mn} is an influence matrix coefficient for the n th horseshoe vortex effect at the location.

$$\mathbf{V}_m = \mathbf{C}_{mn} \mathbf{\Gamma}_n \quad (3-2)$$

Then the total velocity at point m , combined velocity of free stream velocity and induced velocity, could be given by Equation 3-3:

$$\begin{aligned} \mathbf{V}_\infty = & (V_\infty \cos\alpha \cos\beta + u_{m_{ind}}) \mathbf{i} + (-V_\infty \sin\beta + v_{m_{ind}}) \mathbf{j} \\ & + (V_\infty \sin\alpha \cos\beta + w_{m_{ind}}) \mathbf{k} \end{aligned} \quad (3-3)$$

Assume all the walls are solid, and then the non-penetration boundary condition at all points should satisfy:

$$\mathbf{V} \cdot \mathbf{n} = 0 \quad (3-4)$$

The surface profile could be described by:

$$F(x, y, z) = 0 \quad (3-5)$$

Then the boundary condition can be written:

$$\mathbf{V} \cdot \frac{\nabla F}{|\nabla F|} = 0 \quad (3-6)$$

Substitute all the velocity equation into boundary equation:

$$\left[\left(V_{\infty} \cos \alpha \cos \beta + \sum_{n=1}^{2N} C_{m,n_i} \Gamma_n \right) \mathbf{i} + \left(-V_{\infty} \sin \beta + \sum_{n=1}^{2N} C_{m,n_j} \Gamma_n \right) \mathbf{j} + \left(V_{\infty} \sin \alpha \cos \beta + \sum_{n=1}^{2N} C_{m,n_i} \Gamma_n \right) \mathbf{k} \right] \cdot \left[\frac{\partial F}{\partial x} \mathbf{i} + \frac{\partial F}{\partial y} \mathbf{j} + \frac{\partial F}{\partial z} \mathbf{k} \right] = 0 \quad (3-7)$$

Equations from all the panels could be solved in matrix form, and then vortex strength Γ_n and the induced velocity at each point could be calculated.

Finally, the force acting on each individual panel is calculated through Equations 3-8:

$$\vec{F} = \rho (\vec{V}_{ind} \times \vec{\Gamma}) \cdot l \quad (3-8)$$

Where, \vec{F} is the aerodynamic force, ρ is air density, \vec{V}_{ind} is induced velocity vector, $\vec{\Gamma}$ is vortex strength and l is the length vortex crossing the panel.

3.1.1 Lift

The previous contents introduces the classical vortex lattice method which bases on the Laplace equation assuming that the entire flow field is irrotational and incompressible. In order to take the compressibility into account, the Prandtl-Glauert correlation is taken to consider the compressible effect, according to the AVL user manual ^[25], the Prandtl-Glauert factor $1/B$ is calculated by Equation 3-9.

$$\frac{1}{B} = \frac{1}{\sqrt{1 - Ma^2}} \quad (3-9)$$

Where Ma is the Mach number.

Figure 3-2 describes the trend of Prandtl-Glauert correction factor changing as the Mach number varies.

The AVL user manual ^[25] also lists the reliability of results on different Mach number, which is shown in Table 3-1

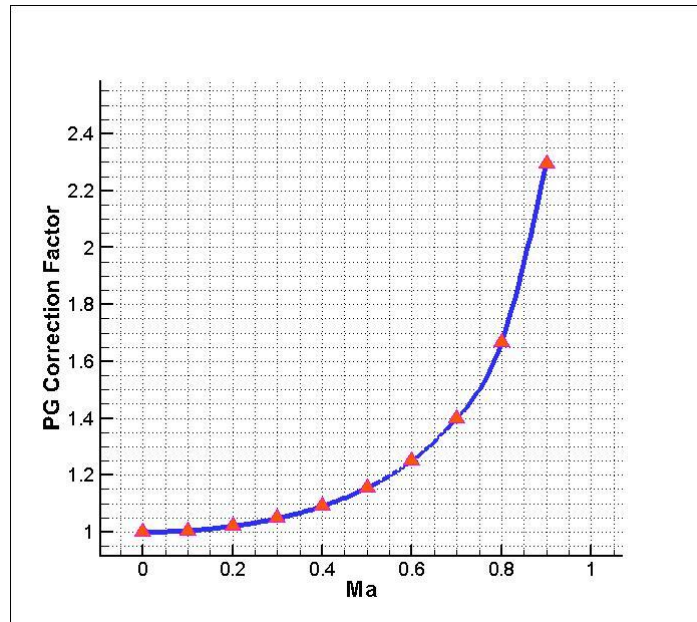


Figure 3-2 PG correction factor

Table 3-1 Mach number PG correction

Mach Number	PG correction factor	Reliability
0.0	1.000	Valid
0.1	1.005	
0.2	1.021	
0.3	1.048	
0.4	1.091	
0.5	1.155	
0.6	1.250	
0.7	1.400	Suspected
0.8	1.667	Unreliable
0.9	2.294	Hopeless

For the swept wing configuration, it is the perpendicular Mach number other than free stream Mach number is used to judge the validity of Prandtl-Glauert model^[25]. The Equation 3-10 shows that there is a wider Mach number range for the swept wing than the upswept wing.

$$Ma_{perp} = Ma_{free\ stream} \cdot \cos(\text{sweep angle}) \quad (3-10)$$

Where Ma_{perp} means wing perpendicular Mach number, and $Ma_{free\ stream}$ is the free stream Mach number. If the free stream of Mach number 0.8 flows over a 45 degrees sweep back wing, the wing perpendicular Mach number is 0.579, which still lies in the valid criterion.

3.1.2 Drag

According to Ref^[27], the wing drag coefficient can be calculated by Equation (3-11)

$$C_D = C_{DF} + C_{DLV} + C_{DW} + C_{DLW} \quad (3-11)$$

C_{DF} is the profile coefficient which combines both the form drag and friction drag. C_{DLV} indicates vortex drag coefficient due to lift which is also called induced drag coefficient. C_{DW} means the wave drag coefficient. C_{DLW} is the wave drag coefficient due to lift.

In terms of C_{DF} , the value could be calculated using software named FRICTION^[28], developed by Virginia Tech.

3.1.2.1 Profile Drag C_{DF}

According to the user manual of FRICTION^[28], the method of calculating profile drag is described simply as follows: firstly calculate the friction drag, then the form drag is calculated by friction drag times a form factor, finally, the profile drag is the sum of friction drag and form drag.

In terms of laminar friction drag, the calculation formula is based on the method introduced in Ref^[29].

For a given edge Mach number M_e and ratio of wall temperature to adiabatic wall temperature T_W/T_{AW}

$$\frac{T_W}{T_e} = \frac{T_W}{T_{AW}} \left(1 + r \frac{\gamma - 1}{2} M_e^2\right) \quad (3-12)$$

Where r is specific heat ratio which equals 1.4. Laminar flow recovery factor equals to 0.88 and T_e is edge temperature which equals to $390^\circ R$.

Since adiabatic wall temperature is

$$T_{AW} = T_e \left(1 + r \frac{\gamma - 1}{2} M_e^2\right) \quad (3-13)$$

The reference temperature approximately equals to:

$$\frac{T^*}{T_e} \cong 0.5 + 0.039 M_e^2 + 0.5 \left(\frac{T_W}{T_e}\right) \quad (3-14)$$

According to the Sutherland's viscosity law and based on the reference temperature, the Chapman-Rubesin constant is:

$$C^* = \left(\frac{T^*}{T_e}\right)^{\frac{1}{2}} \left(\frac{T_e + K}{T^* + K}\right) \quad (3-15)$$

Where K equals $200^\circ R$ for air.

The local friction coefficient C_f could be expressed as:

$$C_f = 0.664 \sqrt{\frac{C^*}{Re_x}} \quad (3-16)$$

Finally, considering the wetted area is almost as twice as reference area, and then the laminar friction drag coefficient is $C_F = 2C_f$.

In terms of the turbulent friction drag, Driest II Method is used to calculate it, which is introduced in Ref^[30].

For a given edge Mach number M_e and ratio of wall temperature to adiabatic wall temperature T_W/T_{AW} . r is specific heat ratio which equals 1.4 , turbulent

flow recovery factor r equals to 0.88 and T_e is edge temperature which equals to $222^\circ K$.

$$F = \frac{T_W}{T_e} = \frac{T_W}{T_{AW}} \cdot \frac{T_{AW}}{T_e} \quad (3-17)$$

$$T_{AW} = T_e \left(1 + r \frac{\gamma - 1}{2} M_e^2\right) \quad (3-18)$$

$$A = T_e \left(\frac{rm}{F}\right)^{\frac{1}{2}}, B = \frac{1 + rm - F}{F} \quad (3-19)$$

$$\alpha = \frac{2A^2 - B}{\sqrt{4A^2 + B^2}}, \beta = \frac{B}{\sqrt{4A^2 + B^2}} \quad (3-20)$$

Then,

$$F_c = \begin{cases} \frac{rm}{\sin^{-1}\alpha + \sin^{-1}\beta} & (\text{if } M_e > 0.1) \\ \left(\frac{1 + \sqrt{F}}{2}\right)^2 & (\text{if } M_e \leq 0.1) \end{cases} \quad (3-21)$$

According the Keyes viscosity law,

$$F_\theta = \sqrt{\frac{1}{F} \left(\frac{1 + \frac{122}{T_w} \times 10^{-\frac{5}{T_w}}}{1 + \frac{122}{T_e} \times 10^{-\frac{5}{T_e}}} \right)} \quad (3-22)$$

F_x is the ratio of F_θ and F_c , calculated by :

$$F_x = \frac{F_\theta}{F_c} \quad (3-23)$$

Given the specific Reynolds number Re_x

Solve the equation:

$$\frac{0.242}{\sqrt{\bar{C}_F}} = \log(F_x Re_x \bar{C}_F) \quad (3-24)$$

Finally,

$$C_F = \frac{\bar{C}_F}{F_c} \quad (3-25)$$

When both laminar and turbulent regions appear on the surface, it is essential to estimate the combined effect of both laminar and turbulent skin friction. According to Schlichting's formula introduced in Ref ^[31], once the transition position x_c and Renault's number Re_L is given, the friction could be computed by:

$$C_F = C_{F_{turb}}(Re_L) - \left(\frac{x_c}{L}\right) [C_{F_{turb}}(Re_c) - C_{F_{lam}}(Re_c)] \quad (3-26)$$

During the form drag calculation process, In order to consider the effects of thickness, form factors are introduced to adjust the skin friction formula. Depends on the different components, two different factors are used.

For wings and tails, which are wing-like shapes, form factor is described as Equation 3-27:

$$FF = 1.0 + 2.7 \left(\frac{t}{c}\right) + 100 \left(\frac{t}{c}\right)^4 \quad (3-27)$$

Where t/c is the thickness ratio of specific component.

For other bodies like fuselage, form factor is calculated by Equation 3-28:

$$FF = 1.0 + 1.5 \left(\frac{d}{l}\right)^{1.5} + 100 \left(\frac{d}{l}\right)^3 \quad (3-28)$$

Where d/l is the ratio of diameter to length.

3.1.2.2 Incompressible induced drag coefficient C_{DLV}

According to the Ref ^[27], the incompressible drag coefficient due to lift is calculated by Equations 3-29.

$$C_{DLV} = \frac{K_v C_L^2}{\pi AR} \quad (3-29)$$

Where, K_v is vortex drag factor described by Equation 3-30:

$$K_v = \left\{ 1 + \frac{(0.142 + 0.0062AR)(10 t/c)^{0.33}}{(\cos\Lambda_{1/4})^2} + \frac{0.1}{(4 + AR)^{0.8}} \right\} \quad (3-30)$$

3.1.2.3 Zero lift wave drag coefficient C_{DW}

In case of high subsonic speed, the wave drag will be produced due to the compressed air. According to Ref^[27], the value of zero lift wave drag coefficient is calculated by Equations 3-31:

$$C_{DW} = \frac{0.12C_F}{Ma} \left\{ \frac{Ma(\cos\Lambda_{1/4})^{\frac{1}{2}}}{(A_f - t/c)} \right\}^{20} \quad (3-31)$$

Where A_f a factor is depends on the airfoil. The value varies as the advanced airfoil would be as high as 0.93 while older aerofoil may as low as 0.75.

3.1.2.4 Wave drag due to lift C_{DLW}

In the subsonic flight range, according to the method in Ref^[27], the waves drag due to lift is suggested that:

$$C_{DLW} = 0.12M_a^6 C_{DLV} \quad (3-32)$$

Where C_{DLV} is given by Equation 3-29.

Up to now, since the methods to calculate all the four components of drag have been provided, the total drag could be estimated by Equation 3-11.

3.2 Stability calculation

In order to calculate the stability characteristics, both the aerodynamic data and mass data are needed.

3.2.1 Longitudinal stability calculation

Based on the state space method and small perturbation assumption, the linear longitudinal state equation could be expressed as Equation 3-33^[53].

$$\begin{bmatrix} \dot{V} \\ \dot{\alpha} \\ \dot{q} \\ \dot{\theta} \end{bmatrix} = \begin{bmatrix} X_v & X_\alpha + g & 0 \\ -Z_v & -Z_\alpha & 1 \\ \overline{M}_V - \overline{M}_{\dot{\alpha}}Z_v & \overline{M}_\alpha - \overline{M}_{\dot{\alpha}}Z_\alpha & \overline{M}_q + \overline{M}_\alpha \\ 0 & 0 & 0 \end{bmatrix} \begin{bmatrix} V \\ \alpha \\ q \\ \theta \end{bmatrix} + \begin{bmatrix} X_{\delta_e} \\ -Z_{\delta_e} \\ \overline{M}_{\delta_e} - \overline{M}_{\dot{\alpha}}Z_{\delta_e} \\ 0 \end{bmatrix} \delta_e \quad (3-33)$$

The detailed definition of those parameters could be found in Ref^[53]. Through analysing the Eigen value of the matrix, the longitudinal dynamic stability characteristics could be researched. A MATLAB code was written to solve the Eigen roots of the matrix and helps to analyse the dynamic stability characteristics.

The longitudinal modes contain the short period mode and phugoid mode.

According to the reduced order method introduced by M.V.Cook ^[20], for short period mode approximation, the reduced order formulation to calculate damping ratio and natural frequency can be written:

$$\omega_{sp}^2 \cong -\frac{C_{M_\alpha} \frac{1}{2} \rho V^2 S \bar{c}}{I_{yy}} - \frac{\frac{1}{2} \rho V^2 S (C_{L_\alpha} + C_D)}{mV} \times \frac{C_{M_q} \frac{1}{2} \rho V S \bar{c}^2}{I_{yy}} \quad (3-34)$$

$$2\omega_{sp} \zeta_{sp} \cong \frac{\frac{1}{2} \rho V S (C_{L_\alpha} + C_D)}{m} - \frac{C_{M_q} \frac{1}{2} \rho V S \bar{c}^2}{I_{yy}} - \frac{C_{M_{\dot{\alpha}}} \frac{1}{2} \rho S V \bar{c}^2}{I_{yy}} \quad (3-35)$$

For the phugoid mode, the damping and natural frequency are:

$$2\zeta_p \omega_p \cong \frac{2gC_D}{V_0 C_L} \quad (3-36)$$

$$\omega_p^2 \cong \frac{2g^2}{V_0^2} \quad (3-37)$$

3.2.2 Lateral-directional stability calculation

Based on the state space method and small perturbation assumption, the linear lateral-directional state equation could be expressed as Equation 3-38.

$$\begin{bmatrix} \dot{\beta} \\ \dot{p} \\ \dot{r} \\ \dot{\phi} \end{bmatrix} = \begin{bmatrix} \bar{Y}_\beta & \alpha + \bar{Y}_p & \bar{Y}_r - 1 & g \cos \theta_* / V_* \\ \bar{L}_\beta & \bar{L}_p & \bar{L}_r & 0 \\ \bar{N}_\beta & \bar{N}_p & \bar{N}_r & 0 \\ 0 & 0 & 0 & 1 \end{bmatrix} \begin{bmatrix} \beta \\ p \\ r \\ \phi \end{bmatrix} + \begin{bmatrix} 0 & \bar{Y}_{\delta_r} \\ \bar{L}_{\delta_a} & \bar{L}_{\delta_r} \\ \bar{N}_{\delta_a} & \bar{N}_{\delta_r} \\ 0 & 0 \end{bmatrix} \begin{bmatrix} \delta_a \\ \delta_r \end{bmatrix} \quad (3-38)$$

The detailed definition of those parameters could be found in Ref^[53].

Through analysing the Eigen value of the matrix, the lateral-directional dynamic stability characteristics could be researched.

The lateral-directional dynamic characteristic consist three modes: Dutch roll mode, roll mode and spiral mode.

According to the reduced order method introduced by M.V.Cook^[20], The Dutch roll mode damping and frequency are given:

$$2\zeta_d \omega_d \cong - \left(\frac{\frac{1}{2} C_{nr} \cdot \frac{1}{2} \rho V_0 S b^2}{I_{zz}} + \frac{C_{y\beta} \cdot \frac{1}{2} \rho V_0 S}{m} \right) \quad (3-39)$$

$$\omega_d^2 \cong - \frac{C_{n\beta} \cdot \frac{1}{2} \rho V_0 S b}{I_{zz}} \quad (3-40)$$

The roll mode time constant is described as:

$$T_r \cong - \frac{I_{xx}}{\frac{1}{2} C_{lp} \cdot \frac{1}{2} \rho V_0 S b^2} \quad (3-41)$$

The spiral mode time constant could be calculated by:

$$T_s \cong - \frac{V_0 (C_{l\beta} C_{np} - C_{lp} C_{n\beta})}{g (C_{lr} C_{n\beta} - C_{l\beta} C_{nr})} \quad (3-42)$$

3.3 Support tools

3.3.1 ESDU

Engineering Science Data Unit, also called ESDU for simple, is useful and powerful tool to estimate the aerodynamic data. The basic method and results have validated by worldwide academic and industry experts that makes ESDU is of a high reputation. The ESDU Aerodynamics Series provides a range of documents and programmes to the aerodynamic data. In this research, ESDU datasheet is used to calculate the MAC (mean aerodynamic chord), NP (neutral point), and other important parameters.

3.3.2 AVL

AVL is written by Harnold Youngren and Mark Drela at MIT. According to the AVL user manual ^[25], it is quite suitable for configurations mainly of thin lifting surfaces, and the flow condition is subsonic, small angle of attack and sideslip.

AVL is a type of Vortex Lattice Method code solving the Laplace Equation and the method has been introduced in previous chapter. Beyond the capability of calculating the aerodynamic data, the code could also compute the stability and control characteristics of aircraft combined with input mass file.

3.3.3 XFLR

XFLR is developed based on the XFOIL ^[45], which focus on the airfoil and wing on low Reynolds number. XFLR has the interface with AVL. This function provides an easy way to define a new configuration, change the geometry parameters, and then output the file for AVL.

In this research, XFLR is used to set up the model and then output to AVL. The function is quite helpful especially in the parameter study described in Chapter 8.

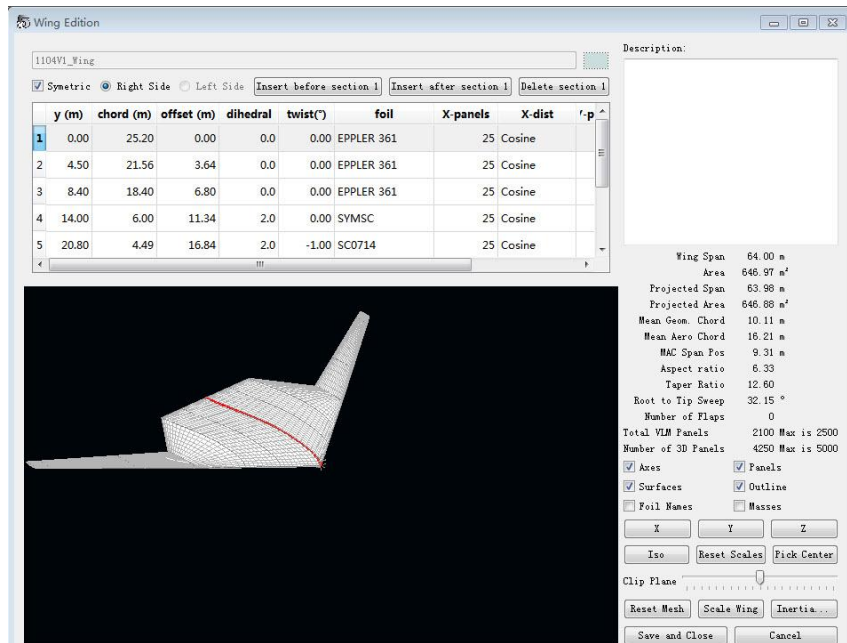


Figure 3-3 Wing geometry parameter

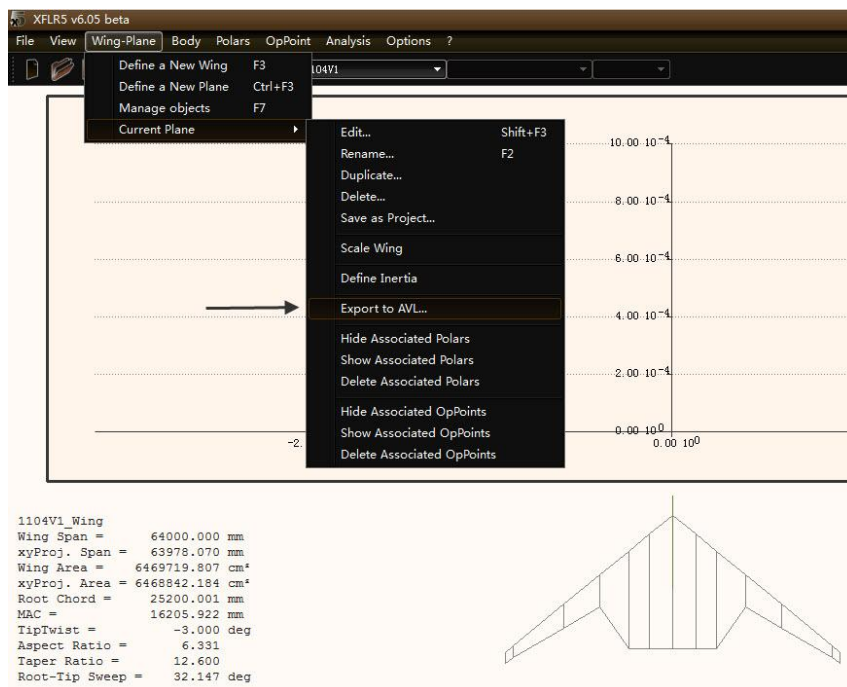


Figure 3-4 XFLR interface with AVL

The AVL and XFLR are released under GNU General Public License, and could be downloaded the software from website. Cranfield University is an authorised user of ESDU. All the softwares introduced in this research are legally used.

3.4 Research flow chart

The research flow chart is represented in Fig 3-4.

In step 1, the aerodynamic data are calculated by AVL. The mass, CG and moments of inertia data are inputted to calculate the stability characteristics.

In step 2, the stability characteristics are computed combined with aerodynamic data, mass, CG and moments of inertia data.

In step 3, the aerodynamic and stability characteristics of the three configurations are compared.

In step 4, since it is found the static stability of BWB is not quite good, the general configuration is modified to improve the static stability.

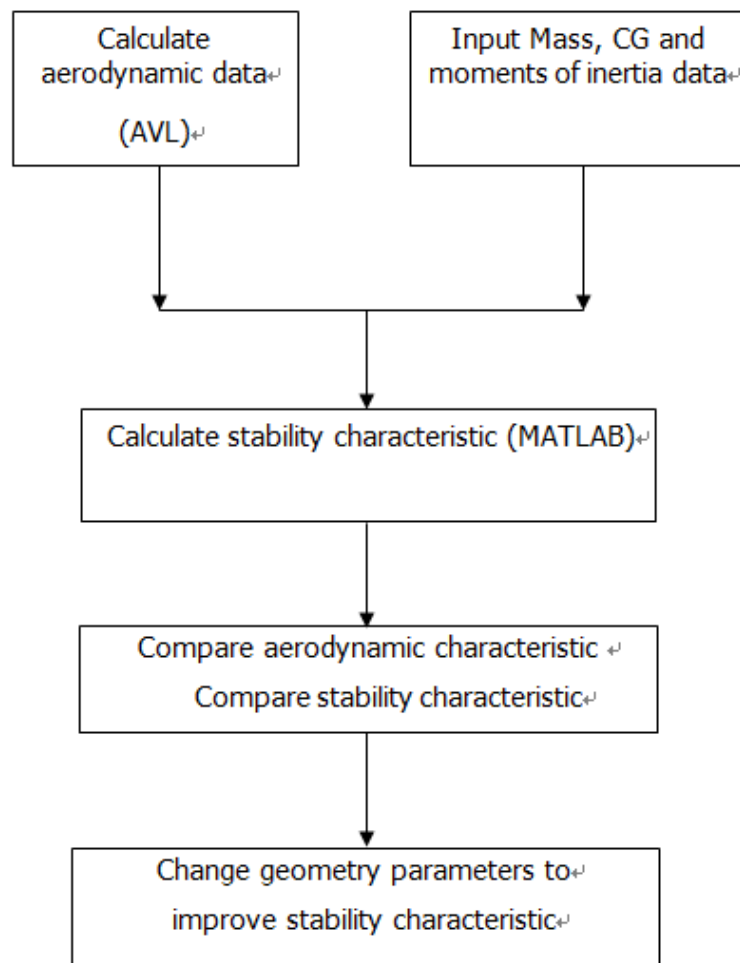


Figure 3-5 Research flow chart

4 Validation

Before the calculation starts, it is essential to run some examples to validate the suitable method are chosen. This chapter validates the methods introduced in the previous chapter are right and results based on these are reliable.

Taken reference from Ref^[32], several validation examples are chosen to test the abilities of AVL:

The first validation example--2D flat plate is to estimate the influence of mesh number, and the second example --Warren 12 is to estimate the mesh distribution methodology. The following examples are testing the AVL's ability to reflect the sweep and twist of wing, and the last one is to check the credibility of stability calculation.

4.1 Mesh number

4.1.1 Case introduction

The purpose of this test is to check the impact of different mesh numbers on the calculation data. Four AVL simulation models with different mesh density are set up based on the same high aspect ratio wing.

The high aspect ratio wing span is 20m and chord length is 1m, as shown in Figure 4-1.

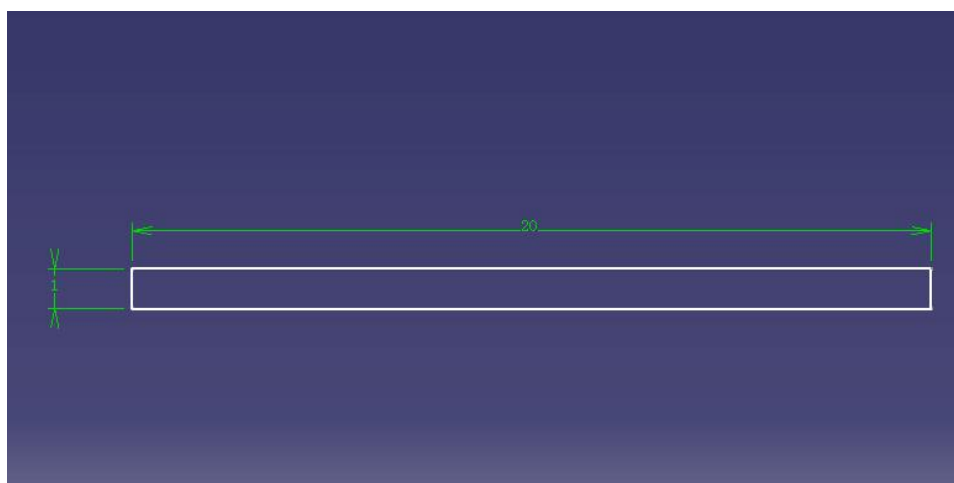


Figure 4-1 2D flat plate (Unit:m)

Table 4-1 2D flat plate parameter

Aspect Ratio	20.0
Reference Chord Length(m)	1.0
Wing Area(m ²)	20.0
Angle of attack	10°
Air speed (m/s)	10
Air density (kg/m ³)	1

4.1.2 Case setting

As illustrated in Figure 4-2, the spanwise mesh number is fixed as 34; for the chordwise, four different chord wise mesh number-2, 5, 10, 15-are used to test the mesh sensitive of results.

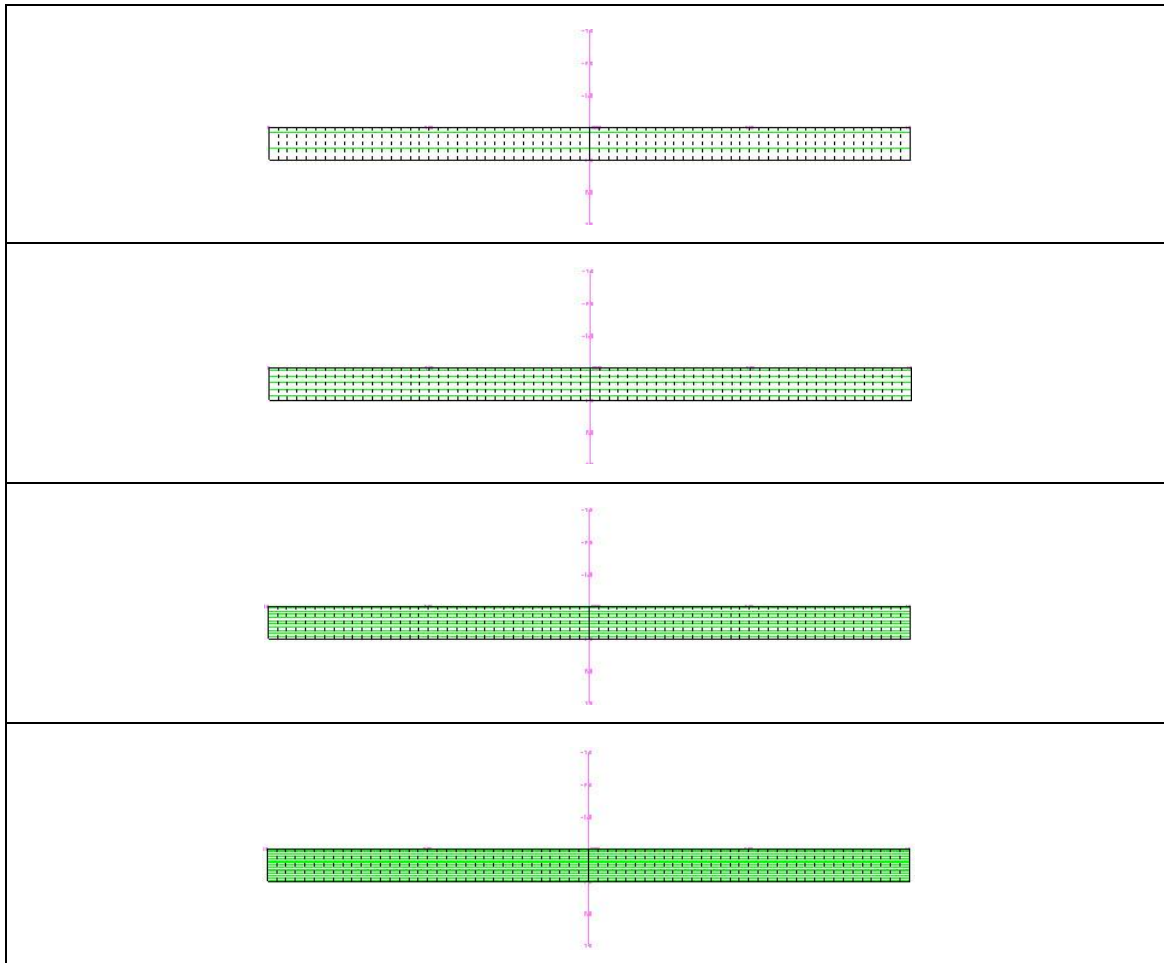


Figure 4-2 Different mesh density

Both the four cases are running on the same calculation condition, which is described in Table 4-2:

Table 4-2 Simulation condition

Angle of attack	10°
Air speed (m/s)	10
Air density (kg/m ³)	1

4.1.3 Results and discussion

Theoretical data is obtained from Ref [33]. The results based on different mesh numbers and the comparisons with theoretical data are shown in Fig4-3.

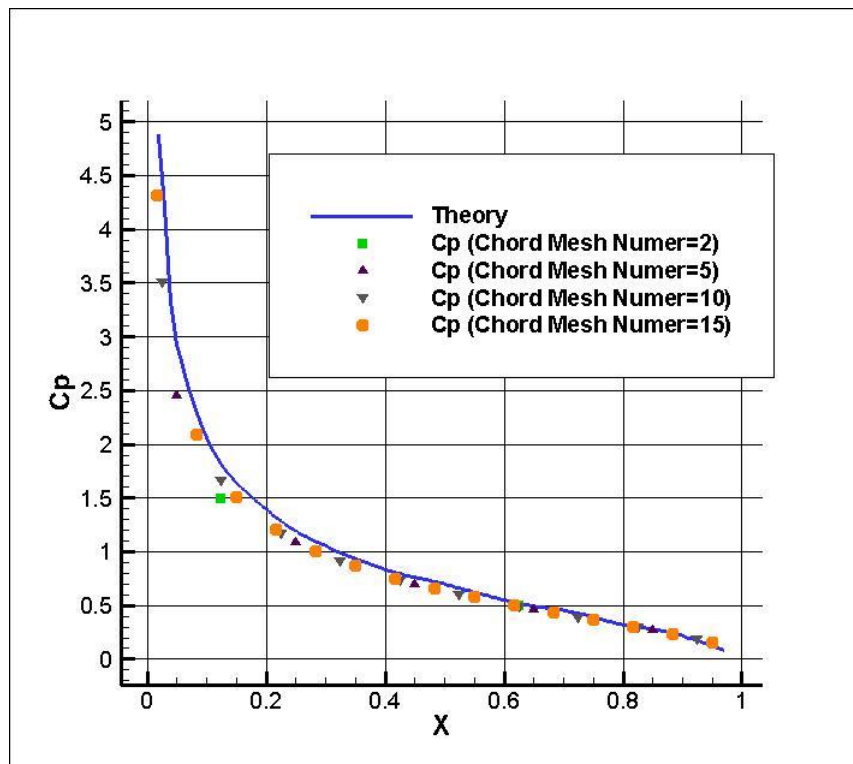


Figure 4-3 2D Cp of different mesh number compare to theory value

Obviously, the more mesh number on the chord length, the calculation result will be more accordance with the theoretical data. Too coarse mesh may not lead to good result, while too fine mesh seems to be “spoiled” to promote the accuracy. Therefore, it would be better to take a good balance between the mesh number and result accuracy.

4.2 Mesh distribution

4.2.1 Case introduction

As described by Ref^[32], Warren 12 is a standard model for testing the existing and newly developed vortex-lattice method codes. The main aim of this test is to check the effect of different panel mesh density and distribution.

The planform and geometry parameters of Warren12 are shown in Fig4-4 and Table4-3 respectively.

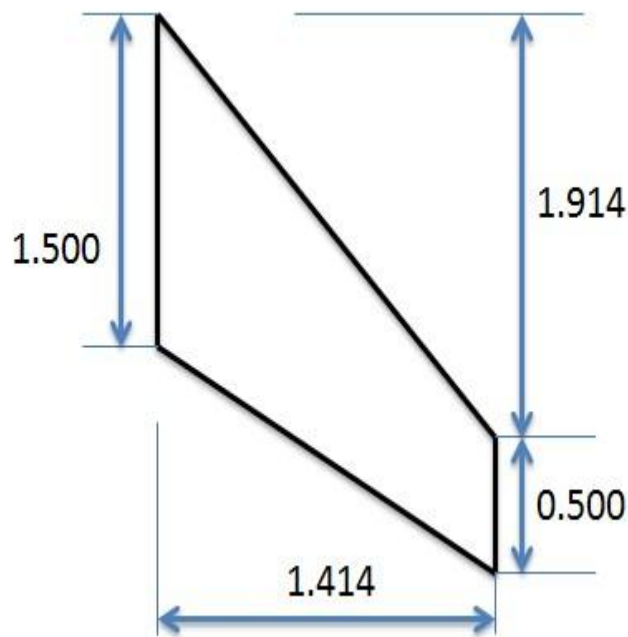


Figure 4-4 Warren 12 planform (Unit:m)

For all the calculation conditions, the reference chord length is mean aerodynamic chord and the reference point for moment calculation locates at the wing apex (not the one-quarter mean aerodynamic chord).

Table 4-3 Warren 12 geometry parameter

Aspect Ratio	2.83
Leading Edge Sweep Angle	53.54°
Reference Chord Length(m)	1.00
Wing Area (m ²)	2.83
Moment Reference Point(m)	0.00

4.2.2 Case setting

This validation work contains six cases.

Three types of mesh densities are used in the testing cases. The coarse mesh case is 6 chordwise mesh number and 16 spanwise mesh number. The medium mesh case is 8 chordwise mesh number and 24 spanwise mesh number. The finest mesh case is 16 meshes in chordwise and 36 meshes in spanwise .

Two types of mesh methodology—uniform and cosine distributions are contained. For the uniform distribution, the chord and span are equally divided. For the cosine distribution, the mesh density is relatively high in the edge while low in the middle part.

Overall, there are six cases with various mesh distribution methodologies, which are shown in Table 4-4.

Table 4-4 Mesh distribution methodology

	Chord Mesh Number	Chord Mesh Methodology	Span Mesh Number	Span Mesh Methodology
Case 1	6	Uniform	16	Uniform
Case 2	8	Uniform	24	Uniform
Case 3	16	Uniform	36	Uniform
Case 4	6	Cosine	16	Cosine
Case 5	8	Cosine	24	Cosine
Case 6	16	Cosine	36	Cosine



Figure 4-5 Uniform and cosine distribution^[25] (1)

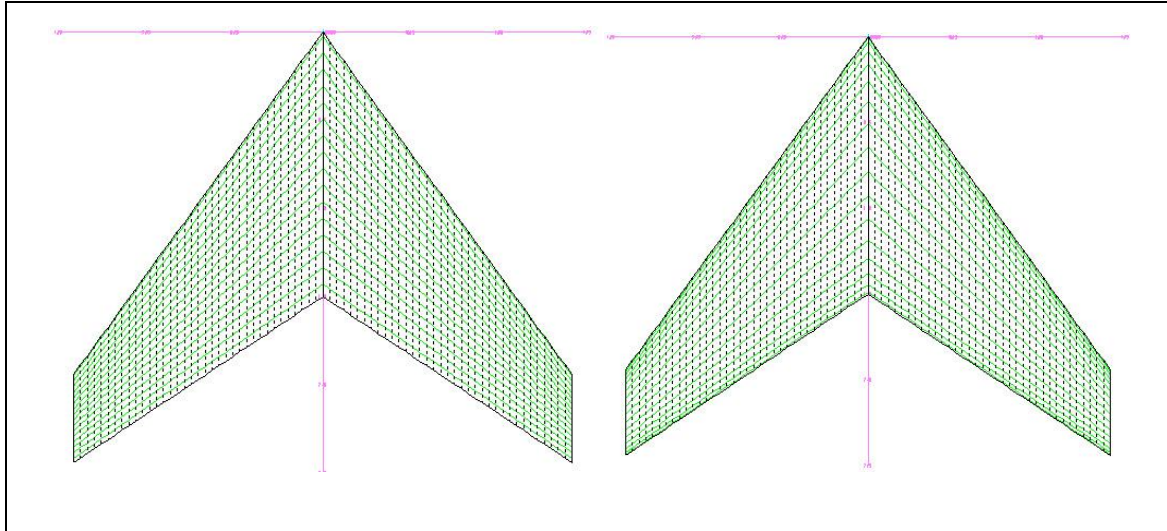


Figure 4-6 Uniform(left) and cosine (right) distribution (2)

4.2.3 Results and discussion

According to the different cases, the results compared to the theoretical data are shown in Tab 4-5.

Table 4-5 Comparison between calculation and theoretical data

	$C_{L\alpha}$	$C_{M\alpha}$	$\Delta C_{L\alpha}$	$\Delta C_{M\alpha}$
Expected	2.743	-3.10	0	0
Case 1	2.773	-2.826	0.030	0.274
Case 2	2.759	-2.806	0.016	0.294
Case 3	2.751	-2.796	0.008	0.304
Case 4	2.723	-2.756	-0.020	0.344
Case 5	2.725	-2.762	-0.018	0.338
Case 6	2.728	-2.764	-0.015	0.336

Generally, increasing the mesh number really helps to get closer to the theoretical value of lift coefficient. Cases with the uniform mesh distribution have better performance than the cosine distribution. The intention of the cosine spacing option is expected to get a more accurate result. However, the situation does not appear. The reason for this condition is that the forces change smoothly along spanwise and chordwise. Therefore, the uniform spacing is

better suitable than the cosine spacing. This validation indicates that a sensible spacing approach should be taken for calculation.

4.3 Sweep

4.3.1 Case introduction

Two wings-one with 0 sweep angle and the other one with 35 sweep angle examples are set up to test the AVL with the ability to calculate the differences between the two wings. Both the two wings have 10 ft wing span and 1 ft chord length.

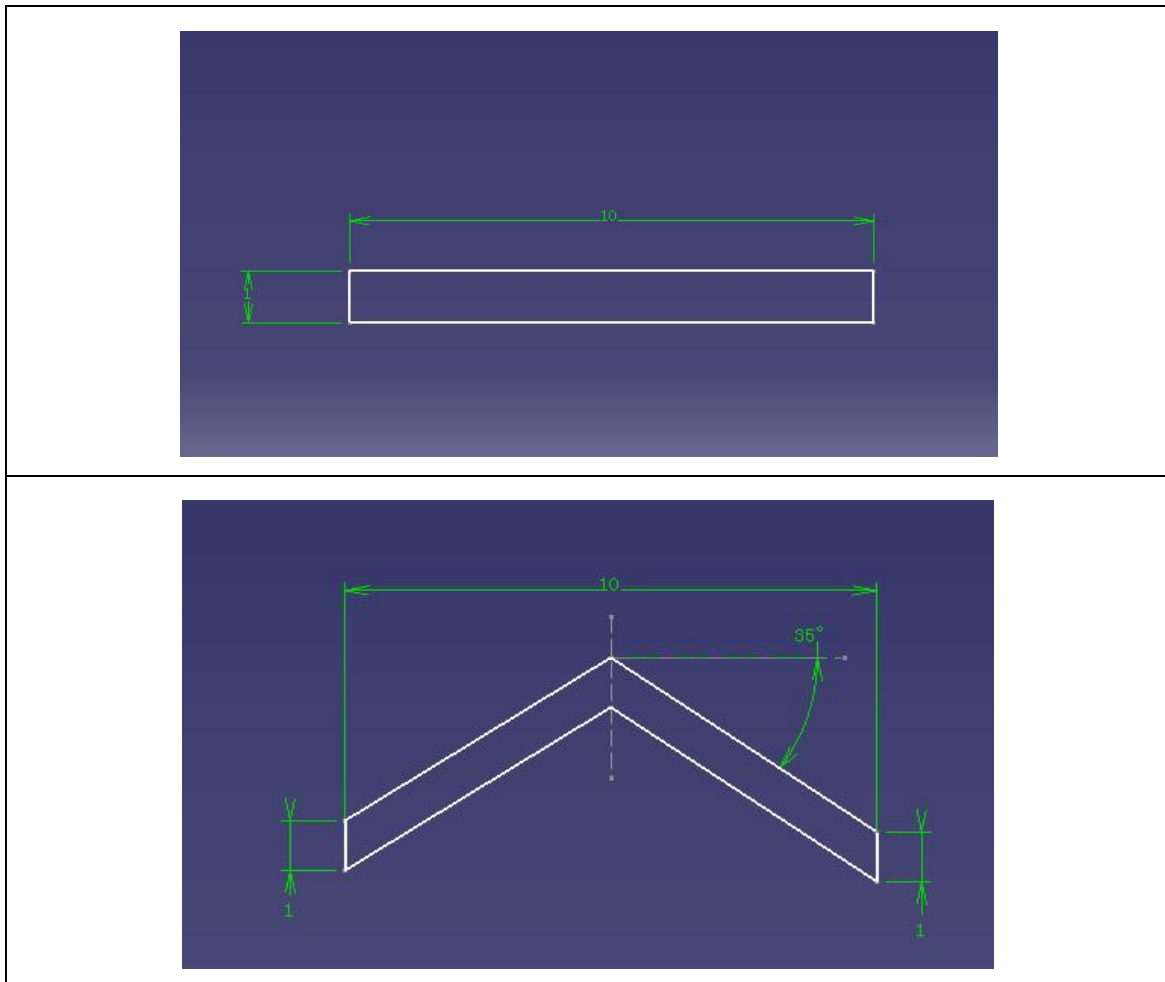


Figure 4-7 0 sweep and 35 sweep wing configuration (Unit:ft)

Table 4-6 Wing geometry parameter

Span (ft)	10
Chord (ft)	1
Wing Area (ft ²)	10
Aspect Ratio	10
Airfoil	NACA 0009
Angle of attack	10°
Air speed (ft/s)	168.8
Air density (slug/ft ³)	0.002378

4.3.2 Case setting

The AVL models of the two wings are shown in Figure 4-8. Both of the two meshes share the same mesh density and mesh distribution methodology

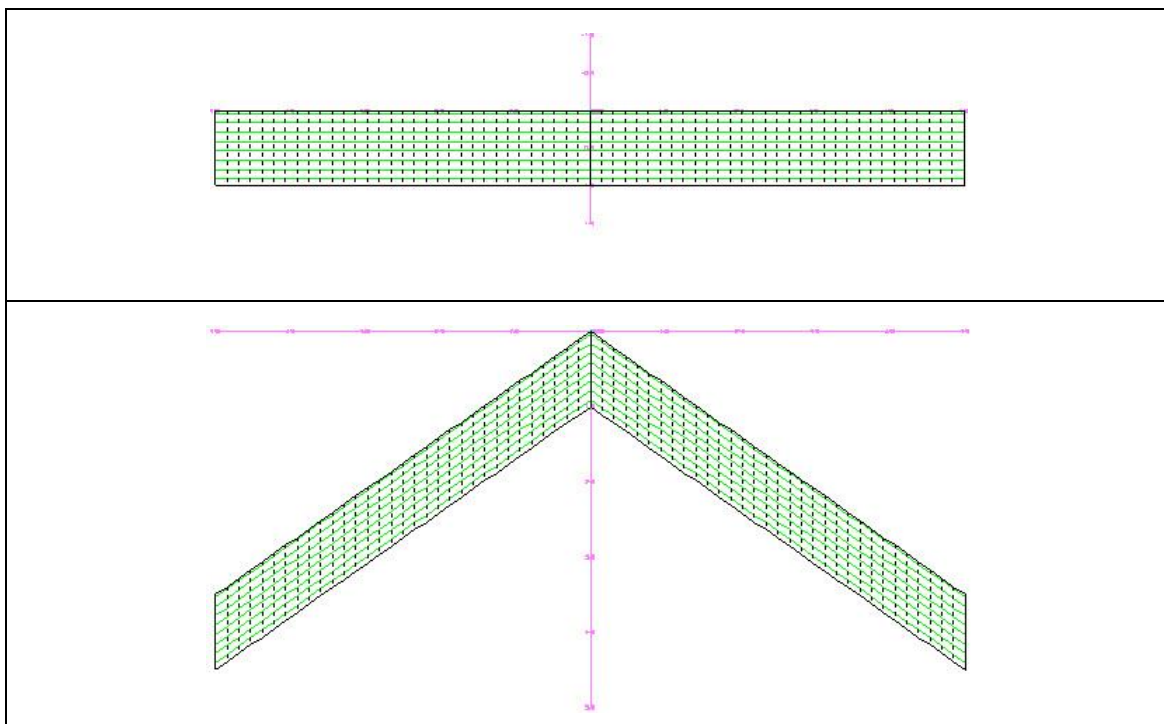


Figure 4-8 0 sweep and 35 sweep wing AVL model

Both of the two wings are calculated on the same condition as illustrated in Table 4-7.

Table 4-7 Simulation condition

Angle of attack	10°
Air speed (ft/s)	168.8
Air density (slug/ft ³)	0.002378

4.3.3 Results and discussion

According to the method introduced in Ref ^[34].The lift slope and the induced drag coefficient could be calculated by Equations 4-1 and 4-2 respectively.

$$C_{L\alpha} = \frac{2\pi * AR}{2 + \sqrt{\frac{AR^2 \beta^2}{\kappa^2} \left(1 + \frac{\tan^2 \Lambda_{c/2}}{\beta^2}\right) + 4}} \quad (4-1)$$

$$C_{Di} = \frac{C_L^2}{\pi * AR} \quad (4-2)$$

Since NACA0009 is a symmetric airfoil, the lift at 10 degree is calculated by Equation 4-3:

$$C_L = 10 * C_{L\alpha} \quad (4-3)$$

According the different cases, the comparisons of AVL calculation results with theoretical method results is shown in Tab 4-8 and Tab 4-9. The lift curve slope and lift coefficient calculated by AVL is a little lower than the theoretical data. For the 0 degree leading sweep angles, the induced drag coefficient is relative higher than the classical method result while the 35 degrees leading sweep angle, the induced drag is lower than the classical method result.

Generally, the result calculated by AVL is reliable.

Table 4-8 Summary of 0 leading sweep angle wing

Parameter	Symbol	Theoretical data	AVL result
Lift curve slope	$C_{L\alpha}$	0.0885	0.0834

Lift coefficient	C_L	0.8850	0.8514
Induced drag coefficient	C_{Di}	0.0249	0.0235

Table 4-9 Summary of 35 leading sweep angle wing

Parameter	Symbol	Theoretical data	AVL result
Lift curve slope	$C_{L\alpha}$	0.0748	0.0712
Lift coefficient	C_L	0.7480	0.7264
Induced drag coefficient	C_{Di}	0.0178	0.0186

4.4 Twist

4.4.1 Case introduction

The aim of this validation example is to test the ability of AVL for calculating the wings with different airfoils and twist angles.

In the NACA-TN-1422^[35], three different wings shared the same general planform are shown in Fig4-9. The wing1 had the NACA 64-210 airfoil with -2 twist angle, the wing2 had the NACA 65-210 airfoil and -2 twist angle, and the wing3 had the same airfoil as wing2 but with no twist. The differences of the three wings are described in Table 4-10. This validation compares the results calculated by AVL and the wing tunnel experimental data.

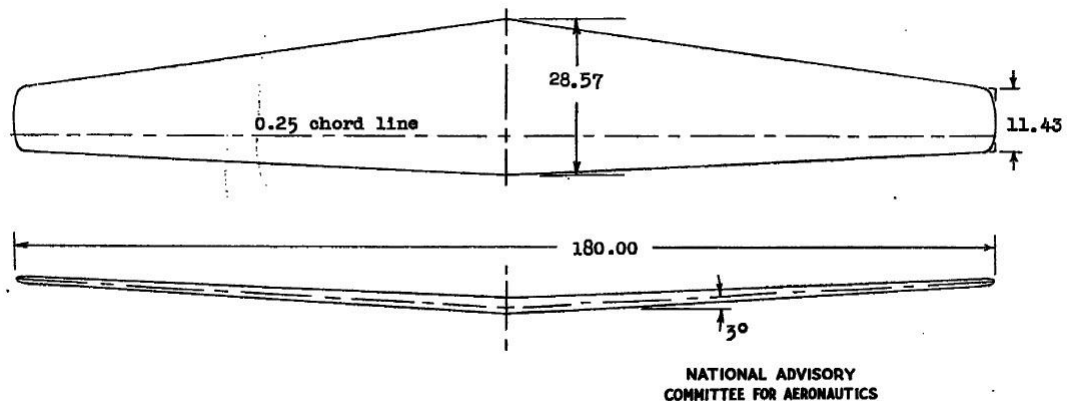


Figure 4-9 NACA1422 wing planform^[35]

Table 4-10 Different twist and dihedral of three wings

Wing	Airfoil	Twist	Dihedral
Wing1	NACA 64-210	-2°	3°
Wing2	NACA 65-210	-2°	3°
Wing3	NACA 65-210	0°	3°

4.4.2 Case setting

Both the three wings are conducted wind tunnel experiment at a Mach number of approximately 0.17. In order to make a fair comparison, the AVL simulation chooses the same Mach number.

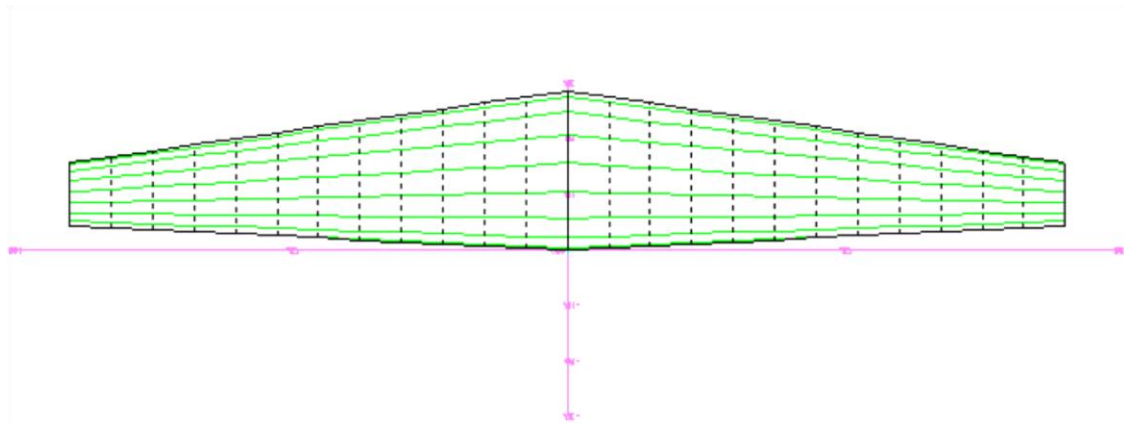


Figure 4-10 NACA1422 model for AVL

4.4.3 Results and discussion

The blue line in Figure 4-11 is the experimental data while the yellow delta symbol dots are the data calculated by AVL. The figure shows that the computed spanwise lift distribution of wing2 is close to the experimental data. Generally, the lift coefficient is in good agreement. The error is mainly because the viscosity effect is neglected in the Vortex Lattice Method.

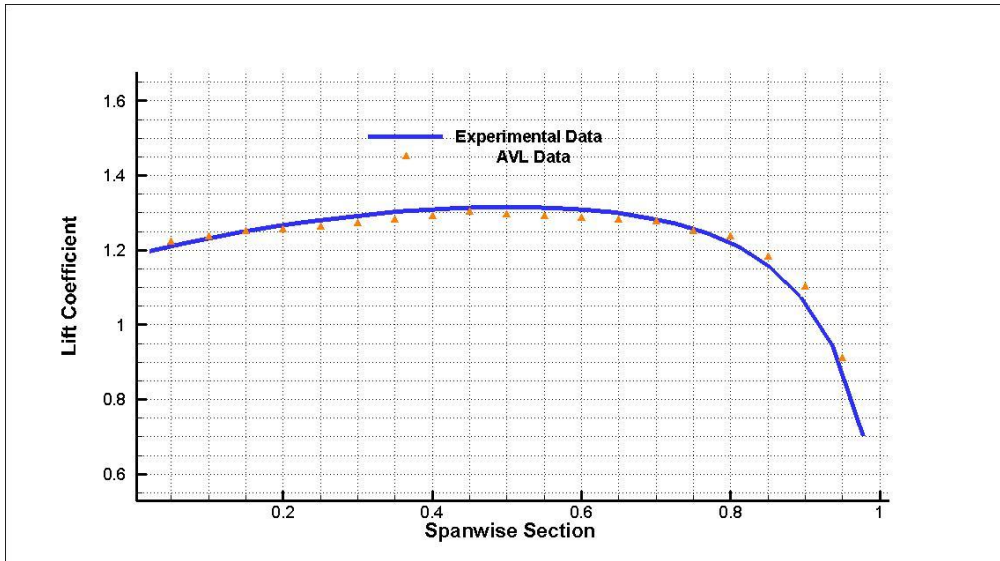


Figure 4-11 Lift distribution curve

Figure 4-12 shows the comparison of the differences of three wings. There is slightly different in wing2 and wing1, which is not very obvious. For the wing1 with 2° positive twist, it will bring relative higher lift than other two wings at the same angle of attack.

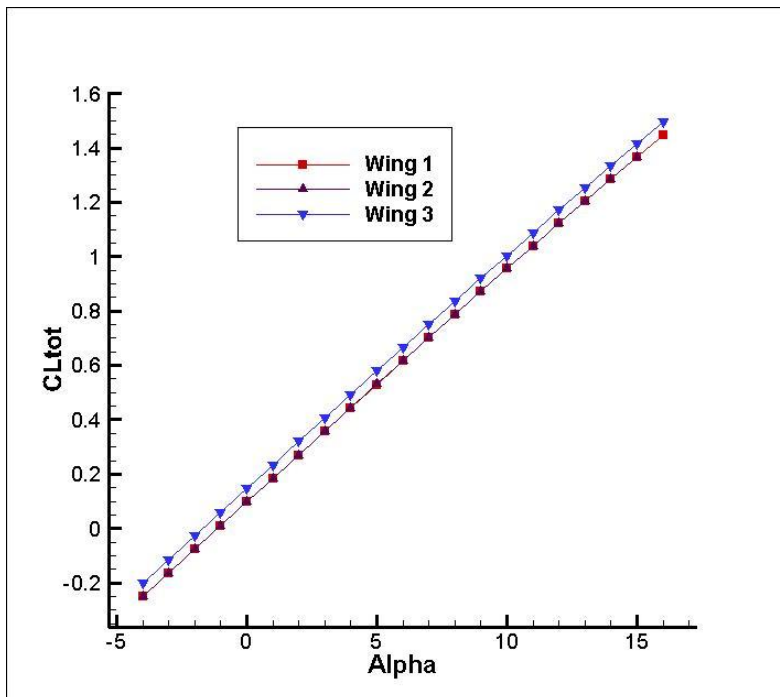


Figure 4-12 Lift coefficient versus alpha (angle of attack) curve

This validation shows that the AVL simulation could reflect the difference of changing twist, and the spanwise lift distribution is in good accordance with experimental data. Therefore, AVL can be used for estimation the effect of twist.

4.5 Stability calculation

4.5.1 Case introduction

The aim of this test is to compare the aerodynamic calculation data from AVL and the stability calculation data from MATLAB with the flight test data of a sailplane. A sailplane was made to fly and flight data were collected. The flight test data and geometry data for AVL comes from Deperrois^[36]. Two slow periodic modes: Phugoid mode and Dutch roll mode periods are compared in this test.

According to the sailplane parameter data in Ref ^[36], the main geometry data are listed in Table 4-11.

Table 4-11 Parameters of sailplane ^[36]

Geometry Data	Span (m)	3.150
	MAC (m)	0.202
	Wing Area (m ²)	0.605
	CG Position (m)	0.090(from leading edge)
Mass	Mass (kg)	2.1
Inertia	$I_{xx}(\text{kg}\cdot\text{m}^2)$	0.565
	$I_{yy}(\text{kg}\cdot\text{m}^2)$	0.161
	$I_{zz}(\text{kg}\cdot\text{m}^2)$	0.723
	$I_{xy}(\text{kg}\cdot\text{m}^2)$	0.000
	$I_{yz}(\text{kg}\cdot\text{m}^2)$	0
	$I_{zx}(\text{kg}\cdot\text{m}^2)$	0

4.5.2 Case setting

Based on the geometry data, the AVL simulation model of sailplane is shown in Fig 4-13.

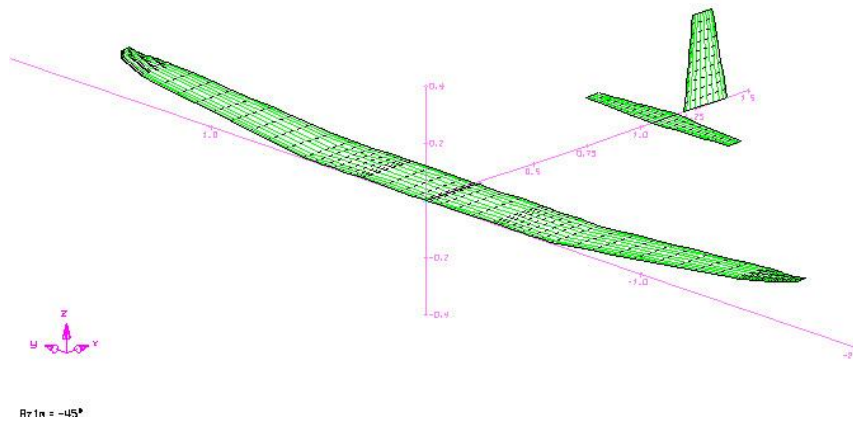


Figure 4-13 Sailplane AVL simulation

The trimmed simulation condition is described in Table 4-12^[36]:

Table 4-12 Simulation condition^[36]

Angle of attack	-1°
Air speed (m/s)	13.1
Lift coefficient	0.324
Pitching moment coefficient	0.000

4.5.3 Result and discussion

Firstly, the aerodynamic derivatives data are calculated by AVL, and then those data are treated as input data in MATLAB program to calculate the stability data. The Eigen roots and related modes are listed in Table 4-13^[36].

Table 4-13 Eigen roots and related modes ^[36]

Mode	Eigen roots	Damping ratio	Frequency (s⁻¹)	Period (s)	Flight test period data ^[36]
Dutch Roll	-1.3844 - 4.8186i -1.3844 + 4.8186i	0.285	4.910	1.280	1.10
Phugoid	-0.0443 + 0.6862i -0.0443 - 0.6862i	0.007	0.629	9.995	10.00

Table 4-14 compares the phugoid period and Dutch roll mode periods of calculation data and flight test data ^[36], it is clearly noticed that the calculation data and flight test data are in good consistence.

This validation proves the calculation process is reliable, which firstly using the AVL to calculate the aerodynamic data and then input to MATLAB to calculate the dynamic data.

4.6 Summary of validation

The above five cases have tested different aspects of AVL simulation results.

Generally speaking, with suitable mesh number and proper mesh distribution methodology, the results calculated by AVL have good consistency with theoretical data or experimental data. Besides, the code can reflect the aerodynamic characteristic differences of varied geometry parameters like sweep and twist. The stability analysis of the sailplane is also quite close to the flight test data.

In summary, AVL is a reliable tool to analyse the aerodynamic as well as stability characteristics.

5 Model Description

This chapter presents the models of three configurations: CB, FW and BWB, which are analysed in this research.

As illustrated in Chapter 1, the conventional configuration--CB was designed in the second phase of GDP, and the flying wing configuration--FW was designed in the third phase of GDP. The blended wing body option--BWB is taken the reference of BW-11^[2].

For the convenient to direct comparison, the conventional, flying wing and blended wing body configurations are based on the same design constraints. Two main parameters: the passenger number and the range are fixed. The passenger number is about 250, and the range is about 7,500 nautical miles. The cruise speed is about Mach 0.82 at 35,000ft altitude.

5.1 Conventional configuration--CB

5.1.1 Three-view drawing

Figure 5-1 shows the Three-view drawing of the conventional configuration.

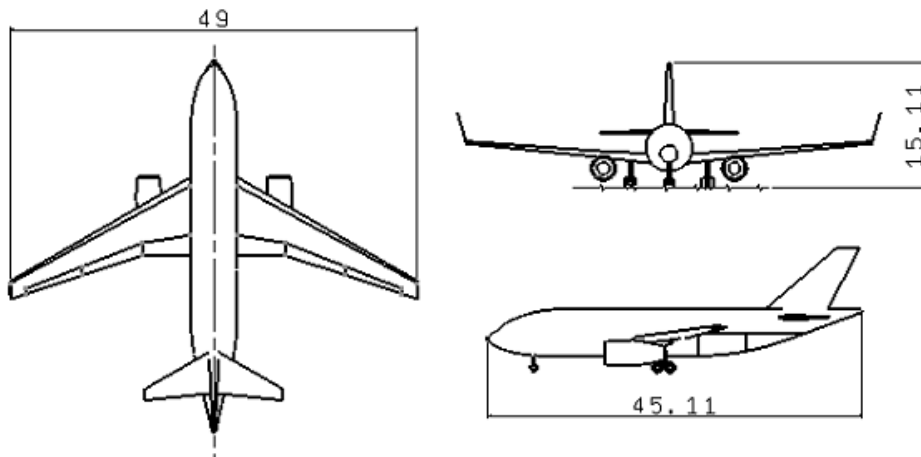


Figure 5-1 Three-view drawing of CB^[1] (Unit:m)

5.1.2 Geometry parameter

The main geometry parameters are listed in Table 5-1.

Table 5-1 Geometry parameters

Reference wing area (m ²)	268
Span (m)	49.2
Aspect ratio	9
Root chord (m)	8.75
Tip chord (m)	2.17
Taper ratio	0.25
Leading edge sweep angle	30.0°
Quarter chord sweep angle	26.5 °
Mean aerodynamic chord (m)	5.83

Supercritical airfoil is chosen for the wing of conventional airplane. The airfoil for root chord is NASA SC2-0714, and the airfoil for tip is NASA SC2-0610. To prevent the wingtip stall at high speed, twist is added for about -3°. In order to enhance the lateral stability, the dihedral angle is 3°.

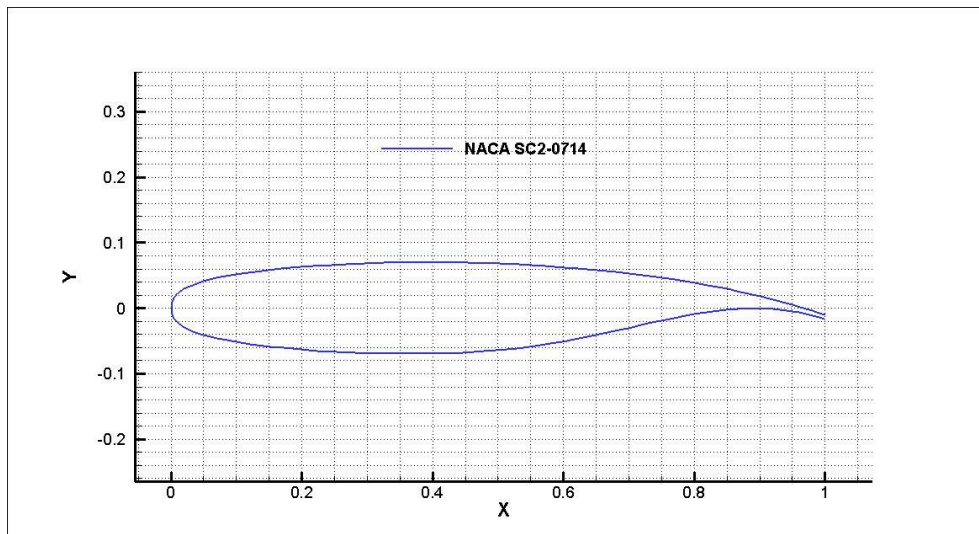


Figure 5-2 NACA SC2-0714

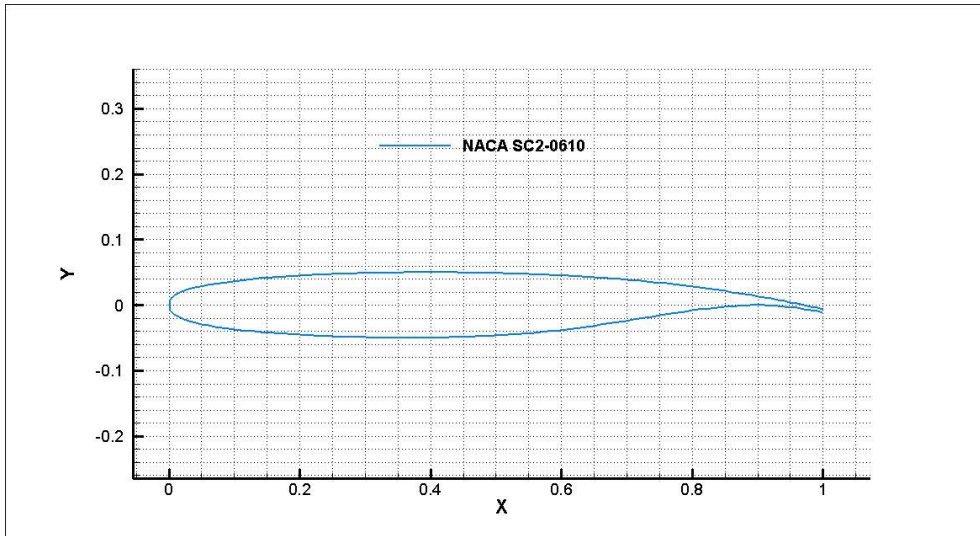


Figure 5-3 NACA SC2-0610

5.1.3 Mass and CG data

According to Ref^[3], the internal arrangement of CB is as following Figure 5-4.

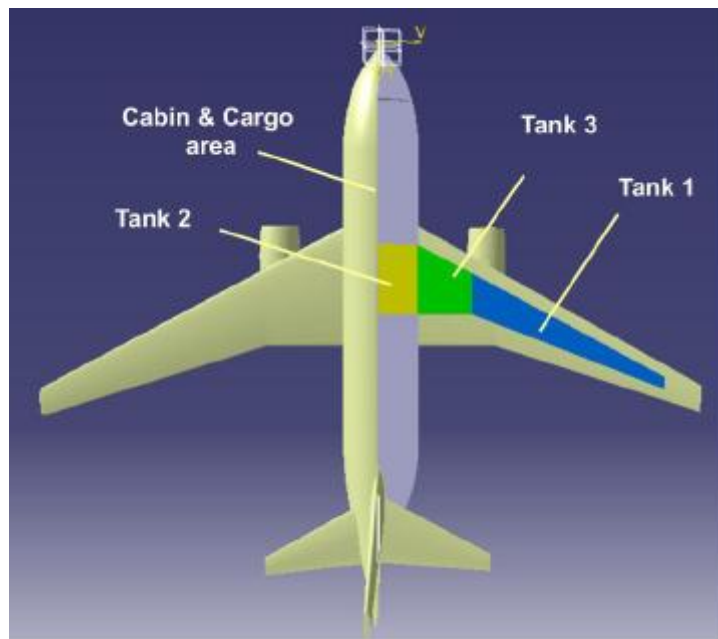


Figure 5-4 Internal arrangement of CB^[3]

According to the output data from in Ref [3], the mass,CG and inertia data are listed in Table 5-2.

Table 5-2 Mass, moments of inertia and CG of CB [3]

MTOW (kg)	187,711.18
OEW(kg)	75,375.48
Fuel(kg)	86,425.64
Payload(kg)	25,910.09
Moments of inertia at MTOW case	
$I_{xx}(\text{kg}\cdot\text{m}^2)$	4,808,833.35
$I_{yy}(\text{kg}\cdot\text{m}^2)$	4,398,130.51
$I_{zz}(\text{kg}\cdot\text{m}^2)$	8,861,314.46
$I_{xy}(\text{kg}\cdot\text{m}^2)$	0.00
$I_{yz}(\text{kg}\cdot\text{m}^2)$	615,132.65
$I_{zx}(\text{kg}\cdot\text{m}^2)$	0.00
Overall CG limit	
Forward CG (m)	19.14 (16.18%MAC)
Aft CG(m)	20.18 (34.60%MAC)

5.2 Flying Wing configuration--FW

5.2.1 Three-view drawing of FW

The flying wing option is shown in the following Figure 5-5.

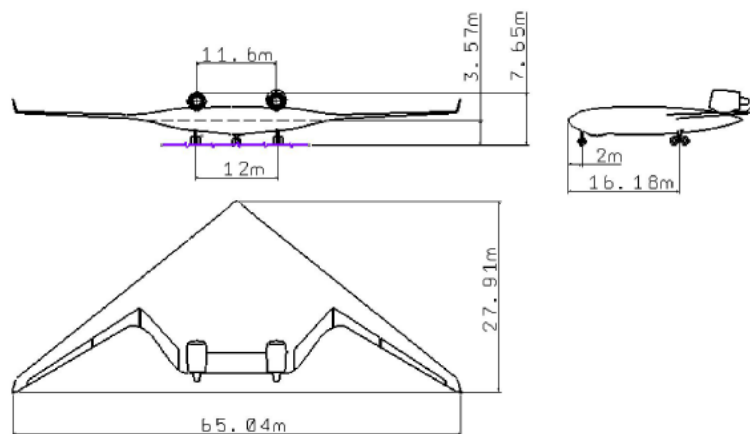


Figure 5-5 Three-view drawing of FW [1]

5.2.2 Geometry parameter

The main geometry parameters are listed in Table 5-3.

Table 5-3 Geometry parameters

Gross area (m ²)	647
Wing loading (kg/m ²)	272
Aspect ratio	6.33
Root chord (m)	25.2
Tip chord (m)	2.0
Taper ratio	0.11
Leading edge sweep angle	39.0 °
Quarter chord sweep angle	34.3 °
Mean aerodynamic chord (m)	12.28

The elevator of FW locates at the rear part of central body, with 9 meters wide and 3 meters long, as shown in Figure 5-8.

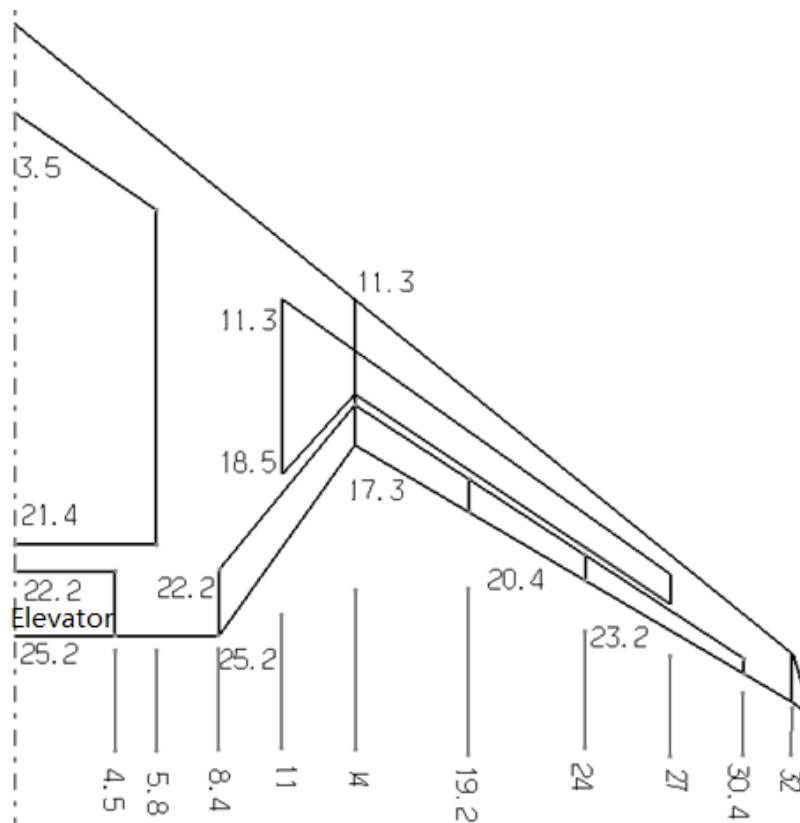


Figure 5-6 Wing geometry of FW^[3] (Unit:m)

According to the internal volume required in the different position, the thickness varies through the wingspan. The airfoil for root chord is modified NASA Symmetric Supercritical airfoil. The thickness position locates at the first kink with nearly 16.4% thickness ratio, and the airfoil for tip is NASA RC-SC2, with about 10% thickness ratio.

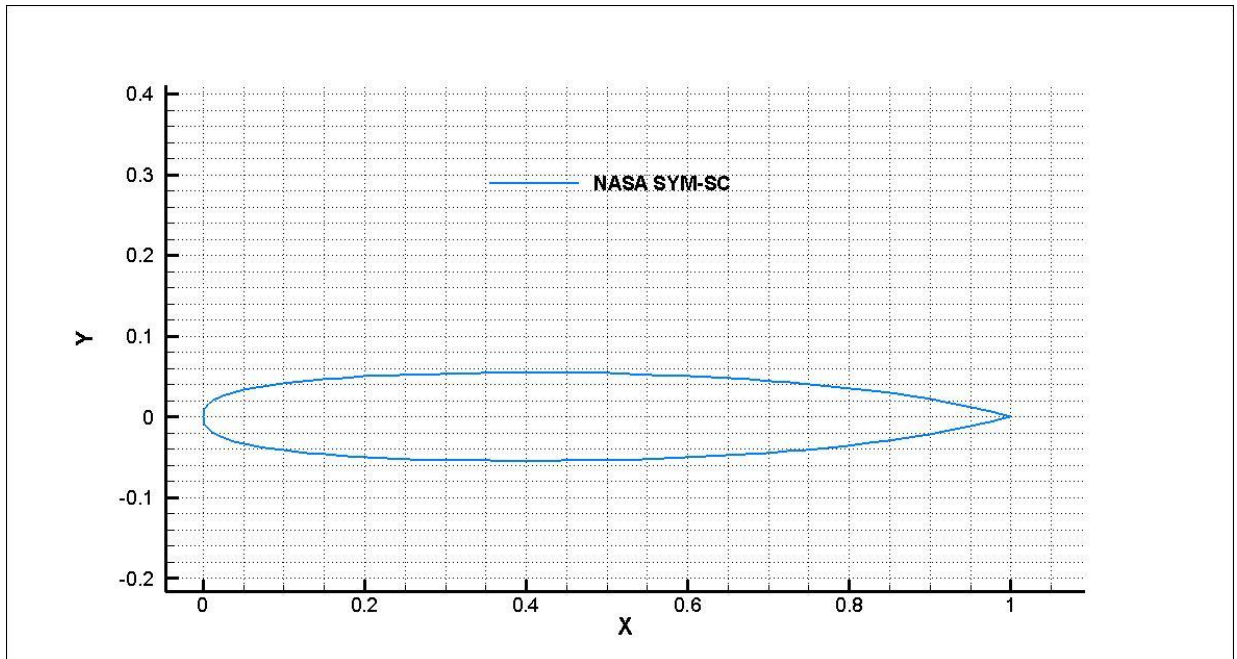


Figure 5-7 NASA SYM SC

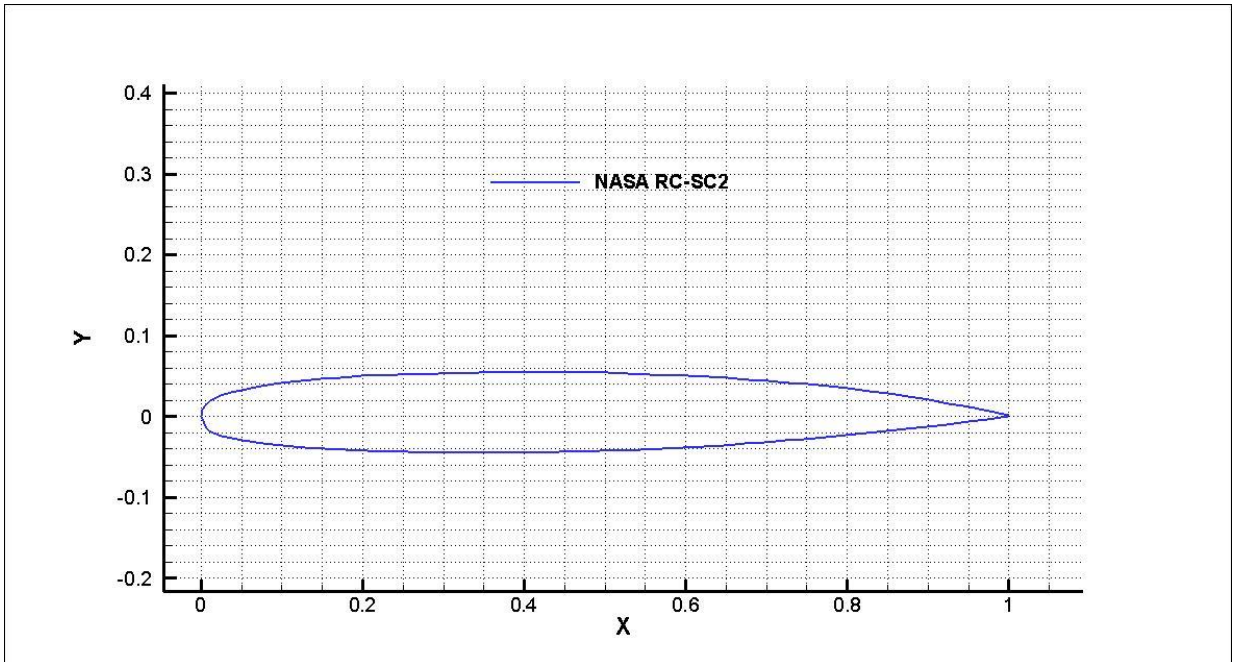


Figure 5-8 NASA RC-SC2

5.2.3 Mass and CG data

According to Ref^[3], the internal arrangement of FW is as following Figure 5-9.

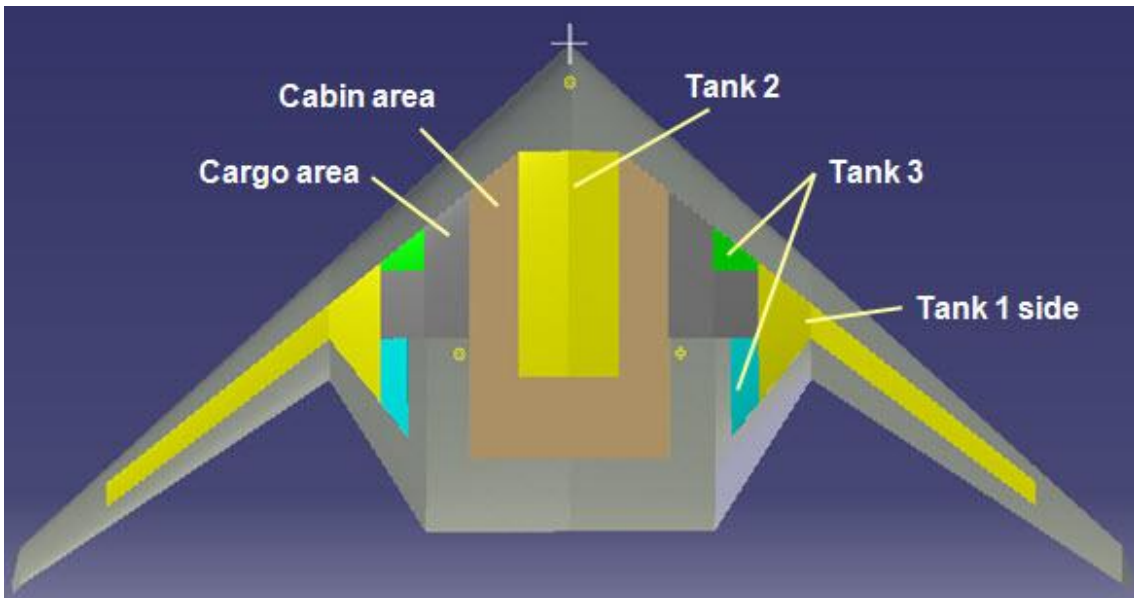


Figure 5-9 Internal arrangement of FW^[3]

According to Ref^[3], the CG and inertia data are listed in Table 5-4.

Table 5-4 Mass, moments of inertia and CG for FW^[3]

MTOW (kg)	176,388.57
OEW(kg)	74,963.95
Fuel(kg)	72,739.03
Payload(kg)	28,686.16
Moments of inertia at MTOW case	
$I_{xx}(\text{kg}\cdot\text{m}^2)$	10,391,139.57
$I_{yy}(\text{kg}\cdot\text{m}^2)$	3,189,119.29
$I_{zz}(\text{kg}\cdot\text{m}^2)$	13,002,958.56
$I_{xy}(\text{kg}\cdot\text{m}^2)$	0.00
$I_{yz}(\text{kg}\cdot\text{m}^2)$	613,176.00
$I_{zx}(\text{kg}\cdot\text{m}^2)$	0.00
Overall CG limit	
Forward CG (m)	13.37 (31.56%MAC)
Aft CG (m)	14.12 (37.72%MAC)

5.3 Blended Wing Body configuration--BWB

5.3.1 Wing geometry

The BWB configuration is as the same configuration as BW-11^[2]. Since the BWB and FW are based on the same requirements, BWB is designed to have the same wing area as the FW configuration.

The wing geometry of BWB is shown in Figure 5-10, the elevator locates at the rear part of central body, with 17.7 meters wide and 2.6 meters long.

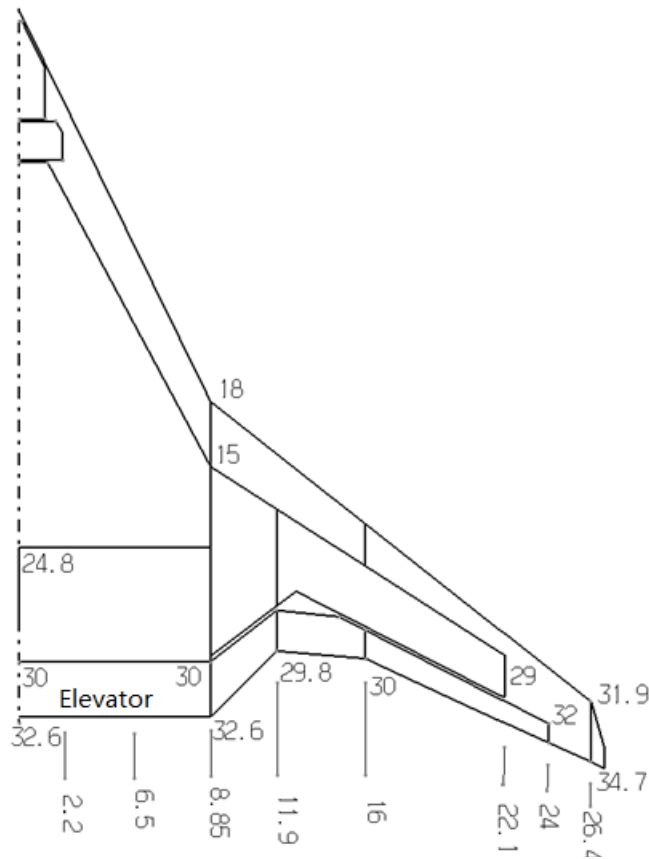


Figure 5-10 Wing geometry of BWB [3]

5.3.2 Geometry parameter

The main geometry parameters are listed in Table 5-5.

Table 5-5 Geometry parameters

Gross area (m ²)	647
Wing loading(kg/m ²)	272
Aspect ratio	4.31
Root chord (m)	32.67
Tip chord (m)	2.72
Taper ratio	0.13
Leading edge sweep angle	68.0 °(inboard), 38.3 °(outboard),
Quarter chord sweep angle	36.9 °
Mean aerodynamic chord (m)	14.71

The airfoil chosen for the inboard body is reflex camber airfoil Eppler 332, which is shown in Figure 5-11. The airfoil chosen for the outboard body is supercritical airfoil NASA SC (2) 0010, shown in Figure 5-12. The dihedral angle is 1.5° for the inboard part and 3° for the outboard part.

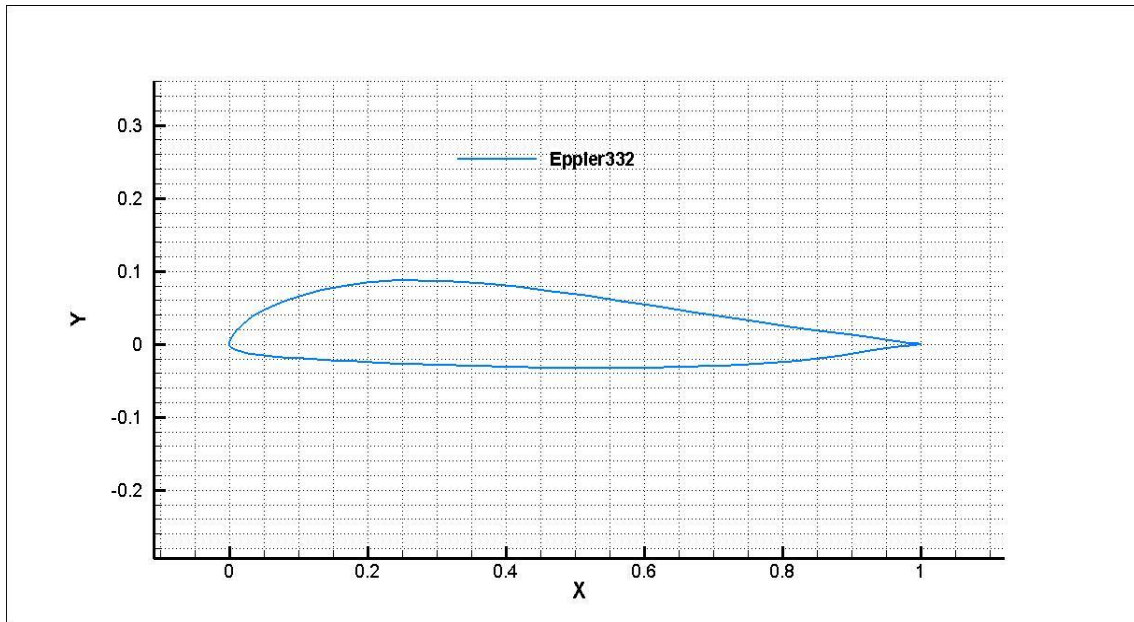


Figure 5-11 Eppler 332 airfoil

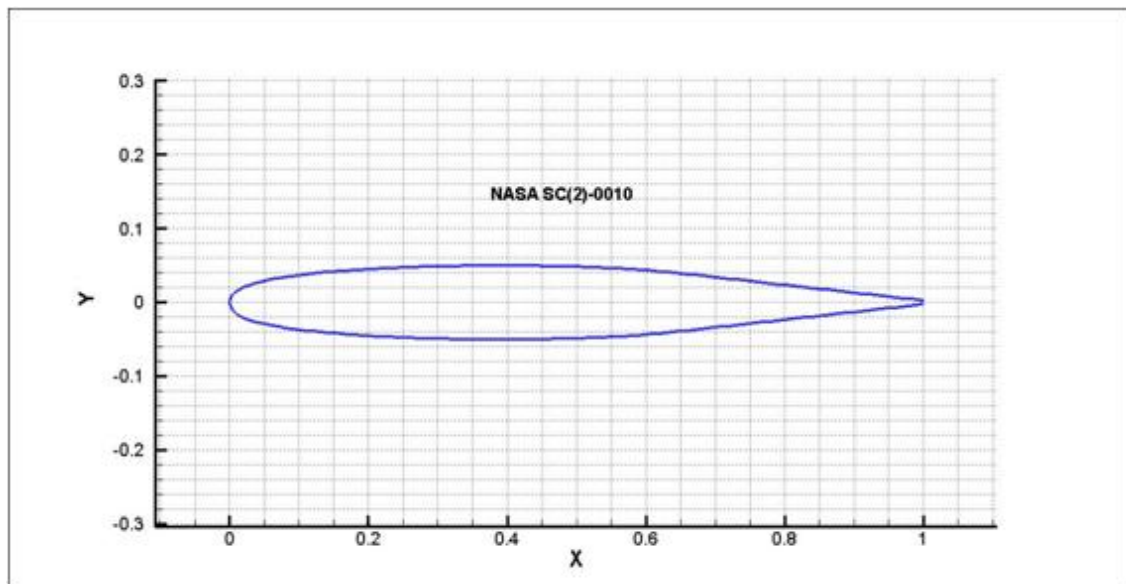


Figure 5-12 NASA SC (2) 0010 airfoil

5.3.3 Mass and CG data

According to Ref ^[3], the internal arrangement of this configuration is shown in the following Figure 5-13:

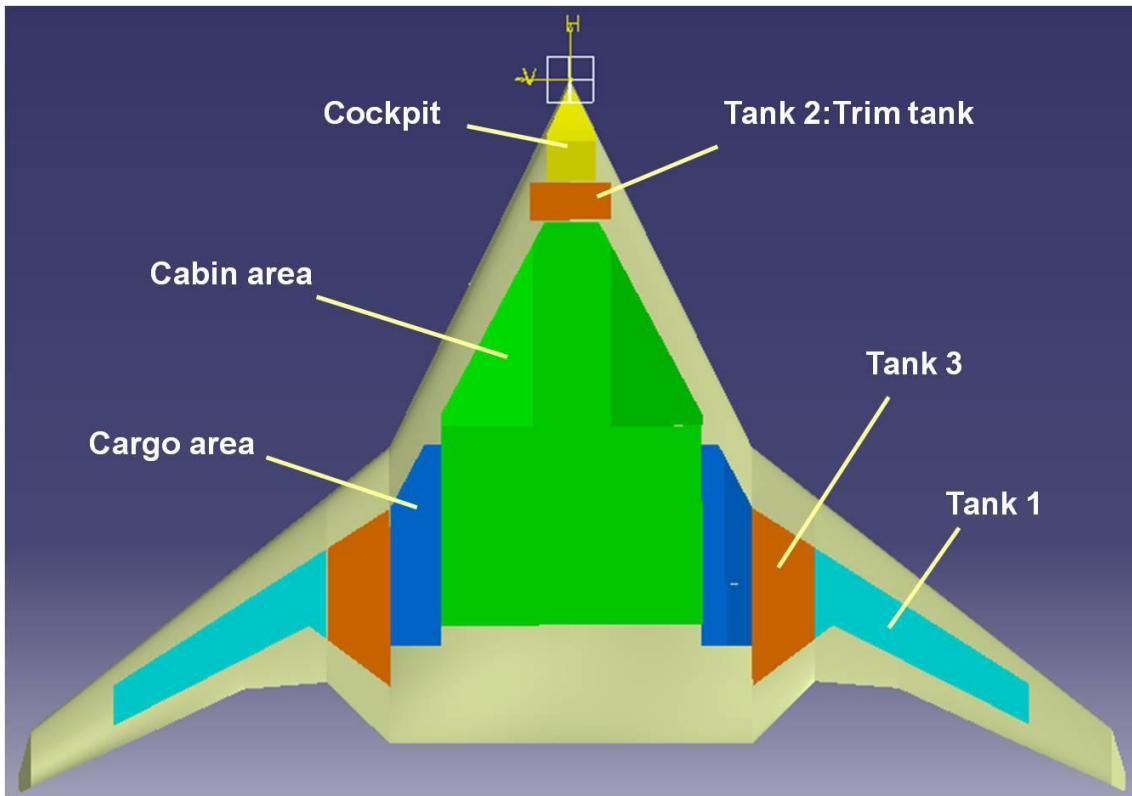


Figure 5-13 Internal arrangement of BWB ^[3]

The mass, CG and inertia data are listed in Table 5-6:

Table 5-6 Mass, moments of inertia and CG for BWB ^[3]

MTOW (kg)	178,103.57
OEW(kg)	75,951.01
Fuel(kg)	73,466.42
Payload(kg)	28,686.16
Moments of inertia at MTOW case	
$I_{xx}(\text{kg}\cdot\text{m}^2)$	12,780,256.37
$I_{yy}(\text{kg}\cdot\text{m}^2)$	7,852,327.89
$I_{zz}(\text{kg}\cdot\text{m}^2)$	20,141,061.18
$I_{xy}(\text{kg}\cdot\text{m}^2)$	0.00

$I_{yz}(\text{kg}\cdot\text{m}^2)$	684,278.12
$I_{zx}(\text{kg}\cdot\text{m}^2)$	0.00
Overall CG limit	
Forward CG (m)	19.05 (17.68% MAC)
Aft CG (m)	22.13 (38.45% MAC)

5.4 AVL models

Based on geometry data of the above configuration, the AVL models have been set up, and shown in the following Figures from 5-14 to 5-16.

For the conventional aircraft, the wing, elevator and fin are treated as lifting surfaces in AVL, while fuselage is considered to be slender body without producing lift.

For the flying wing or blended wing body configuration, the whole “wing” area are lifting surfaces.

As indicated in Chapter 4, the mesh number and mesh distribution has a significant impact on the results, and that is why all the mesh parameters are carefully considered for the aim of obtain reasonable data.

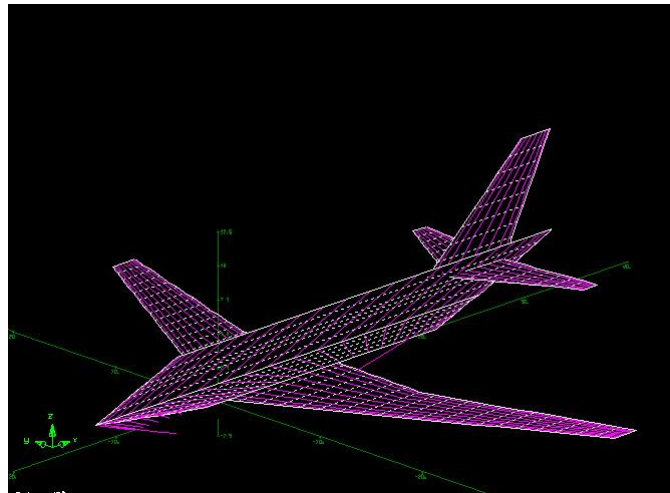


Figure 5-14 Conventional AVL model

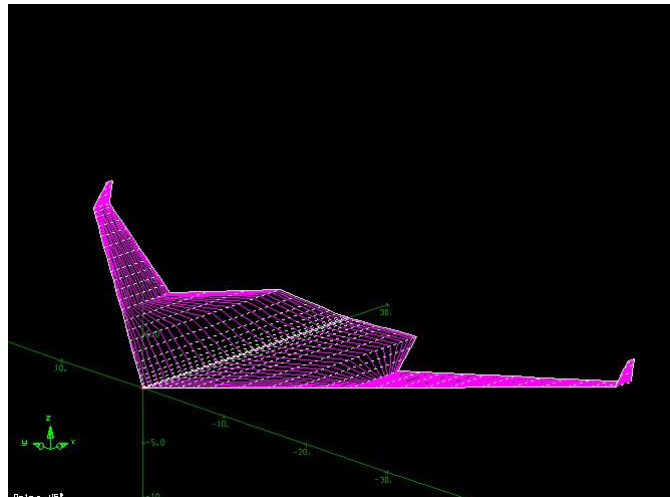


Figure 5-15 Flying wing AVL model

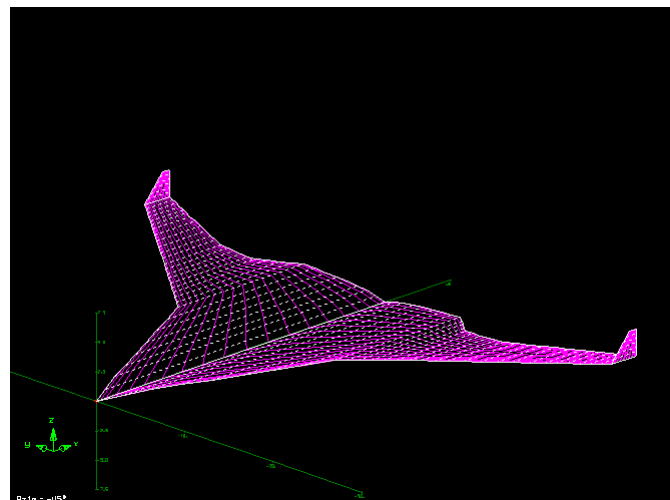


Figure 5-16 Blended wing body AVL model

5.5 Summary

In this chapter, three different configurations have been provided, which were designed based on the same passenger number and range requirements.

Besides, according to the internal arrangements, the mass and CG data have been given by the Ref^[3]. Based on the geometry, the AVL models have been set up. In the following chapter 6 and 7, the aerodynamic data are calculated based on the models introduced in this chapter. In chapter 8, some modifications are made to compare the effects of changing geometry parameters on BWB.

6 Aerodynamic Characteristics Comparison

This chapter compares the aerodynamic characteristics between the three different configurations. The comparison including the following aspects: lift, drag, pitching moment and aerodynamic derivatives. The aerodynamic forces data and aerodynamic derivatives data are generated by running AVL simulation.

6.1 Lift

The lift curves of three configurations are presented in Table 6-1. It is clear that the conventional configuration has the highest lift curve slope while the blended wing body has the least.

The main reason causes the result is the difference on aspect ratio. Theoretically, lift curve slope raises as the aspect ratio increases. For the conventional configuration, the aspect ratio is 9.0; for the flying wing configuration, the aspect ratio is 6.3; for the blended wing body, the value is only 4.3. Therefore, the conventional configuration owns the highest lift curve slope. Table 6-2 lists the zero lift angle of attack at different Mach number.

Table 6-1 Lift curve slope of different Mach number (unit: rad^{-1})

	Ma=0.5	Ma=0.6	Ma=0.7	Ma=0.82
CB	5.68	5.95	6.33	6.92
FW	3.85	4.00	4.21	4.56
BWB	3.51	3.64	3.83	4.19

Table 6-2 Zero lift angle of attack of different Mach number

	Ma=0.5	Ma=0.6	Ma=0.7	Ma=0.82
CB	-3.76	-3.80	-3.86	-3.98
FW	0.71	0.72	0.72	0.73
BWB	0.41	0.42	0.43	0.43

One of the most significant differences between conventional and blended wing body aircraft is that the “body” of blended wing body generates the lift. Additionally, according to the weight predicted in Ref ^[3], there is reduction of

weight of the cruise condition for flying wing and blended wing body than the conventional configuration. Therefore, with extended lift generation surface as well as reduced weight, less lift coefficient is need for the blended wing body aircraft at cruise condition.

Since the mass varies during the flight process, 95% of the MTOW is chosen as start point of cruise condition and the required lift coefficient is listed in Table 6-3.

Table 6-3 Lift coefficient

Configuration	Mass(kg)	Cruise Mach number	Dynamic pressure (N/m²)	Reference area (m²)	Cruise lift coefficient
CB	178,325	0.82	1.122E+04	268	0.362
FW	167,568	0.82	1.122E+04	647	0.224
BWB	169,197	0.82	1.122E+04	647	0.226

6.2 Drag

The drag prediction is based on the method introduced in Chapter 3.1.2.A direct comparison of form drag and wave drag in Mach 0.82 is listed in Table 6-4.

The wetted area of CB is 1160 m², while FW and BWB is 1362 m² and 1414 m² relatively. Taken the Reynolds number into consideration, the total friction force is at the same level. However, the reference area of FW and BWB is larger than the CB. Since the form drag most comes from friction drag, then the value of FW and BWB are much less than CB.

In terms of wave drag, for the CB, the main sources come from fuselage and wing. The average wing thickness to chord ratio is about 12% for CB. The value is about 16.5% for FW, and 12% for BWB. Since BWB has the largest sweep angle among these three configurations while relative thin thickness to chord

ratio, the wave drag coefficient is the least. The thickness to chord ratio of FW is really large, that is why FW has the highest wave drag coefficient.

The aspect ratio for CB is 9, and that makes the least induced drag factor of those three configurations. The aspect ratio for BWB is 4.3, and then the most induced drag factor will be leaded.

Table 6-4 Form drag and wave drag at Mach 0.82

	Zero lift drag coefficient C_{DF}	Wave drag coefficient C_{DW}	Induced drag factor K
CB	0.0153	0.0009	0.0472
FW	0.0073	0.0011	0.0535
BWB	0.0072	0.0005	0.0590

Based on the method introduced in Chapter 3.1.2, the drag polars of three configurations for cruise condition could be described as Equations 6-1 to 6-3.

The drag polar of CB:

$$C_D = 0.0162 + 0.0472C_L^2 \quad (6-1)$$

The drag polar of FW:

$$C_D = 0.0084 + 0.0535C_L^2 \quad (6-2)$$

The drag polar of BWB:

$$C_D = 0.0077 + 0.0590C_L^2 \quad (6-3)$$

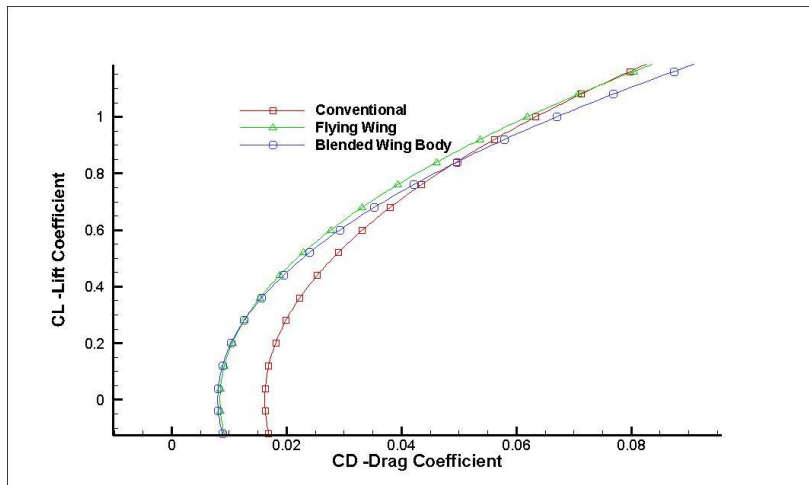


Figure 6-1 Drag Polar

Since the cruise lift coefficient is calculated as shown in Table 6-3, the drag coefficient could be obtained from drag polar. Further, the lift to drag ratio could be computed. As illustrated in Table 6-5, the BWB configuration has the highest lift to drag ratio, which achieves 21.09, about 31% higher than the conventional one. The FW configuration is 20.21 with about 24% increase than the CB.

Table 6-5 Lift to drag ratio on cruise condition

	Lift coefficient	Drag coefficient	Lift to drag ratio
CB	0.362	0.0223	16.17
FW	0.224	0.0110	20.21
BWB	0.226	0.0107	21.09

6.3 Pitching moment

The horizontal axis of Figure 6-2 is the lift coefficient, and the vertical axis is pitching moment coefficient. The reference point to calculate the pitching moment is one-quarter MAC.

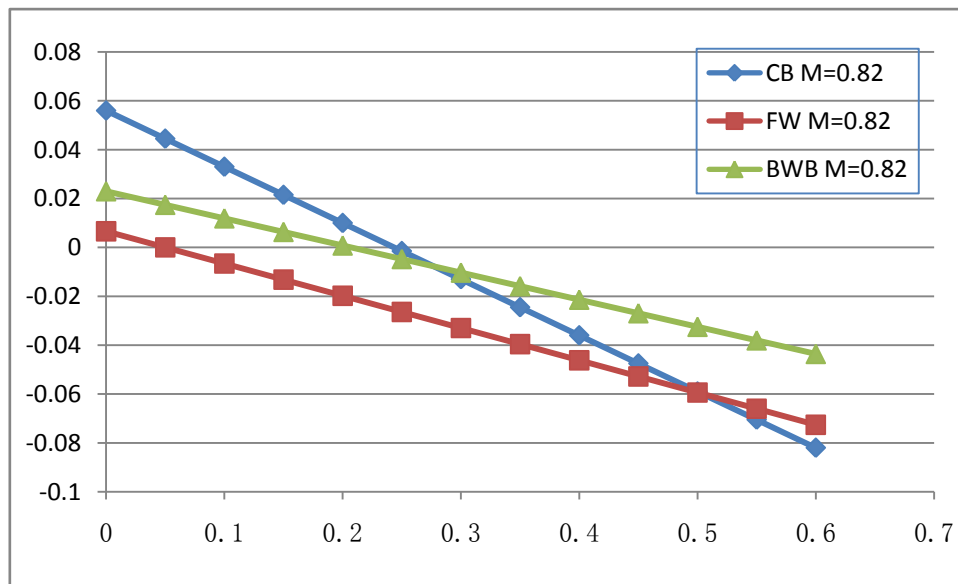


Figure 6-2 C_M-C_L curve

Zero lift pitching moment coefficient is listed in Table 6-6, it could be found that the CB has the largest number of zero lift pitching moment coefficient C_{M0} about 0.056, while FW has the least about 0.006.

For CB, when the lift of the whole airplane is zero, the horizontal tail will generate negative lift and then accompany a nose up pitching moment, which produces a relative large C_{M0} ; for the FW, since its symmetrical airfoil with relatively small twist angle, the C_{M0} is quite small; for the BWB, due to the reflex camber airfoil and bigger twist angle, the C_{M0} will be larger than FW.

Since the one-quarter MAC is chosen to calculate the pitching moment, the slope of $C_M - C_L$ for CB has the lowest value of -0.23, while BWB is only -0.11. One thing has to bear in mind is that, the $C_M - C_L$ slope changes as the reference point moves.

Table 6-6 Zero lift pitching moment and $C_M - C_L$ slope

	Zero lift pitching moment coefficient C_{M0}	$\frac{dC_M}{dC_L}$
CB	0.056	-0.23
FW	0.006	-0.13
BWB	0.020	-0.11

6.4 Aerodynamic derivatives

The aerodynamic derivatives of the three configurations at different Mach numbers are listed in the following tables from Table 6-7 to Table 6-9. Those data are calculated by AVL.

Table 6-7 Aerodynamic derivatives data of CB at different Mach numbers

	Ma	0.60	0.70	0.82
Longitudinal Aerodynamic Derivatives	$C_{L\alpha}$	5.9523	6.3336	6.9212
	$C_{L\delta_e}$	0.0154	0.0162	0.0177
	$C_{M\delta_e}$	-0.0459	-0.0486	-0.0538
	$C_{M\alpha}$	-2.0471	-2.2079	-2.5204
	C_{Lq}	14.8510	15.7368	17.4434
	C_{Mq}	-25.6882	-27.2181	-30.1476
Lateral-directional Aerodynamic Derivatives	$C_{l\beta}$	-0.1061	-0.1115	-0.1216
	$C_{n\beta}$	0.1089	0.1122	0.1179
	C_{lp}	-0.5140	-0.5404	-0.5884
	C_{np}	-0.0195	-0.0223	-0.0275
	C_{lr}	0.1255	0.1338	0.1504
	C_{nr}	-0.1507	-0.1544	-0.1606
	$C_{l\delta_\alpha}$	0.0028	0.0029	0.0032

Table 6-8 Aerodynamic derivatives data of FW at different Mach numbers

	Ma	0.60	0.70	0.82
Longitudinal Aerodynamic Derivatives	$C_{L\alpha}$	4.0012	4.2109	4.5929
	$C_{L\delta_e}$	0.0076	0.0080	0.0086
	$C_{M\delta_e}$	-0.0035	-0.0038	-0.0045
	$C_{M\alpha}$	-0.1925	-0.2320	-0.3120
	C_{Lq}	4.6572	4.9033	5.3550
	C_{Mq}	-1.8492	-1.9949	-2.2768
Lateral-directional Aerodynamic Derivatives	$C_{l\beta}$	-0.0570	-0.0594	-0.0633
	$C_{n\beta}$	0.0068	0.0071	0.0075
	C_{lp}	-0.2955	-0.3090	-0.3324
	C_{np}	-0.0070	-0.0074	-0.0081
	C_{lr}	0.0568	0.0600	0.0658
	C_{nr}	-0.0102	-0.0105	-0.0110
	$C_{l\delta_\alpha}$	0.0018	0.0019	0.0020

Table 6-9 Aerodynamic derivatives data of BWB at different Mach numbers

	Ma	0.60	0.70	0.82
Longitudinal Aerodynamic Derivatives	$C_{L\alpha}$	3.6488	3.8400	4.1967
	$C_{L\delta_e}$	0.0137	0.0145	0.0161
	$C_{M\delta_e}$	-0.0060	-0.0066	-0.0078
	$C_{M\alpha}$	-0.4319	-0.4956	-0.6245
	C_{Lq}	4.2632	4.5297	5.0437
	C_{Mq}	-1.7001	-1.8383	-2.1150
Lateral-directional Aerodynamic Derivatives	$C_{l\beta}$	-0.0816	-0.0830	-0.0855
	$C_{n\beta}$	0.0048	0.0050	0.0056
	C_{lp}	-0.2950	-0.3085	-0.3325
	C_{np}	-0.0157	-0.0143	-0.0115
	C_{lr}	0.0740	0.0758	0.0790

	Ma	0.60	0.70	0.82
	C_{nr}	-0.0075	-0.0079	-0.0087
	$C_{l\delta_\alpha}$	0.0023	0.0024	0.0027

From the above tables, some important features could be analysed as follows:

In terms of the static derivatives:

CB owns the highest derivative C_{Ma} obviously, due to the influence of horizontal tail. It should be noticed that BWB has larger C_{Ma} than FW. This comes from the fact that the longer relative distance between aerodynamic centre and CG.

$C_{n\beta}$ is the directional stability derivative. The directional stability derivatives of both BWB and FW are dramatically lower than the CB due to the lack of vertical tail.

$C_{l\beta}$ is the lateral stability derivative. Obviously, CB has biggest lateral stability due to its conventional configuration. Although BWB experiences much lower lateral stability than the conventional, it has better performance than FW in this aspect. However, the differences of lateral stability derivatives of the three configurations are not as significant as the longitudinal and directional derivatives.

In terms of dynamic derivatives:

C_{Mq} is the pitching damping derivative, and CB has the highest value while the FW has the least. The horizontal tail is the main component influence the pitching damping ratio. Because of both the FW and BWB do not have horizontal tail and that feature significantly reduces the pitching damping derivative C_{Mq} .

C_{lp} is the roll damping derivative. BWB and FW have nearly the same roll damping, probably because of the highly integrate wing-body configuration and same wing areas. The CB has higher roll damping mainly due to the contribution of tail.

C_{nr} is the yaw damping derivative. The vertical tail plays the most important role in the yaw damping. Because of the lack of vertical tail, both FW and BWB have much lower yaw damping compared to the conventional aircraft, and the values are not at the same level. FW possess a slightly higher yaw damping than BWB.

6.5 Summary

The main conclusions of this chapter are follows:

1. Benefit from the less weight (estimated in Ref ^[3]) and large lift generating surface, there is less cruise lift needed for BWB and FW configuration in the cruise condition.
2. For the BWB and FW configuration, the form drag coefficient is remarkably decreased and the lift to drag ratio at cruise condition has dramatically risen. The BWB configuration has almost 31% increments on the lift to drag ratio than the conventional configuration, while the FW increases about 24%.
3. The reduction of aspect ratio reduces the lift slope of BWB, also causes the increase of induced drag.
4. Because of the absence of horizontal tail, the longitudinal static and dynamic derivatives of FW and BWB are much less than the CB. Due to the lack of vertical tail, the directional derivatives of FW and BWB are deteriorated. In terms of lateral derivatives, there is no significant difference between the three configurations.

7 Stability Characteristics Comparison

This chapter compares the stability characteristics of the conventional, flying wing and blended wing body configuration. The comparisons contain four parts: the first part is about longitudinal static stability, followed by the longitudinal dynamic stability, then the lateral-directional static stability is discussed, and the last is the lateral-directional dynamic stability.

The mass, CG and moment of inertia data are needed for stability analysis, and those data are taken from Ref^[3].

7.1 Calculation condition

For the aim of fair comparison, the calculation condition should be unified.

The flight condition is decided as cruise altitude at 35,000 ft, with Mach number 0.82. Full payload and half fuel condition is chosen to analysis the stability characteristics in this chapter. The corresponding mass, CG and inertia data are listed in Table 7-1.

Table 7-1 Mass, CG and moments of inertia

Configuration	Mass(kg)	X_CG(m)	I_{xx}(kg*m²)	I_{yy}(kg*m²)	I_{zz}(kg*m²)
CB	144,498	19.525	2,508,355	4,331,647	6,515,922
FW	139,808	13.367	7,490,258	2,931,267	9,918,504
BWB	141,136	21.308	7,716,710	5,575,448	12,818,763

7.2 Longitudinal static stability characteristics

7.2.1 Static margin

The longitudinal static stability represents that whether the aircraft could recover to previous stable condition after disturbance in pitching. The condition of longitudinal static stability could be defined as:

$$\frac{dC_M}{dC_L} < 0 \quad (7-1)$$

The relative position of CG (centre of gravity) and NP (neutral point) decides the static margin. If the CG is forward the NP, the aircraft will be stable, and vice versa. The static margin is defined as Equation 7-2. The value of static margin indicates whether the aircraft is safe and how safety the aircraft is.

$$K_n = h_n - h = -\frac{dC_M}{dC_L} \quad (7-2)$$

Where, K_n is static stability margin, h_n is the neutral point on the reference chord, h is the centre of gravity on the reference chord.

For the CB configuration, the neutral point locates at 46.70% \bar{c} at Mach number 0.82. The static margin of different cases are listed in Table 7-2 from Ref^[3]. It is stable for both forward CG and aft CG position, and the minimum static margin is about 12.40% \bar{c} .

Table 7-2 CG position and static margin of CB^[3]

Cases	CG position	Static margin
MTOW	23.32% \bar{c}	23.68% \bar{c}
No payload full fuel	16.18% \bar{c}	30.82% \bar{c}
No fuel full payload	34.60% \bar{c}	12.40% \bar{c}
No fuel no payload	24.60% \bar{c}	22.40% \bar{c}
Half fuel	22.64%-28.07% \bar{c}	18.93% -24.06% \bar{c}

For the FW configuration, the location of neutral point is 38.2% \bar{c} at Mach number 0.82. The static margins of different cases are listed in Table 7-3 from Ref^[3]. The minimum static margin is only 0.48% \bar{c} , which indicates it is a weak stable position.

Table 7-3 Static margin of FW ^[3]

Cases	Range of CG	Static margin
MTOW	31.56% \bar{c}	6.64% \bar{c}
No payload full fuel	34.54% \bar{c}	3.66% \bar{c}
No fuel full payload	31.87% \bar{c}	6.33% \bar{c}
No fuel no payload	37.72% \bar{c}	0.48% \bar{c}
Half fuel	31.46%-36.04% \bar{c}	2.16%-6.74% \bar{c}

From the data estimated by ESDU, the location of neutral point for BWB is 36.1% \bar{c} at Mach number 0.82. The static margins of different cases are listed in Table 7-4 according to the CG data from Ref ^[3], one particular case shows that the BWB with full fuel and no payload condition is unstable. The BWB configuration has relatively extended static margin than the FW configuration.

Table 7-4 Static margin of BWB ^[3]

Cases	Range of CG	Static margin
MTOW	33.02% \bar{c}	3.08% \bar{c}
No payload full fuel	38.45% \bar{c}	-2.35% \bar{c}
No fuel full payload	17.68% \bar{c}	18.42% \bar{c}
No fuel no payload	23.25% \bar{c}	12.85% \bar{c}
Half fuel	25.10%-30.33% \bar{c}	5.77% -11% \bar{c}

7.2.2 Trim

The trim ability is of vital importance for tailless configurations. For conventional airplane, since there is a large horizontal tail and long aerodynamic force arm, the trim is relatively much easier than the tailless airplane. This section will compare the trim ability of FW and BWB configuration.

The airplane should have the ability to trim at all flight conditions. The position of aerodynamic centre will move as the Mach number changes. The CG moves in the criterion between the forward CG and aft CG. Therefore, four extreme

conditions have been checked as two Mach number boundaries (Mach 0.2 and Mach 0.82) and two CG position boundaries (forward CG and aft CG).

The horizontal axis of Figure 7-1 shows the angle of attack, while the vertical axis indicates the deflection degree of elevator for trim. Same definition could also be used in Figure 7-2, 7-3 and 7-4.

Taking forward CG as the reference point and the flight Mach number 0.82, Figure 7-1 illustrates the elevator deflection angle of both configurations at different angle of attack. Generally, there will be larger elevator deflection angle for BWB than the FW. This may be caused by the reason that the BWB is more stable on the forward CG condition.

As shown in Table 7-4, the forward CG of FW is at MTOW case with the static margin of $6.64\% \bar{c}$. While, the Table 7-5 indicates that the forward CG of BWB is at no fuel full payload condition, with the static margin about $18.42\% \bar{c}$.

Therefore, the BWB configuration is more stable on forward CG condition. The more stable the airplane is, the more difficult to control it. Then, the elevator has to be deflected at a relative large angle for trimming.

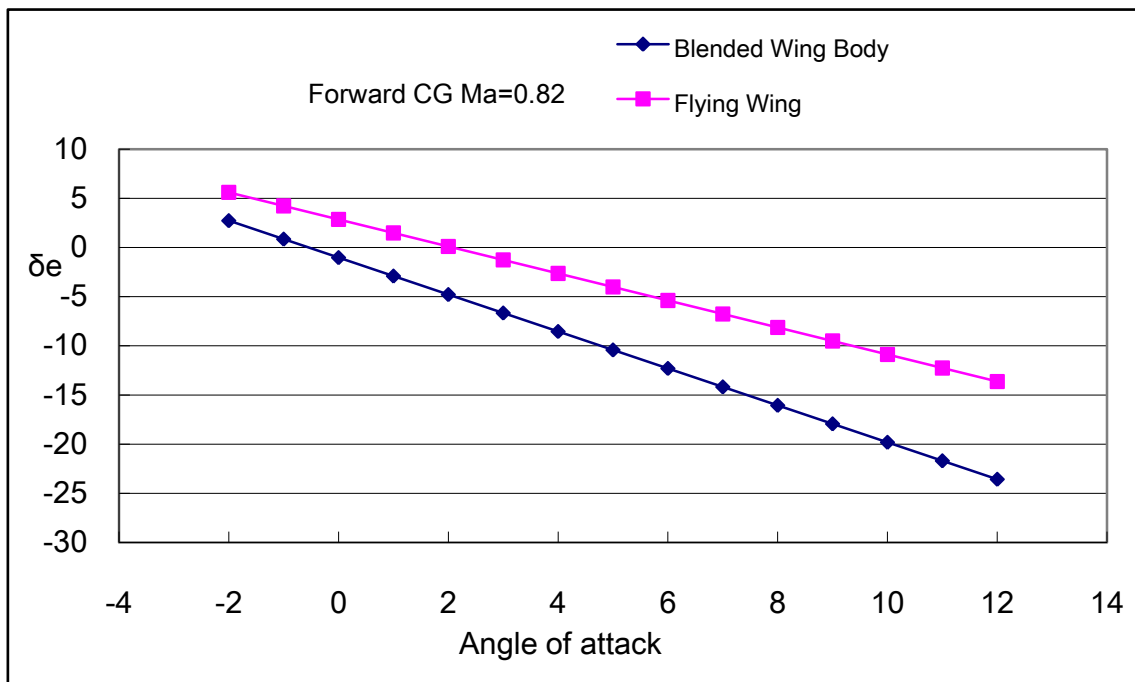


Figure 7-1 Elevator deflection angle (Forward CG, Ma=0.82)

The same reason could also explain the result shown in Figure 7-2. There is larger elevator deflection angle needed for trimming the BWB, which is also taking forward CG as reference point while the Mach number changes to 0.2.

Commonly, the forward CG needs the largest elevator deflection degree. From Figure 7-2, when the angle of attack reaches 12° , the elevator deflection angle still less than 25° , which is still in the acceptable criterion, according to the specification ^[1].

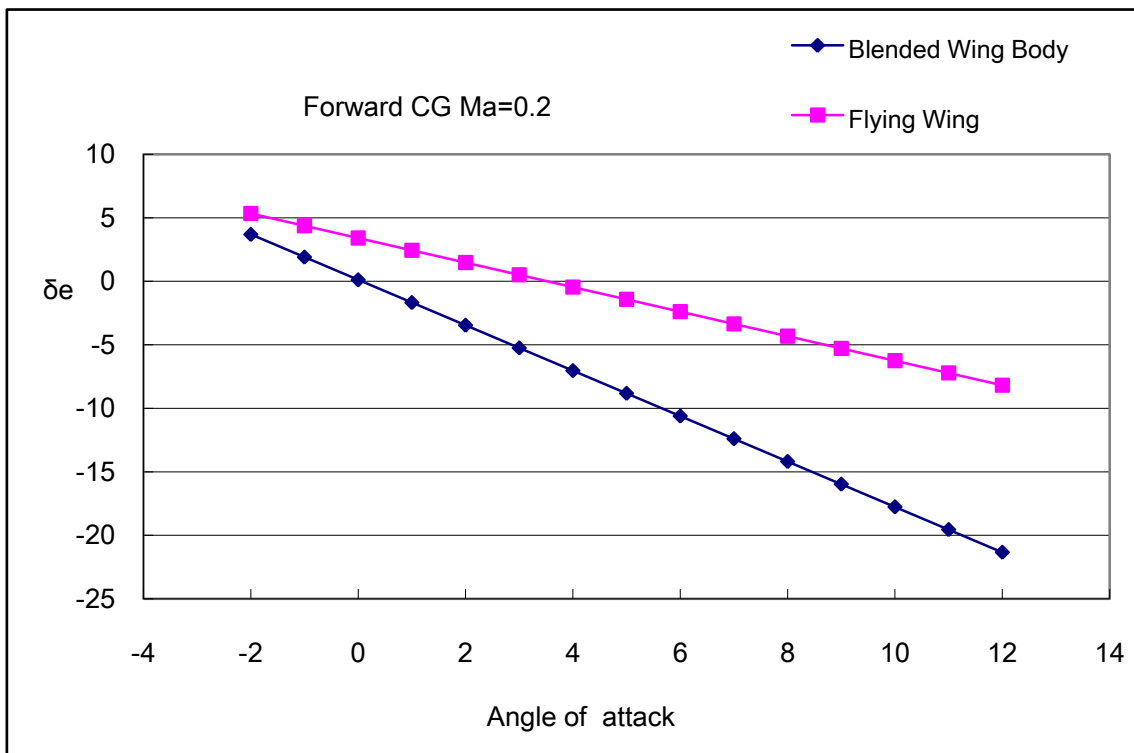


Figure 7-2 Elevator deflection angle (Forward CG, Ma=0.2)

In Figure 7-3, the slope of blue line is positive which means the BWB is unstable when flying at Mach number 0.82 and taking aft CG as reference point. This could be proved by Table 7-4 that the aft CG for BWB is at no payload full fuel condition, the static margin is $-2.35\% \bar{c}$.

From Figure 7-3, it could be found that only small deflection angle is need for trim at Ma 0.82, taking aft CG as reference point.

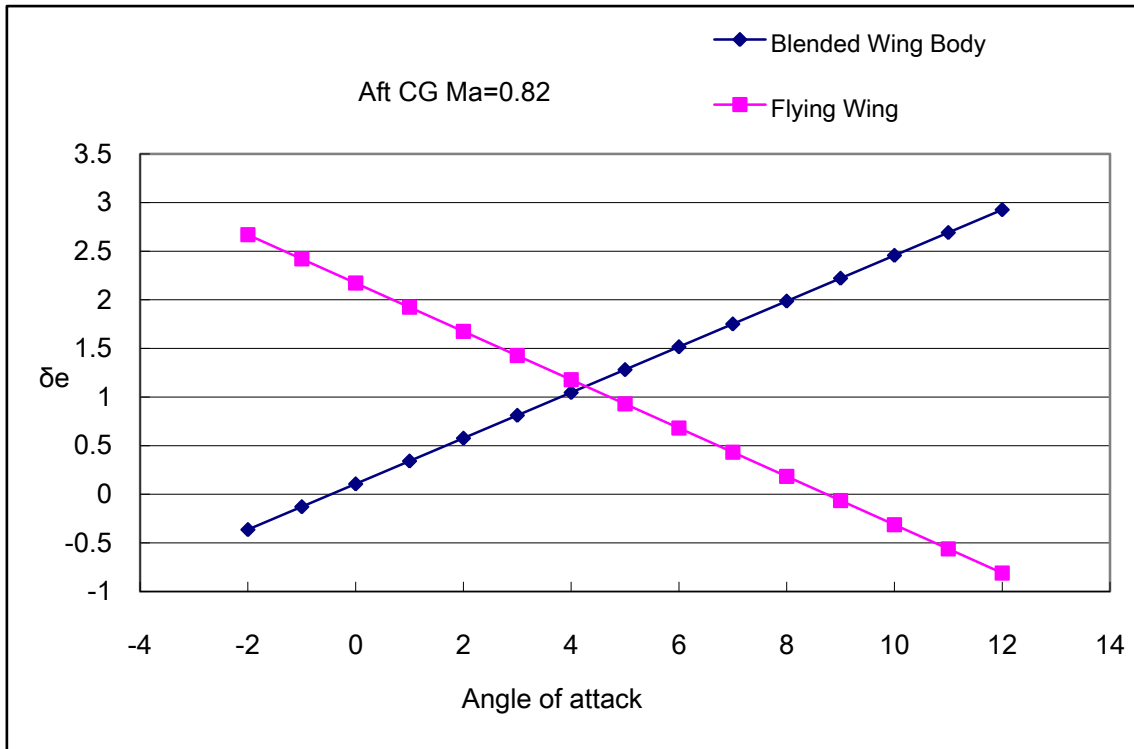


Figure 7-3 Elevator deflection angle (Aft CG, Ma=0.82)

The Figure 7-4 shows that both the flying wing and blended wing body are unstable when flying at Mach 0.2 and taking aft CG as reference point. As the angle of attack increase from -2° to 12° , the elevator deflection angle of BWB and FW will also increase about 8° correspondingly. However, both the BWB and FW deflection angles are still far away from the 25° deflection limitation.

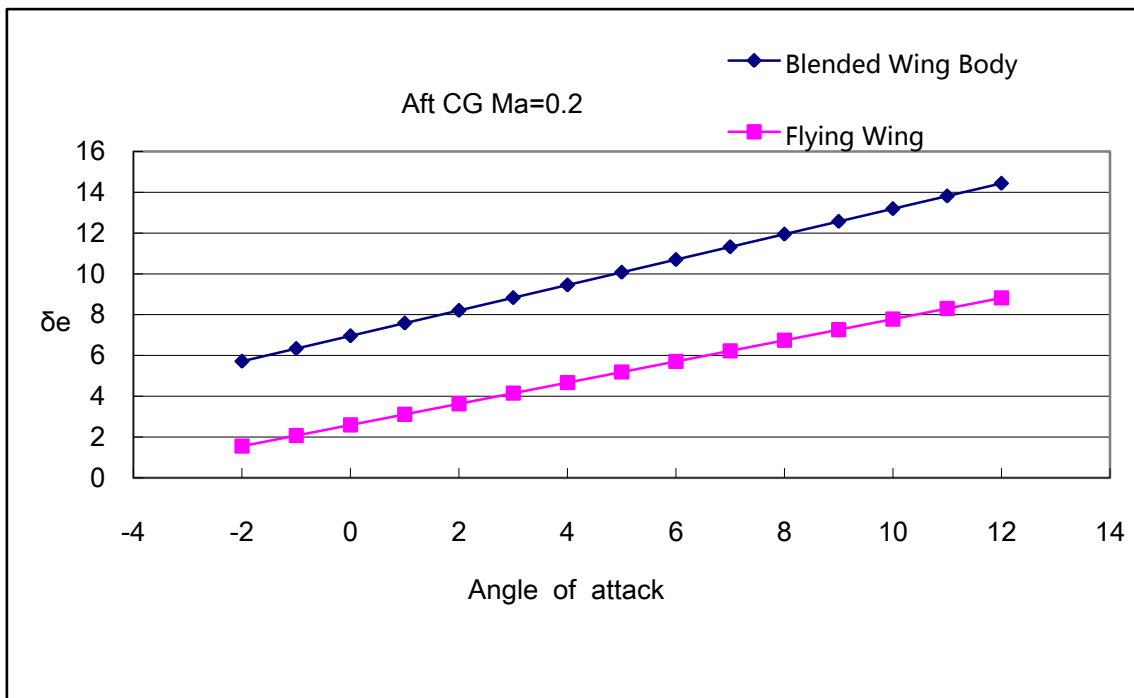


Figure 7-4 Elevator deflection angle (Aft CG, Ma=0.2)

7.3 Longitudinal dynamic stability characteristics

7.3.1 Phugoid mode

Typically, the phugoid mode is a long period, low frequency oscillation ^[20]. Because of large inertia and momentum involving in the process, the motion of phugoid mode is relatively slow and the angular acceleration is really small.

From Table 7-5, it seems that the phugoid mode damping ratios of FW and BWB are less than CB. According to explanation from M.V.Cook^[20], the reason may lie in the fact that less drag of FW and BWB than the CB. Since FW and BWB have the higher lift to drag ratio, which will makes them less damped in the phugoid mode.

Table 7-5 Phugoid mode damping ratio and frequency

Configuration	Ma=0.60		Ma=0.70		Ma=0.82	
	ζ_p	ω_p (rad/s)	ζ_p	ω_p (rad/s)	ζ_p	ω_p (rad/s)
CB	0.0678	0.0954	0.0551	0.0816	0.0490	0.0695
FW	0.0305	0.0899	0.0284	0.0763	0.0313	0.0654
BWB	0.0342	0.0942	0.0311	0.0795	0.0326	0.0677

Compare the phugoid damping ratio in Table 7-5 and the phugoid damping ratio requirement in Table 2-2, both the FW and BWB could only meet the Level 2 requirement, while the CB could achieve the Level 1 requirement.

7.3.2 Short period mode

Commonly, the short period mode is a relatively short period, high frequency damped oscillation in pitching.

From the Table 7-6, the short period mode damping ratios of the three configurations are nearly at the same level.

Table 7-6 Short period mode damping ratio and frequency

Configuration	Ma=0.60		Ma=0.70		Ma=0.82	
	ζ_{sp}	ω_{sp} (rad/s)	ζ_{sp}	ω_{sp} (rad/s)	ζ_{sp}	ω_{sp} (rad/s)
CB	0.3586	2.1842	0.3645	2.6532	0.3754	3.3276
FW	0.5093	1.9466	0.4987	2.4798	0.4867	3.3478
BWB	0.3428	2.1993	0.3422	2.7474	0.3439	3.6124

From the approximate Equation 3-34 and 3-35, it could be found that several main factors influencing the short period mode: moment of inertia in pitch I_{yy} , pitching damping derivative C_{Mq} , wing area S and reference chord length \bar{c} . Because the FW and BWB have no horizontal tail, the pitching damping derivative C_{Mq} is far less than the CB. Besides, the FW and BWB have larger moment of inertia in pitch I_{yy} comparatively. Less C_{Mq} and large I_{yy} seems will lead FW and BWB less damping ratio of FW and BWB, compared to the CB.

However, due to the large wing area S and reference chord length \bar{c} of FW and BWB, those two elements could weaken the effect of low pitching damping ratio C_{Mq} and larger moment of inertia in pitch I_{yy} . Therefore, all these aspects make the short period damping ratio of FW and BWB as the same level as the CB. This similar result has also been found by Castro^[5].

Comparing the Table 7-6 and the short period mode requirement in Table 2-1, both the CB, FW and BWB could meet the Level 1 requirement.

7.4 Lateral-Directional static stability characteristics

7.4.1 Lateral static stability

$C_{l\beta}$ represents the amount of the lateral static stability, the requirement for directional static stability is:

$$C_{l\beta} < 0 \quad (7-3)$$

Figure 7-5 shows the lateral static stability of three configurations at different Mach numbers. With the tailless configuration, the lateral static stability of FW and BWB is much smaller than the conventional aircraft.

Comparatively, the relatively larger sweep angle of BWB makes the lateral static stability performance better than the FW. Another factor is the dihedral angle. For FW, there is 2° dihedral angle; For BWB, the outboard dihedral is 3° , which also increases the lateral static stability.

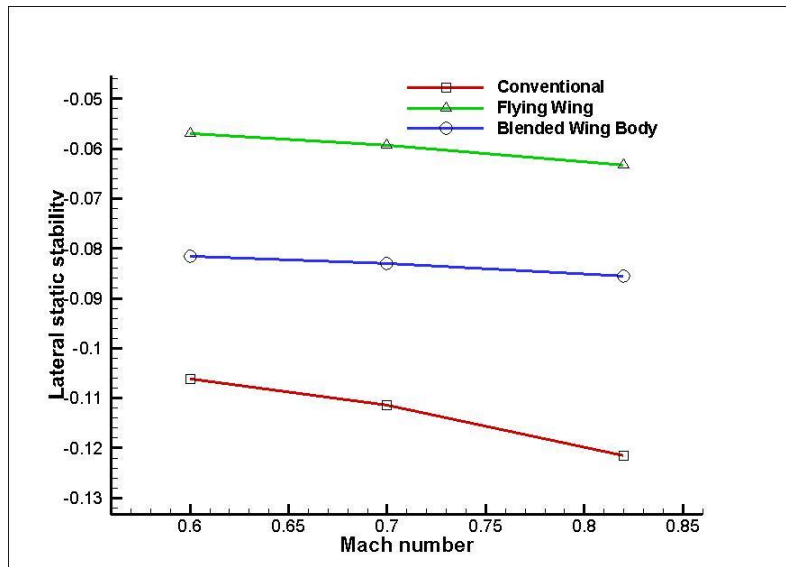


Figure 7-5 Lateral static stability

7.4.2 Directional Static stability

$C_{n\beta}$ represents the amount of the directional static stability, the requirement for directional static stability may be described as:

$$C_{n\beta} > 0 \quad (7-4)$$

The directional stability comparison is shown in Fig 7-6. The most notable difference is that no vertical tail installed on the FW and BWB in this research, therefore both FW and BWB configuration have less directional static stability than the conventional one.

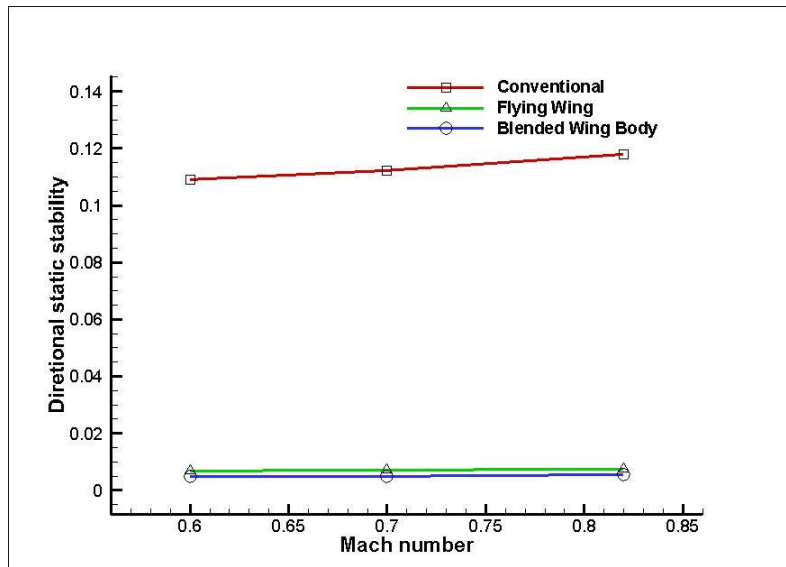


Figure 7-6 Directional static stability

7.5 Lateral-Directional dynamic stability Characteristics

7.5.1 Dutch roll mode

The Dutch roll mode is a damped oscillation, coupling the roll motion and sideslip motion. To some extent, it is equivalent to the longitudinal short period mode.

According to the calculation based on the current models, the Dutch roll mode of BWB is divergent, therefore only the CB and FW are compared. The Dutch roll damping ratio of the FW is smaller than the CB. Yaw damping derivative C_{nr} is the main parameter influencing the Dutch roll mode damping ratio. From the Table 6-7 to 6-9, it could be found that the yaw damping derivative C_{nr} of FW is -0.0110. For CB, the value is -0.1606. The less absolute value of C_{nr} will decrease the Dutch roll damping ratio. Another two factors are lateral static stability $C_{l\beta}$ and directional static stability $C_{n\beta}$. The $C_{l\beta}$ of FW is almost half of CB, however, there is dramatically decrease of $C_{n\beta}$ of FW. Therefore, the value of $|C_{l\beta}/C_{n\beta}|$ for FW are considerable larger than CB, which will cause the lower damping of Dutch roll mode.

Compared the result in Table 7-7 and requirement in Table 2-3, it could be found that the CB could meet the Level 2 requirement while FW only meet the requirement of Level 3.

Table 7-7 Dutch roll mode damping ratio and frequency

Configuration	Ma=0.60		Ma=0.70		Ma=0.82	
	ζ_d	ω_d (rad/s)	ζ_d	ω_d (rad/s)	ζ_d	ω_d (rad/s)
CB	0.0545	1.1974	0.0557	1.4125	0.0557	1.6946
FW	0.0011	0.5069	0.0037	0.5860	0.0054	0.6897

7.5.2 Roll mode

The roll mode is a non-oscillatory lateral characteristic.

According to the Equation 3-41, the roll mode time constant T_r is mainly decided by following factors: the moment of inertia in roll I_{xx} , roll damping derivative C_{lp} , wing span b and wing area S . The moment of inertia in roll I_{xx} of FW and BWB are larger than the CB and the less absolute value roll damping derivative C_{lp} , these two factors may lead larger T_r of FW and BWB than CB. However, the large wing area S and longer wing span b of FW and BWB also influence the roll mode time constant. The overall result of these factors makes the roll mode time constant of FW and BWB higher than CB.

Compare the result in Table 7-8 and the roll mode time constant requirement in Table 2-4, it could be found that both the three configurations could meet the Level 1 requirement.

Table 7-8 Roll mode time constants

Configuration	Ma=0.60	Ma=0.70	Ma=0.82
	T_r (s)	T_r (s)	T_r (s)
CB	0.4373	0.3580	0.2816
FW	0.5530	0.4560	0.3636
BWB	0.7850	0.6853	0.5337

7.5.3 Spiral mode

The spiral mode is a non-oscillatory lateral-directional characteristic. If this mode is stable, the time constant is irrespective; if the mode is unstable, since the response is quite slow that not severe divergence is acceptable.

Whether the value of $(C_{l\beta} C_{nr} - C_{lr} C_{n\beta})$ is positive or not determines whether the spiral mode is stable or unstable.

According to the aerodynamic derivatives calculated by AVL, the value of $(C_{l\beta} C_{nr} - C_{lr} C_{n\beta})$ are listed in Table 7-9. From the results, it is found that all the values are positive, which means all the three configurations are spiral mode stable.

Table 7-9 Spiral mode stability judgement

Configuration	Ma=0.60	Ma=0.70	Ma=0.82
	$C_{l\beta} C_{nr} - C_{lr} C_{n\beta}$	$C_{l\beta} C_{nr} - C_{lr} C_{n\beta}$	$C_{l\beta} C_{nr} - C_{lr} C_{n\beta}$
CB	0.00232	0.00220	0.00179
FW	0.00019	0.00019	0.00020
BWB	0.00025	0.00027	0.00030

7.6 Summary

The contents in this chapter could be summarised as follows:

1. For the longitudinal static stability characteristics, the CB is stable for both forward and aft CG position, while the FW is weak stable. Although there is unstable in the aft CG position, generally, the BWB has relatively larger stable criterion than the FW configuration.
2. For the longitudinal dynamic stability characteristics, there is no significant difference on short period mode between the three configurations. Although there is relatively low pitching damping ratio C_{Mq} and larger moment of inertia in pitch I_{yy} for FW and BWB, the larger wing area will benefit the FW and BWB

as the same level of short period damping ratio as CB. Due to the relatively large lift to drag ratio, the FW and BWB will have less drag than the CB, which causes slightly less damped in phugoid mode of FW and BWB.

3. For the lateral-directional static stability characteristics, there is no doubt that the conventional configuration has the best performance. Benefit from higher sweep angle and dihedral angle, the BWB is better than FW in lateral static stability. The directional derivatives of both BWB and FW are dramatically lower than the CB due to the lack of vertical tail.

4. For the lateral-directional dynamic stability characteristics, In terms of Dutch roll mode, the BWB is divergent. Comparing the FW and CB, the yaw damping derivative C_{nr} is quite low for FW, while the value of $|C_{l\beta}/C_{n\beta}|$ is quite larger, then the Dutch roll mode of FW is less damped than the CB. The roll mode time constant of BWB is larger than CB due to its less roll damping derivative and larger roll inertia moment. Both the three configurations are spiral mode stable.

In conclusion, the flying quality for the FW and BWB deteriorated mainly because of the tailless configuration.

Accordingly, three different solutions could be introduced to improve the flying quality of the FW and BWB in this research. The first one is to modify the configuration; the second one is varying the internal arrangements to change the mass distribution, and the last choice is adding advanced flight control system for better flying quality.

8 Parameter Influence on The Aerodynamic and Stability Characteristics of BWB Configuration

As the third part of the research work, the geometry parameter influence on the aerodynamics and stability characteristics are investigated.

It is of great interest to study the aerodynamic characteristics through varying wing geometry parameters. Due to the fact that the blended wing body aircraft is highly integrated, most of the geometry parameters are closely linked together. For the purpose to making direct comparison, only one of the geometric parameters varied at a time to identify the trend of influences. In this research, the changing parameter includes twist and sweep angle.

8.1 Influence of twist

The aim of this exercise is to access the influence of twist. Through suitable twist, the different shapes of lift distribution could be achieved. In this research, two different lift distribution shapes—elliptic and triangle shape are achieved by changing twist of several control sections. Then the influences of the induced drag and pitching moment are estimated.

The elliptic shape spanwise lift distribution follows the Equation 8-1:

$$\frac{C_{l(y)}C_{(y)}}{C_{ref}} = \sqrt{1 - \left(\frac{y}{b/2}\right)^2} \frac{C_{l(0)}C_{(0)}}{C_{ref}} \quad (8-1)$$

Where $C_{l(y)}$ means the local lift coefficient, $C_{(y)}$ is the local chord length, C_{ref} is reference chord length (usually the mean aerodynamic chord length), y is the spanwise position and b is the wing span.

The lift of whole wing surface could be calculated by integrating the lift of each section:

$$2 \int_0^{\frac{b}{2}} C_{l(y)}C_{(y)} dy = S_w C_L \quad (8-2)$$

Where, S_w is the whole wing area, and C_L is the lift coefficient of the whole airplane.

For the elliptic lift distribution, integrating the left part of Equation 8-2:

$$2 \int_0^{\frac{b}{2}} C_{l(y)} C_{(y)} d_y = 2 \times \frac{1}{4} \pi \times C_{l(0)} C_{(0)} \times \frac{b}{2} = S_w C_L \quad (8-3)$$

Then, the required lift coefficient at root chord for elliptic distribution is:

$$C_{l(0)} = \frac{4S_w C_L}{\pi b C_{(0)}} \quad (8-4)$$

The triangle spanwise lift distribution follows the Equation 8-5:

$$\frac{C_{l(y)} C_{(y)}}{C_{ref}} = \left(1 - \frac{y}{b/2}\right) \frac{C_{l(0)} C_{(0)}}{C_{ref}} \quad (8-5)$$

The lift of whole airplane could be calculated by Equation 8-6::

$$2 \int_0^{\frac{b}{2}} C_{l(y)} C_{(y)} d_y = 2 \times \frac{1}{2} \times C_{l(0)} C_{(0)} \times \frac{b}{2} = S_w C_L \quad (8-6)$$

Then, the required lift coefficient at root chord for triangle distribution is :

$$C_{l(0)} = \frac{2S_w C_L}{b C_{(0)}} \quad (8-7)$$

As illustrated in Table 6-3, the cruise lift coefficient C_L for blended wing body configuration equals to 0.226, the wing area S_w is 647 m², and the span is 52.76 m. The different lift distribution shapes are achieved by changing the twist of five control sections. From the above equations, the lift in each control section could be calculated for different lift distribution shapes, which are shown in Table 8-1 and Table 8-2.

Table 8-1 Elliptic lift distribution

Control section on spanwise position(m)	Local chord length C (m)	Local lift coefficient C_l
0	32.67	0.1081
8.84	14.29	0.2328
11.91	9.32	0.3381
15.99	6.37	0.4409
26.38	2.77	0.0000

Table 8-2 Triangle lift distribution

Control section on spanwise position(m)	Local chord length C(m)	Local lift coefficient C_l
0	32.67	0.1696
8.84	14.29	0.2579
11.91	9.32	0.3262
15.99	6.37	0.3427
26.38	2.77	0.0000

It could be found in the Table 8-1 and 8-2, there need more lift from the central body (0 m) to the first kink (8.84m) for triangle shape lift distribution. Hence, a relatively higher twist will be added for triangle shape in this area. In the outboard part, less lift is required for triangle distribution, and then a relatively less twist is needed. Figure 8-1 illustrates the twist on the spanwise for the two types of lift distribution.

In Figure 8-2 and Figure 8-3, the red line means the aim of elliptic or triangle lift distribution respectively, and the blue lines resembles the actual lift distribution after several loops iteration.

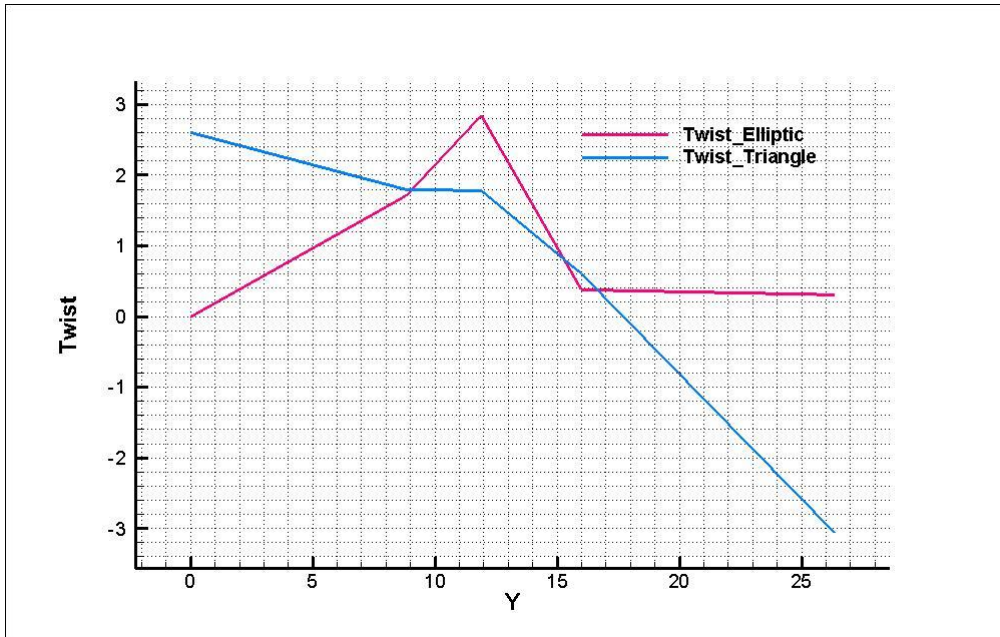


Figure 8-1 Twist angle through the spanwise

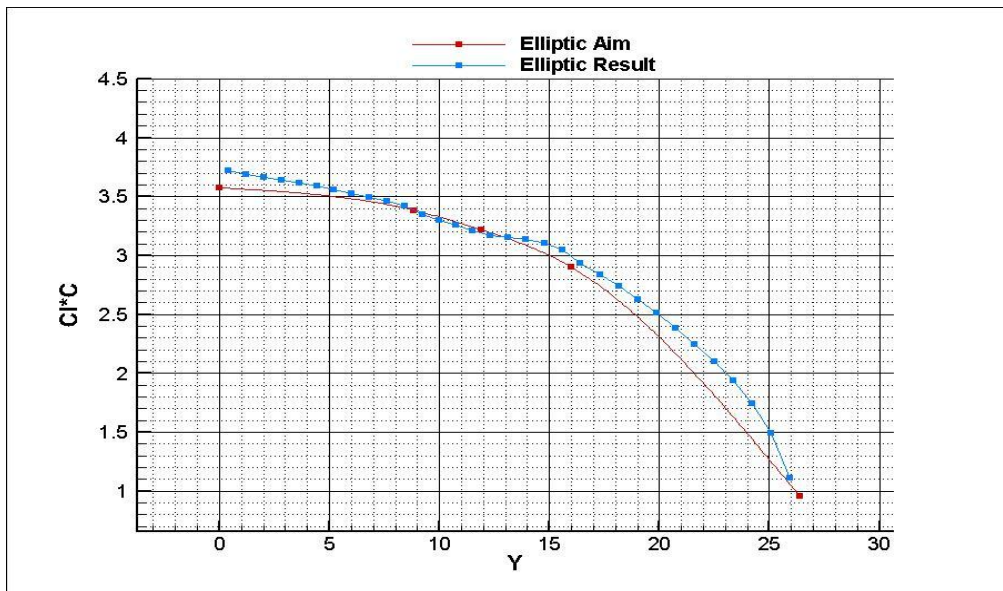


Figure 8-2 Elliptic lift distribution

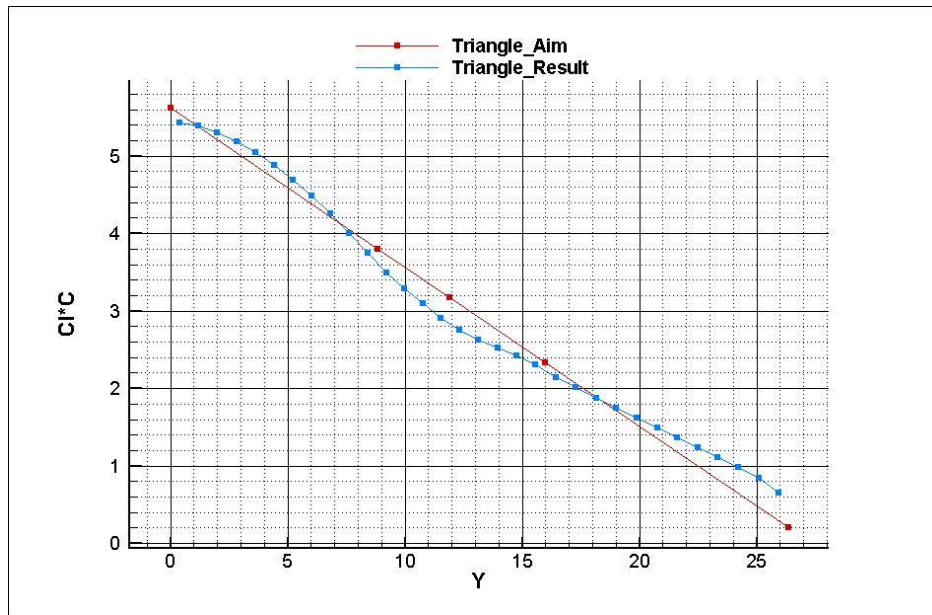


Figure 8-3 Triangle lift distribution

It is found in Table 8-3 that the induced drag is less for elliptic shape lift distribution. However, the pitching moment will inevitably be influenced. Taking one-quarter MAC as the reference point to calculate the pitching moment coefficient, it is clear that the wing with elliptic shape has larger negative pitching moment coefficient, which will bring the trend of nose-down pitching. The larger value of pitching moment in cruise, the more deflection angle of control surfaces for trim, meanwhile the more drag will be introduced consequently.

Since pitching moment is quite important for blended wing body aircraft, therefore changing twist will not only just pursuit the reduction of induced drag, the pitching moment should also be taken into consideration.

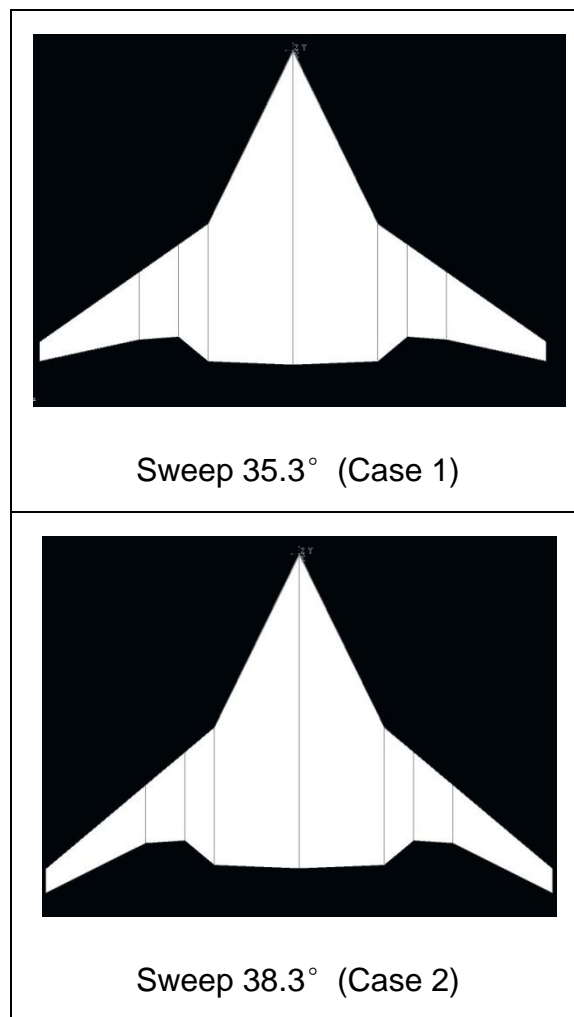
Table 8-3 Induced drag and pitching moment coefficient comparison

Configuration	Induced drag	Pitching moment coefficient
Twist for elliptic shape lift distribution	0.0040	-0.0751
Twist for triangle shape lift distribution	0.0052	-0.0254

8.2 Influence of sweep angle

In this section, the sweep angle of outboard part of blended wing body has been changed to estimate its effect. Inboard part, from the central root to the first kink position, keeps the same sweep angle as original.

The Case 1 is 35.3° degree sweep ,the Case 2 is 38.3° sweep, and the Case 3 is 41.3° sweep, as shown in Fig 8-4.



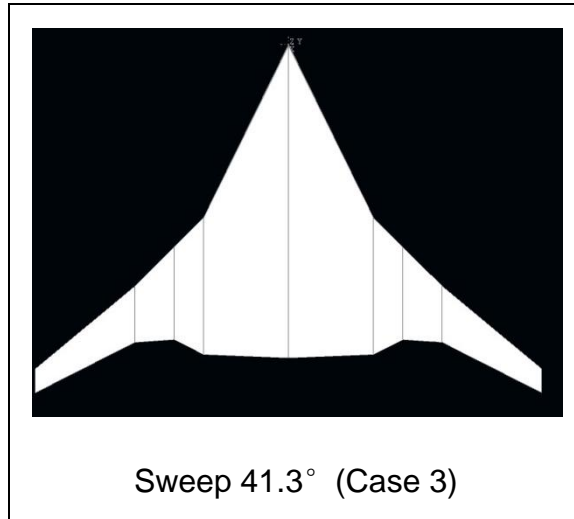


Figure 8-4 Different sweep angle models

The Table 8-4 lists the lift curve slope of these configurations. Apparently, the lift curve slope will be decreased as the increase of sweep angle. To some extent, that will lose the lift efficiency.

Table 8-4 Lift curve slope comparison (Unit: rad⁻¹)

Configuration	Ma=0.50	Ma=0.60	Ma=0.70	Ma=0.82
35.3° sweep angle	3.63	3.77	3.97	4.34
38.3° sweep angle	3.51	3.64	3.83	4.19
41.3° sweep angle	3.44	3.56	3.74	4.06

With the increase of sweep angle, the neutral point will move backward respectively as shown in Table 8-5.

Table 8-5 Neutral point comparison (Unit: MAC)

Configuration	Ma=0.50	Ma=0.60	Ma=0.70	Ma=0.82
35.3° sweep angle	0.328	0.331	0.337	0.348
38.3° sweep angle	0.339	0.343	0.349	0.361
41.3° sweep angle	0.351	0.356	0.362	0.375

Another advantage brought by increasing sweep is enhancing the lateral static stability. With the increase of sweep angle, the value of lateral static derivative will be decreased and that means lateral static stability will be enhanced. There is an reduction about 0.007 of lateral stability derivative from sweep 35.3° to 38.3° , while the trend is not so obvious from sweep 38.3° to 41.3° with only 0.003 reducing.

Table 8-6 Lateral stability derivative comparison

Configuration	Ma=0.50	Ma=0.60	Ma=0.70	Ma=0.82
35.3° sweep angle	-0.0732	-0.0744	-0.0760	-0.0790
38.3° sweep angle	-0.0801	-0.0816	-0.0830	-0.0855
41.3° sweep angle	-0.0834	-0.0848	-0.0867	-0.0899

8.3 Summary

From the above calculation and analysis, some conclusions could be summarised:

1. According to the classical theory, the elliptic shape lift distribution could minimise the induced drag. Once the airfoil of each wing section has been fixed, the elliptic spanwise lift distribution could be achieved through arranging the suitable twist on each wing section. The twist will not only influence the lift distribution, but also affect the pitching moment. Especially for the tailless configuration, it is very important to keep the pitching moment in an acceptable criterion. Therefore, the twist should be carefully balanced between achieving the lift distribution shape and controlling the pitching moment.
2. Increasing the sweep angle of the outboard part, on the one hand, will make the neutral point moves back ward. On the other hand, the lateral stability characteristics are also improved. However, the lift slope will be decreased as increasing the sweep angle.

In general, the design of blended wing body is a really complicated job, since its high integrated configuration, the whole blended wing body is really a “sensitive”

configuration. Even the smallest detail change will affect the aerodynamic and stability performance of whole body. Therefore, it is essential to carefully consider many aspects to give an optimised solution.

9 Improve Static Margin Through Changing Parameters

This chapter describes an iteration process that changing parameters to improve the static margin as well as keep the same zero pitching moment at the design point. Due to the highly integration characteristics of blended wing body, geometry parameters, stability and aerodynamic characteristics are closely linked.

9.1 Introduction

As presented in Table 7-4, there is a one particular situation that the blended wing body with full fuel and no payload is unstable. The static margin is -2.35%. Several methods could be chosen to improve the static margin, for example, rearrange the mass package to move the CG forward, or modify the configuration to move the neutral point aft ward. In this chapter, the configuration is modified by changing the sweep angle to improve the static margin.

However, since blended wing body is an integrated system, the modified sweep angle will inevitably affect the pitching moment.

Taking the weight of the full payload and half of the fuel as the calculation point, the weight is 141,136 kg and the CG position of 21.308 m. For the purpose of keeping the same zero pitching moment at the same position, a new twist distribution has been arranged to achieve this aim.

9.2 Iteration steps

Three steps are included during the iteration process:

Step 1: change the sweep angle to improve the longitudinal stability;

Step 2: check the trim condition of the new configuration with the previous twist.

Step 3: rearrange the twist to make sure the zero pitching moment at the design point.

9.2.1 Step 1: change sweep angle

The static margin is determined by the relative position of the neutral point and CG, as described in Equation 7-2.

The sweep angle will influence the position of the neutral point and the CG. The neutral point will move aft as the sweep angle increases. At the same time, the CG will also move aft. Therefore, whether the static margin will be enhanced or not, depends on which one will move “faster”.

Two kinds of sweep angle: 41.3 degrees and 43.3 degrees are estimated, which is shown in Figure 9-1. The corresponding position of the neutral point and the CG are listed as Table 9-1. It is clear that with 41.3 degrees sweep back, the neutral point moves at the same rate of the CG, and the overall result makes the static margin is zero; with 43.3 degrees sweep back, the neutral point moves back to 38.60% while the CG moves to 37.54%, therefore, the static margin is 1.06%.

Since 43.3 degrees sweep angle achieves performance by improving the stability margin, it will be chosen for the new configuration.

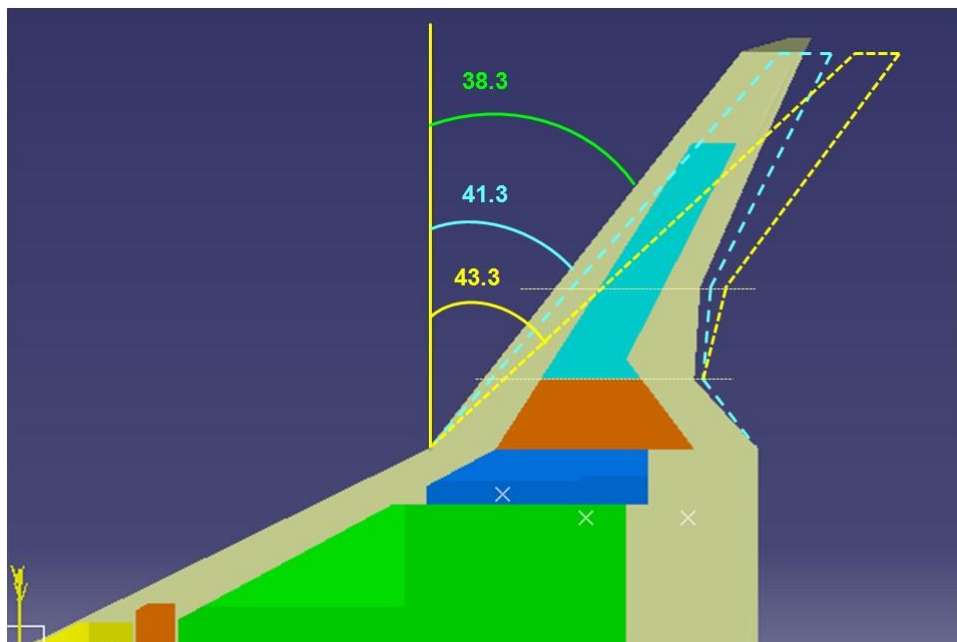


Figure 9-1 Three sweep angles

Table 9-1 Comparison of NP and CG of different sweep angles

	38.3 ° sweep	41.3 ° sweep	43.3 ° sweep
Neutral point	36.10% \bar{c}	37.70% \bar{c}	38.60% \bar{c}
CG (No payload full fuel)	38.45% \bar{c}	37.70% \bar{c}	37.54% \bar{c}
Static Margin	-2.35% \bar{c}	0.00% \bar{c}	1.06% \bar{c}

9.2.2 Step 2: check trim ability

After changing the sweep angle from 38.3 to 43.3 degree, there is a slightly change on the zero lift pitching moment coefficient C_{M_0} , which is shown in Table 9-2.

Table 9-2 Comparison of zero lift pitching moment coefficient

	38.3 ° sweep	43.3 ° sweep
C_{M_0}	0.01736	0.01720

After changing the sweep angle to 43.3 degree, the ability to trim the aircraft should be checked. Four extreme conditions have been checked for trim: two CG positions (forward CG and aft CG) and two velocity conditions (Mach 0.2 and Mach 0.82).

The comparison of forward CG and aft CG for two different sweep angles has been shown in Table 9-3.

Table 9-3 Forward CG and Aft CG of different sweep angle

	38.3 ° sweep	43.3 ° sweep
Forward CG	18.08% \bar{c}	16.34% \bar{c}
Aft CG	38.68% \bar{c}	37.54% \bar{c}

The horizontal axis of Figure 9-2 is the angle of attack, while the vertical axis is the elevator deflection angle. Same definition is also used in Figure 9-3 to Figure 9-5.

The Figure 9-2 shows that the elevator deflection angle of different sweep angles. The reference point is forward CG, while the Mach number is 0.82. Generally, there will be a larger elevator deflection angle for the new configuration than the previous one, at the same angle of attack. The reason is that with a larger sweep angle, the new configuration will be much more stable. Since stability and handling quality are a pair of conflicting characteristics. If the airplane is too stable, it will be more difficult to control, and vice versa. That is why the more elevator deflection angle is needed for the new configuration with 43.3 degrees sweep angle.

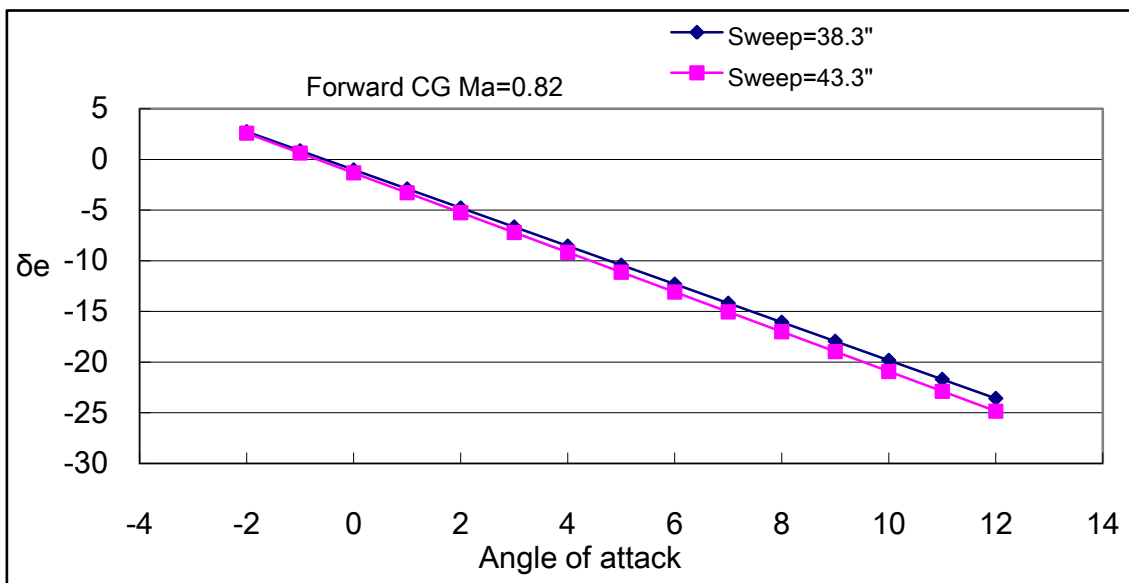


Figure 9-2 Elevator deflection angle (Forward CG, Ma=0.82)

There is significant change in Figure 9-3 that ,after changing sweep angle from 38.3 degrees to 43.3 degrees, the slope changes from positive(blue line) to negative (red line),which indicates that the airplane becomes stable after changing the sweep angle.

In Figure 9-3, where the reference point is the aft CG and flight condition is at Mach number 0.82, there will be less elevator deflection angle for the new

configuration with 43.3 degree sweep. For the aft CG, the elevator has to deflect upward to balance the nose up pitching moment.

The pitching moment of the whole airplane could be described by Equation 9-1

$$C_M = C_{M_0} - C_L(X_{np} - X_{cg}) \quad (9-1)$$

Where C_{M_0} is the zero lift pitching moment coefficient, C_L is the lift coefficient, X_{np} is the position of the neutral point and X_{cg} is the position of centre of gravity.

Since the static margin of the new configuration has been improved, so the value of $(X_{np} - X_{cg})$ is larger. Therefore, less noses up pitching moment C_M for the new configuration is needed for trim, and so less elevator deflection is needed.

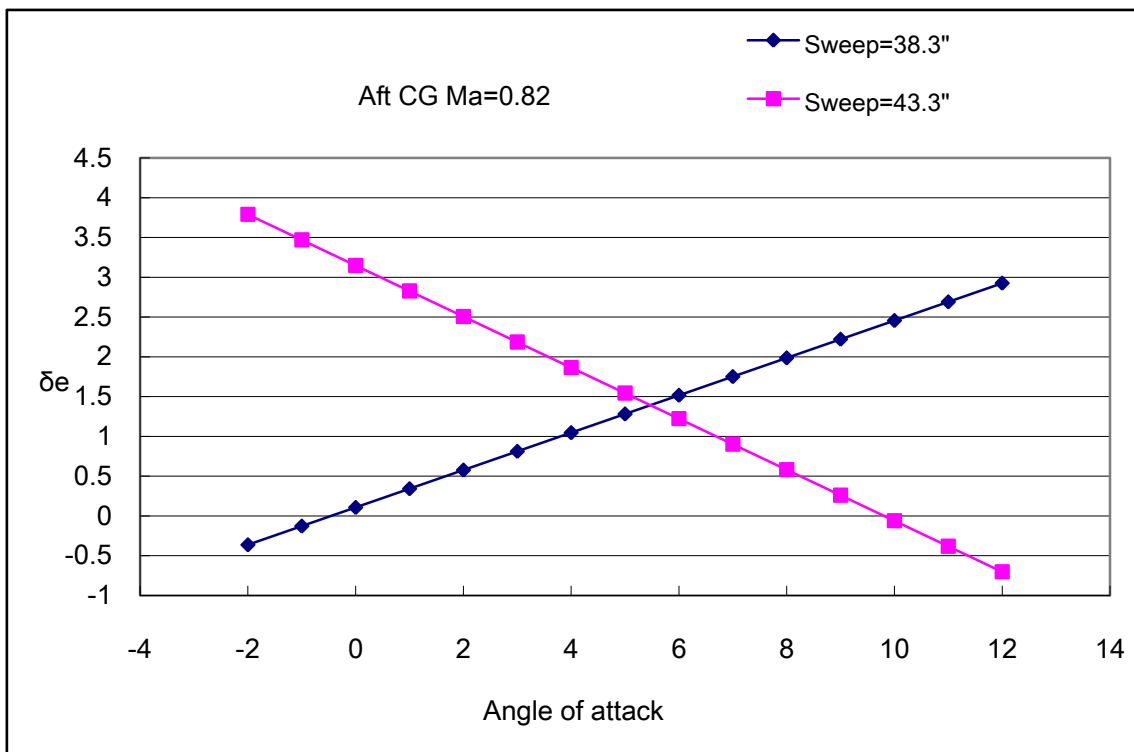


Figure 9-3 Elevator deflection angle (Aft CG, Ma=0.82)

The Figure 9-4 shows the elevator deflection angle for different sweep angles. The reference point is forward CG, while the Mach number is 0.2. The elevator

will be deflected to a larger degree for the new configuration with 43.3 degree sweep, if both of them are at same angle of attack.

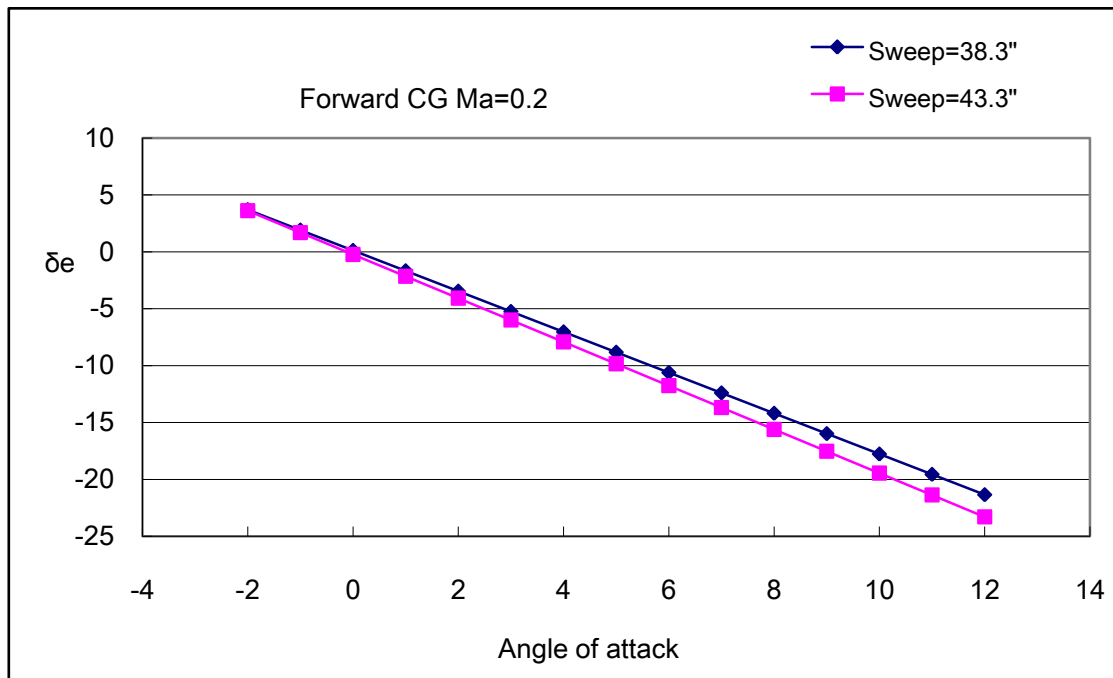


Figure 9-4 Elevator deflection angle (Forward CG, Ma=0.2)

For Figure 9-5, the slopes of the two lines are positive, which means that the neutral point moves forward than the CG and both the two configurations are unstable, then $X_{np} - X_{cg} < 0$ in this situation. According to Equation 9-1, since the neutral point of new configuration is more close to the CG, the value of $-(X_{np} - X_{cg})$ will be less and then less pitching moment C_M need to be trimmed. Therefore, less deflection angle is needed for the new configuration with 43.3 degree sweep.

For the angle of attack from -2° to 12° , the deflection angle is less than 14 degree, which still lies in the acceptable criteria. So, the airplane still could be trimmed.

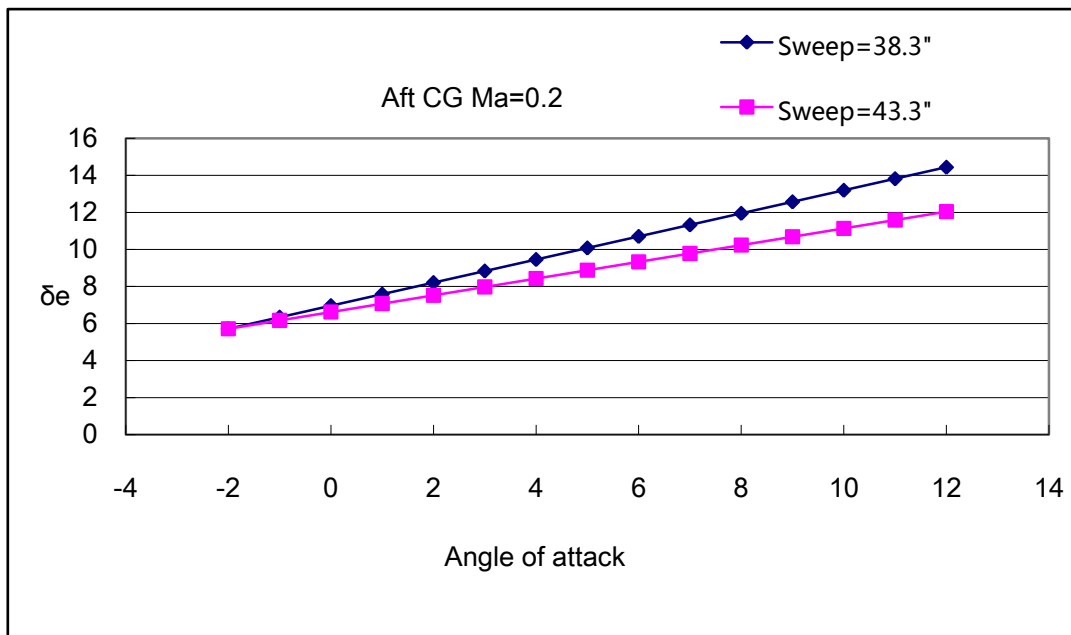


Figure 9-5 Elevator deflection angle (Aft CG, Ma=0.2)

In general, after moving the sweep angle from 38.3° to 43.3° , there is no significant influence on the trim condition. Even in the most severe condition ,the elevator deflection angle still under the 25° limitation.

9.2.3 Step 3: arrange the twist

Taking the full payload and half of the fuel as the design point, the CG position has been changed with the sweep angle, as well as the pitching moment coefficient, which are shown in Table 9-4. In order to make sure the pitching moment coefficient at the same position (21.308 m) is zero for the new configuration, the zero lift pitching moment that should be added the value of 0.0079.

Table 9-4 Sweep influence on CG position and pitching moment coefficient C_M

	38.3 ° sweep	43.3 ° sweep
CG(full payload , half fuel)	21.30	20.98
C_M	0.0000	-0.0079

There are two different ways to change the C_{M_0} . The first is to replace the airfoil. As illustrated in Chapter 8-4, the reflex camber airfoil will add a positive value to C_{M_0} . The second choice is to rearrange the twist. Adding a negative twist in the outboard wing section will bring a positive value to C_{M_0} , and vice versa.

Since there are six control sections along the span, a variety of combinations can achieve this aim. For example, twist one single section with large angle, or twist several sections with relative small angle. In order to keep the lift distribution a smooth shape, finally, the decision is keeping the same twist in the centre body, while several outboard control sections are twisted, as shown in Table 9-5.

Table 9-5 Comparison of the twist

Spanwise (m)	0.00	2.04	8.84	11.91	15.99	26.38
Original Twist(°)	2.5	3.0	2.0	3.5	2.5	-6.5
New Twist (°)	2.5	3.0	2.0	2.0	1.5	-7.0

Inevitably, the spanwise lift distribution is affected, which is shown in Figure 9-6. The red line is the lift distribution with original twist and the green line is the lift distribution with the new twist. The elliptic distribution is the blue line. Compared with the original twist, less lift is produced in the outboard section because of the negative twist angle added. Therefore, the lift distribution of the new twist is far away the elliptic distribution, and so the induced drag is increased. The comparison of induced drag is listed in Table 9-6.

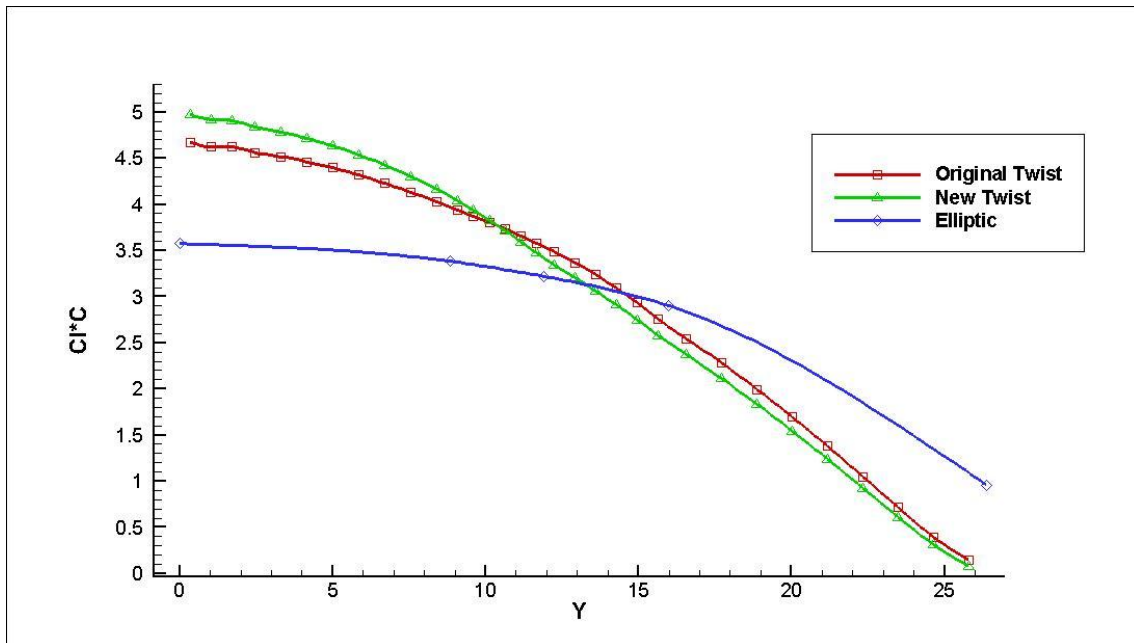


Figure 9-6 Spanwise lift distribution of different twists

Table 9-6 Comparison of induced drag

Configuration	Induced drag
43.3 ° sweep with original twist	0.0051
43.3 ° sweep with new twist	0.0054

9.3 Other concerns

Increasing the sweep angle improves the longitudinal static stability; however, some other aspects of aerodynamic characteristics may be deteriorated. For example, there is a decrease in the lift curve slope when increasing the sweep angle, as illustrated in Table 9-7.

Table 9-7 Lift curve slope (Unit: rad⁻¹)

Configuration	Ma=0.5	Ma=0.6	Ma=0.7	Ma=0.82
38.3 ° sweep	3.51	3.64	3.83	4.19
43.3 ° sweep	3.37	3.49	3.66	3.97

It can be seen during the iteration process that, in order to improve the static margin by increasing the sweep angle, several characteristics have been sacrificed.

9.4 Summary

In this chapter, a special case has been explored in an attempt to improve the static stability by changing geometry parameters. Then, the pitching moment has been influenced. In order to make sure the pitching moment refer to the design point still keeps zero for the new configuration, a new twist is arranged. Inevitably, the lift distribution and induced drag will be affected, and the lift characteristic is deteriorated.

The iteration shows that the blended wing body aircraft is really a complex configuration. Geometry parameters, stability and aerodynamic characteristics are closely linked. Only a slightly change for one parameter will influence others. Therefore, the design of blended wing body aircraft is quite complicated due to the close coupling of parameters.

10 Conclusions and Suggestions

This aim of this chapter is the main conclusions of the whole research work as well as some suggestions for the future work.

10.1 Conclusions of present work

The research process could be summarised as follows:

Based on the same requirements, three different options--conventional, flying wing and blended wing body aircraft are provided. Utilising simple calculation methods, the aerodynamic characteristics are compared on the three configurations. With the estimated mass and CG data (from Ref ^[3]), the comparison on stability characteristics of the three configurations are made. The effects of geometric parameters on aerodynamic and stability characteristics are investigated. Then, the static margin of BWB has been improved through modifying geometry parameters.

The main findings through the research could be concluded as:

1. From the aerodynamic point of view, the highly integrated wing and body configuration benefits the flying wing and blended wing body less lift coefficient needed for cruise as well as less drag produced. The cruise lift to drag ratio of BWB will increase about 31% compared to the CB configuration, that value is 24% for FW configuration.
2. The BWB configuration seems to be better balanced in aerodynamic and stability. According to the present configuration and internal mass arrangement, the aft CG of BWB is unstable. Except this particular condition, the BWB configuration has extended static margin than the FW configuration in other conditions.
3. In terms of longitudinal dynamic stability, the FW and BWB has relatively higher lift to drag ratio than CB, therefore, the phugoid mode damping ratio is less than the CB due to the lower drag. For the short period mode, although the pitching damping ratio C_{Mq} of FW and BWB are much less than the CB, however, the larger wing area and longer mean aerodynamic chord

length plays an important role to make the short period damping ratio of FW and BWB the same level as CB.

4. In terms of lateral-directional dynamic stability, the most significant differences lie in the fact that the Dutch roll mode of BWB is divergent, while the Dutch roll damping ratio and frequency of FW is much less than the CB. Less yaw damping derivative C_{nr} and large $|C_{l\beta} / C_{n\beta}|$ for BWB and FW are the two main contributors cause the result.
5. According to the classical theory, the elliptic span wise lift distribution is best for minimise the induced drag. This could be achieved by arranging the suitable twist on several control sections. However, that twist arrangement may lead to too much nose down pitching moment, which will cause more difficulty for trim. Since trim is quite a big issue for tailless configuration, therefore, it is of vital importance to find the balance point to take both the lift distribution and pitching moment into consideration.
6. The increasing of the sweep angle will make the neutral point moves backward. At the same time, the centre of gravity will also have the same trend. Therefore, whether the static margin could be improved depends on which moves faster. Meanwhile, the lift curve slopes will inevitable be decreased as the increase of sweep angle.
7. The blended wing body configuration is really very sensitive to changing geometry parameter. Several parameters are closely linked together. Once one parameter changes will lead to a chain reaction. This feature makes the design and optimisation of Blended Wing Body a quite complicated work.

10.2 Limitation of present research

The limitations of present research could be present as follows:

1. From the models point of view, both of the three configuration options are not “well designed”, which means the general configuration, the airfoil section, the twist as well as other aerodynamic aspects still need in-depth design and optimise in the future work. Besides, the mass, CG and inertia data are also based on the prediction data. Therefore, those results in this

research might not comprehensively represent the characteristics of flying wing or blended wing body.

2. From the aerodynamic point of view, the aerodynamic forces calculation could be more accurate. In terms of the lift calculation, it is calculated by AVL. To be frank, AVL may not be suitable in the transonic region. The present calculation of lift curve slope is really large. In terms of drag prediction, the engine and nacelle drag are neglected. Besides, the drag estimation method may not be sufficiently enough. Although there are so many drawbacks, nevertheless, it provides a quick and convenient method to obtain the aerodynamic data.
3. From the stability calculation point of view, the aerodynamic derivatives are provided by AVL using some reduced order equations, which may not correctly reflect the real situation during the calculation. That may also cause some errors on the stability calculation because the dynamic stability calculation may be very sensitive to these derivatives data.

10.3 Suggestions of future work

Accordingly, some suggestions for future work could be provided.

1. Fulfil the design of three configuration options to make a better comparison, especially on the aerodynamic design and internal mass distribution arrangement. That further work will bring more accurate data for analysis and comparison on the three different configurations.
2. Since only AVL is used in this research, several other codes based on Vortex-Lattice Method could be used to make a direct comparison. Besides, more advanced computational approaches will benefit the calculation for aerodynamic data. If further work requires more accurate estimation, some high fidelity codes such as Euler or Navier-Stokes based methods may be a better choice.
3. Only the “clean” configuration has been considered, for the take-off or landing these kinds of complex configuration can be investigated in the future work.

4. At present, few parameters have been estimated as twist and sweep angle. Further research could pay more attention on investigating the impact of a wide range of parameters like wing span, kink position....
5. Since there are so many parameters closely linked together in blended wing body aircraft, it is of great interest to research the optimisation of those parameters. Some optimisation algorithm could be added during the iteration process.

REFERENCES

1. AVIC 4th GDP Report, "*FW-11 Specification*". Cranfield University ,2012
2. Howard Smith, "*DES 1100/1: Advanced Blended Wing Body High Capacity Airliner BW-11 Project Specification*". Cranfield University. 2011
3. Zhang Jin, "*The layout effect on Flying Wing Airliner's CG Range and Inertial Loads*". MSc Thesis. Cranfield University. Jan 2012
4. Lippisch, Alexander, "*The delta wing—history and development*". Iowa State University Press, AMES. 1981
5. H V DE Castro, "*Flying and Handling Qualities of a Fly-by-Wire Blended Wing Body Civil Transport Aircraft*". PhD Thesis. Cranfield University .Dec 2003
6. Richard M. Wood, Steven X.S. Bauer, "*Flying Wings/Flying Fuselages*". AIAA 2001-0311, 39th AIAA Aerospace Sciences Meeting & Exhibit, Reno, 8-11 January 2001.
7. Bolsunovsk, A.L., Buzoverya, N.P., Gurevich, B.I., Denisove, V.E., Dunaevsky, A.I., Shkadov, L.M., Sorin, O.V., Udzhuhu, A.J. and Zhurihin, J.P., "*Flying Wing-Problems and Decisions*". Aircraft Design 4(2001) 193-219, Pergamon, 2001.
8. Liebeck, R.H., "*Design of the Blended Wing Body Subsonic Transport*". Journal of Aircraft, Vol.41, No.1, pp.10-25, 2004.
9. Liebeck, "*Design of the Blended-Wing-Body Subsonic Transport*". AIAA-2002-002
10. Northrop Grumman. www.northropgrumman.com. (Website Reference)
11. Tjoetjoek Eko Pambagjo , "*Aerodynamic Design of a Medium Size Blended Wing Body Airplane*". AIAA-2001-0129

12. Roman, D., Alen, J.B., Libeck, R.H, “*Aerodynamic Design of the Blended-Wing-Body Subsonic Transport*”. AIAA Paper 2000-4335
13. Eppler, Richard, “*Airfoil Design and Data*”. Springer-Verlag. 1990
14. Charles D. Harris, “*NASA Supercritical Airfoils: A Matrix of Family-Related Airfoils*”. NASA Technical Paper 2969. 1990.
15. Henne, P.A, “*Applied Computational Aerodynamics*”. AIAA Education Series. 1990
16. Paul F. Roysdon, Mahmood Khalid, “*Lateral-Directional Stability Investigation of a Blended-Wing-Body*”. AIAA- 2010-9167
17. N Qin, A vavalle, A Le Moigne, M Laban , K Hackett, Weinerfelt, “*Aerodynamic Studies for Blend Wing Body Aircraft*”. AIAA-2002-5448.
18. N Qin, A Vavalle, A Le Moigne , M Laban, K Hackett , P Weinerfelt, “*Lift Distribution for Blended Wing Body Aircraft*”. Journal of Aircraft. Vol.42.No.2 2005.
19. Northrop, “*The Development of All-wing Aircraft. 35th Wilbur Wright Memorial Lecture*”. The Royal Aeronautical Society Journal. Vol 51, pp.481-510, 1947
20. M.V. Cook., “*Flight Dynamics Principles*”. Elsevier Aerospace Engineering Series. Arnold Press. First Edition 1997
21. Military Specification, “*Flying Qualities of Piloted Airplanes*”. MIL-F-8785C
22. Salman A. Ansari, Kevin Knowles, Rafal Zbikowski, “*Insectlike Flapping Wings in Hover Part 2: Effect of Wing Geometry*”. Journal of Aircraft. Vol.45, No 6. 2008
23. Lv Xinbo, “*Aerodynamic Characteristics and Flying Qualities Research of Large Aircraft with Box-wing Configuration*”. MSc Thesis. Cranfield University. 2010

24. Ralph Paul, William L. Garrard, "*Dynamics and control of tailless aircraft*". AIAA-97-3776. AIAA Atmospheric Flight Mechanics Conference, August 11-13, New Orleans, Louisiana, 1997
25. Drela, M. Youngren, H., "*AVL 3.26 User Primer*". MIT Aero & Astro. Aug, 2010
26. Tornado. <http://www.redhammer.se/tornado/> (Website Reference)
27. D. Howe, "*AVT-AVD 9603. Estimation of Drag Coefficient at Initial Design Work*". Cranfield University
28. W. H. Mason, "*FRICTION USERMAN*". Virginia Tech Aerodynamics and Design Software Collection. <http://www.dept.aoe.vt.edu>. (Website Reference)
29. F. M. White, "*Viscous Fluid Flow*", New York: McGraw-Hill, pp. 589-590, 1974
30. E. J. Hopkins and M. Inouye, "*An Evaluation of Theories for Predicting Turbulent Skin Friction and Heat Transfer on Flat Plates at Supersonic and Hypersonic Mach Numbers*", AIAA Journal Vol. 9 No. 6, pp. 993-1003, June 1971
31. T. Cebeci and P. Bradshaw, "*Momentum Transfer in Boundary Layers*". McGraw-Hill, New York, pp. 187, 1977
32. SURFACES., "*Vortex Lattice Module User Manual. Great OWL Publishing. Engineering Software*". August 2009.
33. Barnes Mc Cormic, "*Aerodynamics, Aeronautics, and Flight Mechanics*". John Wiley & Sons. Second Edition. 1995
34. Ira Herbert Abbott, Albert Edward Von Doenhoff, "*Theory of Wing Sections*". Dover Publications. 1959.
35. James C. Sivells, "*Experimental and Calculated Characteristics of Three Wings of NACA 64-210 and 65-210 Airfoil Sections With and Without 2 ° Washout*". AIAA Technical Note 1422.

36. A. Deperrois, *“Modal Analysis and Experimental Validation”*. Feb, 2011.
<http://xflr5.sourceforge.net/xflr5.htm> (Website Reference)
37. Daniel P. Raymer, *“Aircraft Design: A Conceptual Approach”*. AIAA Education Series. 4th Edition. 2006
38. Karl Nickel, Michael Wohlfahrt, *“Tailless Aircraft in Theory and Practice”*. The Bath Press. 1994
39. B. Mialon, T. Fol, C. Bonnaud, *“Aerodynamic Optimization of Subsonic Flying Wing Configurations”*. AIAA Paper 2002-2931
40. Erickson, L.L., *“Panel Methods—An Introduction”*. NASA TP 2995, Dec. 1990
41. Portsdam, M.A., Page, M.A., and Liebeck, R.H., *“Blended Wing Body Analysis and Design”*. AIAA Paper 97-2317, 1997
42. Jupp, J., *“Wing Aerodynamics and the Science of Compromise”*. Aeronautical Journal, Vol. 105, No. 1053, pp. 633-641, 2001.
43. Sergey Peigin, Boris Epstein, *“CFD Driven Optimization of Blended Wing Body Aircraft”*. AIAA Paper 2006-3457
44. Mark Drela, Harold Youngren, *“XFOIL 6.9 User Primer”*. MIT Aero & Astro, 30 Nov 2001.
45. Ben Smiley, Daniel Williams, Dave Pike, *“G1F-BWB Aerodynamics Specialist Technical Report”*. AVDASI 3/4-UB2008F, Bristol University. 2008
46. Donlan, C. J., *“Current Status of Longitudinal Stability”*. NACA RM L8A28, 1948
47. ESDU 76003 *“Geometrical Properties of Cranked and Straight Tapered Wing Planforms”*
48. ESDU 95010, *“Computer Program for Estimation of Spanwise Loading of Wings with Camber and Twist in Subsonic Attached Flow”*.

49. ESDU 93015 , "*Program for Calculation of Maximum Lift Coefficient of Plain Aerofoils and Wings at Subsonic Speeds*".
50. Wilkinson, K.G., Shepperd, J.A.H and Lyon, H.M, "*The Longitudinal Response of Tailless Aircraft*". RAE Report Aero 2060. Royal Aircraft Establishment, Farnborough, July 1945.
51. Louis V. Schmidt., "*Introduction to Aircraft Flight Dynamics*". AIAA Education Series., pp.334-354, 1998.
52. W.H.Mason, "*Applied Computational Aerodynamics*". Virginia Tech, Chapter 6, pp 19-27, 1998
53. Fang Zhenping, Chen Wanchun, Zhang Shuguang. "*Aircraft Flight Dynamics*". Beijing University of Aeronautics and Astronautics. pp.288:325, 2010

APPENDICES

The appendices contain about three parts. The first part introduces the author's contribution to the Group Design Project. The second part presents the details of AVL simulation. The third part shows how to use ESDU to calculate the neutral point.

Appendix A Group Design Project

During the Group Design Project, the author has been involved in the aerodynamic group. Together with my team member-Tong Chao^[4], we have finished the conceptual design of FW-11 and calculate the aerodynamic forces and derivatives. Besides, as a member of management team, the author cooperates with Zhang Jin, monitoring the design progress.

A.1 Airfoil chosen and twist arrangement

Based on the wing geometry, there are four control sections along the spanwise. The first one locates at the symmetric plane with spanwise coordinate $Y=0(m)$, the second one locates at the first kink position with spanwise coordinate $Y=8.4(m)$, the third one locates at the plane with spanwise coordinate $Y=14(m)$, and the last one is the wingtip position with $Y=32(m)$. For each control section, the coordinates of leading point is shown in Figure Appendix -1.

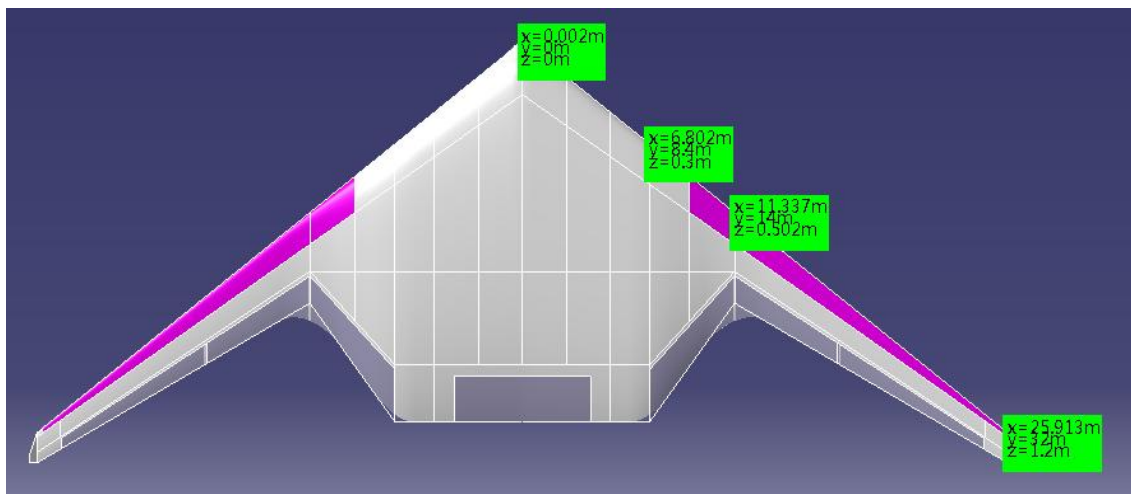


Figure Appendix -1 Wing sections and start point of each section

As illustrated in Figure Appendix -2, the inboard part locates from the first control section $Y=0(m)$ to the second control section $Y=8.4(m)$.

From the arrangement point of view, the inboard part contains flight deck, cabin, and cargo. From the structural point of view, the thickness of inboard part should change smoothly from the front spar (14% chord length) to rear spar (80% chord length). From the aerodynamic point of view, the inboard part will not only just contain the cabin and cargo, it will also a large lift generating surface.

Take those aspects in to consideration, the basic airfoil chosen for this part is NASA Symmetric SC airfoil. In order to suit the internal arrangement, the thickness to chord ratio is modified to 16.4% to provide sufficient internal space.

The outboard part locates from the third control section $Y=14(m)$ to the last section $Y=32(m)$. The outboard part contains some fuel tanks. Besides, the outboard part should make good balance between the lift and pitch moment. Thinking of these requirements, the airfoil chosen for this part is NASA RC-SC2 airfoil. Firstly, the thickness is 10% which is enough for containing the fuel tanks

and other equipments. Secondly, it is a kind of supercritical airfoil which will have good aerodynamic performance. Thirdly, the zero lift pitch moment is -0.02, which is acceptable.

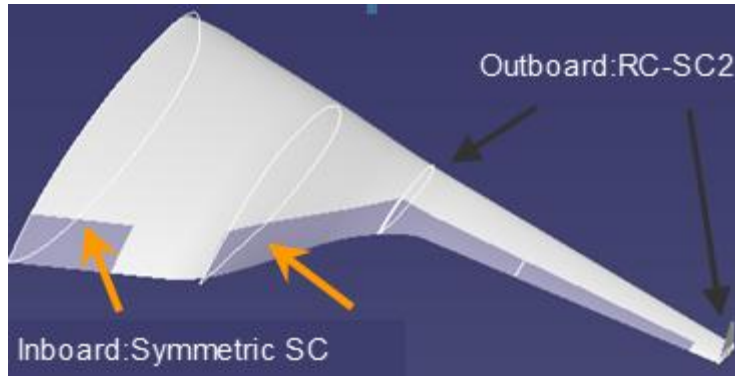


Figure Appendix -2 Inboard and outboard airfoil

According to the internal arrangement, the inboard part of FW-11 is with 16.4% thickness ratio, and smoothly changes to the outboard with 10% thickness ratio. In Figure Appendix -3, the horizontal axis is the ratio of spanwise, and the right vertical axis is the thickness ratio. The red line in Figure Appendix -3 indicates the thickness ratio variation along the spanwise.

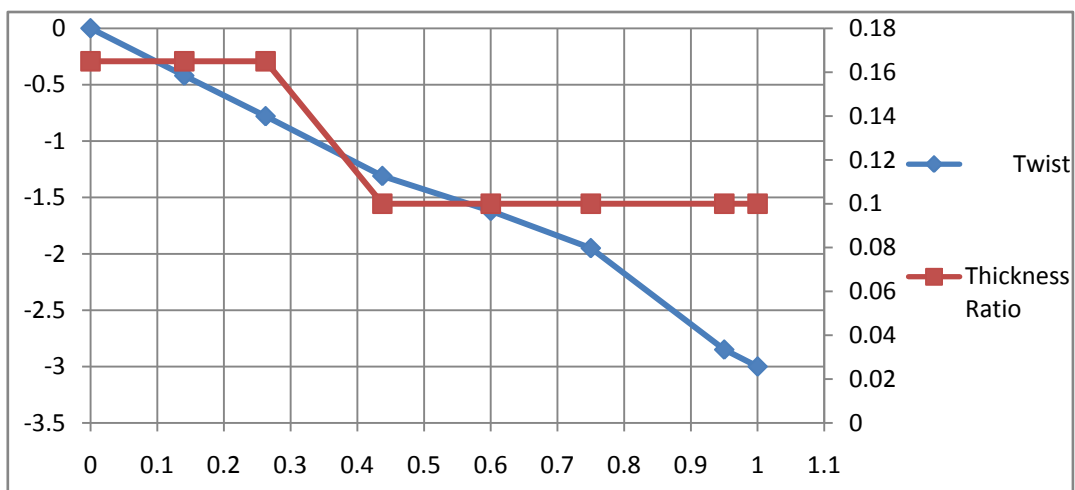


Figure Appendix -3 Spanwise twist and thickness ratio variation

For the aim of minimise the induced drag, the twist should be carefully arranged. With the help of “design” function of AVL, several twist arrangement have been tested. Finally, the twist arrangement is shown in the blue line of Figure Appendix -3. Figure Appendix -4 shows the spanwise lift distribution, it could be found that the shape is nearly the elliptic, which will benefit reducing the induced drag.

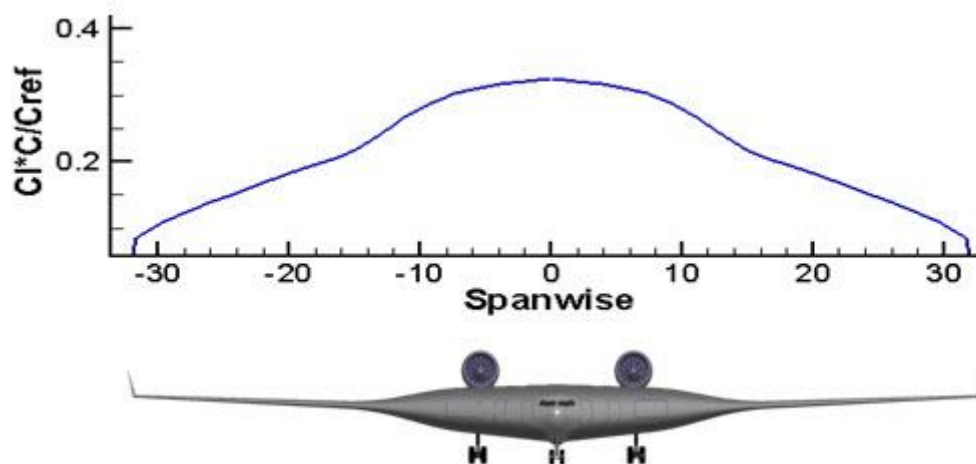


Figure Appendix -4 Spanwise lift distribution

A.2 Lift and drag estimation

During the cruise condition, the airplane is with clean configuration. The lift could be calculated by AVL software, and the drag prediction method has been introduced in the previous chapter.

During the take-off and landing condition, the airplane deploys the high lift devices. According to the specification in Appendix Ref^[1], the flap deflecting angle is 25° for take-off condition and 35° for landing.

The lift and drag increments due to the flap deflection are estimated by the method introduced by Jan Roskam in Appendix Ref^[2].

In terms of the three-dimensional lift increments contributed by flap deflection, firstly, the lift increments due to two-dimensional flap deflection could be predicted. Then, three main factors should be considered. One is the three-dimensional effective factor should be considered. The other is the ratio of flap length to span. The third is ratio of wing lift curve slope to wing airfoil lift curve slope. Taken these factors into consideration, the three-dimensional lift increments contributed by flap deflection could be predicted.

The drag increments caused by flap deflection could be decomposed into three parts: the flap profile drag increment, the induced drag caused by flap and the interference drag.

Using the above method, Table Appendix A-1 lists the results.

Table Appendix A-1 Lift and drag coefficient increment due to flap^[4]

Condition	Flap deflection angle	Lift coefficient increment	Drag coefficient increment
Take-off	25°	0.165	0.00595
Landing	35°	0.288	0.01586

Therefore, the drag polar of take-off condition is:

$$C_D = 0.0144 + 0.0561C_L^2$$

The drag polar for landing condition is :

$$C_D = 0.0243 + 0.0595C_L^2$$

Appendix B AVL model description

In order to run the AVL simulation, there are three different types of input files. The compulsory `.avl` file describes the geometry of the airplane. Two optional files: `.mass` file contains the mass information while `.run` file defines the simulation condition.

The sample `avl` file is listed as follows:

```
-----# Startline of avl file #-----  
  
BWB  
0.0 | Mach  
0 0 0 | iYsym iZsym Zsym  
648.102 14.71 52.760 | Sref Cref Bref  
21.308 0.000 0.000 | Xref Yref Zref  
0.00 | CDp (optional)  
SURFACE | (keyword)  
BWB  
#Nchord Cspace [ Nspan Sspace ]  
20 1.0  
INDEX | (keyword)  
21543 | Lsurf  
YDUPLICATE  
0.0  
SCALE  
1.0 1.0 1.0  
TRANSLATE  
0.0 0.0 0.0  
ANGLE  
0.000 | dAinc  
SECTION  
0.0028 0.0000 0 32.6700 2.50 3 0  
AFIL 0.0 1.0
```

a1.dat
design
twist1 1
CONTROL
elevator 1.0 0.9188 0. 0. 0. 1
SECTION
4.1603 2.0400 0.4916 28.5120 3 8 0
AFIL 0.0 1.0
a2.dat
design
twist2 1
CONTROL
elevator 1.0 0.9133 0. 0. 0. 1
SECTION
18.0342 8.8400 1.083 14.2900 2.0 6 0
AFIL 0.0 1.0
a3.dat
design
twist3 1
CONTROL
elevator 1.0 0.8695 0. 0. 0. 1
CONTROL
flap 1.0 0.8695 0. 0. 0. +1
SECTION
20.4657 11.9100 1.32 9.3199 3.5 6 0
AFIL 0.0 1.0
SYMISC.dat
design
twist4 1
CONTROL
flap 1.0 0.7992 0. 0. 0. +1
SECTION
23.6815 15.9900 1.42 6.3700 2.0 9 0
AFIL 0.0 1.0
SC0010.dat

```

design
twist5 1
CONTROL
flap 1.0 0.7242 0. 0. 0. +1
CONTROL
aileron -1.0 0.7242 0. 0. 0. -1
SECTION
31.8801 26.3800 1.697 2.7700 -6.50 6 0
AFIL 0.0 1.0
SC0010.dat
design
twist6 1
CONTROL
slat -1.0 -0.1 0. 0. 0. +1
CONTROL
aileron -1.0 0.75 0. 0. 0. -1
SURFACE | (keyword)
BWB_Fin
#Nchord Cspace [ Nspan Sspace ]
20 1.0
INDEX | (keyword)
21543 | Lsurf
YDUPLICATE
0.0
SCALE
1.0 1.0 1.0
TRANSLATE
0.0 0.0 0.0
ANGLE
0.000 | dAinc
SECTION
31.8801 26.3800 1.697 2.7700 0.000 6 0
AFIL 0.0 1.0
naca64012.dat
CONTROL

```

rudder 1.0 0.45 0.0.0.1

SECTION

33.8301 26.3800 4 0.82 0.000 6 0

AFIL 0.0 1.0

naca64012.dat

CONTROL

rudder 1.0 0.45 0.0.0.1

-----# Endline of avl file #-----

The *mass* file gives the unit of length, mass and time. Then, the value of gravity and air density are provided. The sample mass file is listed as follows:

-----# Startline of mass file #-----

BWB

Dimensional unit and parameter data.

Mass & Inertia breakdown.

Names and scaling for units to be used for trim and eigenmode calculations.

The Lunit and Munit values scale the mass, xyz, and inertia table data below.

Lunit value will also scale all lengths and areas in the AVL input file.

#

Lunit = 1.0000 m

Munit = 1.0000 kg

Tunit = 1.0000 s

Gravity and density to be used as default values in trim setup (saves runtime typing).

Must be in the unit names given above (i.e. m,kg,s).

g = 9.81

rho = 0.38

Mass & Inertia breakdown.

x y z is location of item's own CG.

lxx... are item's inertias about item's own CG.

#

x,y,z system here must be exactly the same one used in the .avl input file

(same orientation, same origin location, same length units)

#

mass x y z lxx lyy lzz lxy lxz lyz

141136 20.143 0.00 0.00 7716710 5575448 12818763 0 541783 0

-----# Endline of mass file #-----

The *run* file not only defines the flight simulation condition ,the control surface deflection could also be defined in the *run* file.

The sample *run* file is listed as follows:

-----# Startline of run file #-----

Run case 1: BWB

alpha -> *CL* = 0.22600

beta -> *beta* = 0.00000

pb/2V -> *pb/2V* = 0.00000

qc/2V -> *qc/2V* = 0.00000

rb/2V -> *rb/2V* = 0.00000

aileron -> *aileron* = 0.00000

elevator -> *Cm pitchmom* = 0.00000

rudder -> *rudder* = 0.00000

alpha = 2.13442 deg

beta = 0.00000 deg

pb/2V = 0.00000

qc/2V = 0.00000

rb/2V = 0.00000

CL = 0.22600

CDo = 0.200000E-01

bank = 0.00000 deg

elevation = 0.00000 deg

heading = 0.00000 deg

Mach = 0.82

velocity = 246 m/s

density = 0.38 kg/m³

grav.acc. = 9.8000 m/s²

turn_rad. = 0.00000 m

load_fac. = 1.00000


```

X_cg    = 20.912    m
Y_cg    = 0.00000    m
Z_cg    = 0.020    m
mass    = 141136    kg
Ixx     = 7716710    kg-m^2
Iyy     = 5575448    kg-m^2
Izz     = 12818763    kg-m^2
Ixy     = 0          kg-m^2
Iyz     = 0          kg-m^2
Izx     = 520735    kg-m^2
visc CL_a = 0.00000
visc CL_u = 0.00000
visc CM_a = 0.00000
visc CM_u = 0.00000

```

-----# End of run file #-----

Once the three files are well defined, the AVL could be operated .Then, the aerodynamic forces and derivatives could be provided.

Appendix C ESDU for Neutral Point Estimation

ESDU 70011 introduces the method for lift-curve slope and aerodynamic centre position estimation for wings in inviscid subsonic flow. There is an attached computer program(ESDUpac A7011) could be used directly to estimate the .The input and output file format of the program are listed in Figure Appendix C-1—and Figure Appendix C-2 respectively.

<i>Variable name in program</i>	<i>Notation in Item</i>	<i>Comments</i>
CHAR1 CHAR2 CHAR3	- - -	The first 3 lines of the input data file are read as text and are written on the output file. Each line may contain 72 characters and must end with a carriage return. A blank line must be entered if no text is available.
NM	-	Number of Mach numbers (≤ 50)
MVALS(1), ..., MVALS(I), ..., MVALS(NM)	M	Values of Mach number ($0 \leq M < 1$)
NA	-	Number of aspect ratios (≤ 50)
AVALS(1), ..., AVALS(I), ..., AVALS(NA)	A	Values of aspect ratios
SN	n	Specifies n^{th} chord line for definition of Λ_n ($0 \leq n \leq 1$)
NLN	-	Number of sweep angles (≤ 50)
LNVALS(1), ..., LNVALS(I), ..., LNVALS(NLN)	Λ_n	Values of sweep angles
NLDA	-	Number of taper ratios (≤ 50)
LVALS(1), ..., LVALS(I), ..., LVALS(NLDA)	λ	Values of taper ratios ($0 \leq \lambda < 1$)
D or R	-	Enter D or R to specify lift-curve slope per degree or per radian

Figure Appendix C-1 Input data format and comments of A7011

<i>Program Heading</i>	M	A	n	Ln	Taper	Beta A	A tan Lh	dCL/da	xb/cbb	xb0/cr
<i>Notation in Item</i>	M	A	n	Λ_n	λ	βA	$A \tan \Lambda_{1/2}$	$dC_L/d\alpha$	\bar{x}/\bar{c}	\bar{x}_0/c_r

Figure Appendix C-2 Output data heading of A7011

According to the BWB configuration, the input file is listed as follows:

#Startline of input file--

BWB

DATA FOR INPUT IN EXAMPLE OF SECTION 6 OF ITEM No. 70011

PLANFORM a

9

0.2 0.3 0.4 0.5 0.6 0.7 0.8 0.82 0.85

1

4.305

0.25

1

36.87

1

0.1274

R

#Endline of input file----

After running the program, the neutral point could be calculated base on the input geometry and flow condition information. The output data are listed as follows:

OUTPUT DATA

<i>M</i>	<i>A</i>	<i>n</i>	<i>Ln</i>	<i>Taper</i>	<i>BetaA</i>	<i>AtanLh</i>	<i>dCL/da</i>	<i>xb/cbb</i>	<i>xb0/cr</i>
.200	4.305	.250	36.87	.127	4.22	2.45	3.596	.333	.644
.300	4.305	.250	36.87	.127	4.11	2.45	3.644	.334	.645
.400	4.305	.250	36.87	.127	3.95	2.45	3.716	.336	.646
.500	4.305	.250	36.87	.127	3.73	2.45	3.814	.339	.648
.600	4.305	.250	36.87	.127	3.44	2.45	3.948	.343	.650
.700x	4.305	.250	36.87	.127	3.07	2.45	4.133	.349	.654
.800x	4.305	.250	36.87	.127	2.58	2.45	4.396	.358	.661
.820x	4.305	.250	36.87	.127	2.46	2.45	4.464	.361	.663
.850x	4.305	.250	36.87	.127	2.27	2.45	4.582	.365	.666

Where the number of xb/cbb (\bar{x}/\bar{c}) is the value of the distance from the leading edge of aerodynamic mean chord to the aerodynamic centre divided by the aerodynamic mean chord length.

Note that the “x” warns that the high free-stream Mach number. That indicates the result may not be reliable. However, at this conceptual design state, since

the ESDU is a quick method to estimate the data, it is assumed the results predicted by ESDU are reliable. Further work could use high fidelity codes to get more accuracy data.

APPEXDIX REFERENCES

1. AVIC 4th GDP Report, “*FW-11 Specification*”. Cranfield University 2012
2. Roskam, J, “*Airplane design / by Jan Roskam. Part VI, Preliminary calculation of aerodynamic, thrust and power characteristics*”, Ottawa, Kansas, Roskam Aviation and Engineering Corporation, 1987.
3. ESDU 70011, “*Lift-curve slope and aerodynamic centre position of wings in inviscid subsonic flow*”, Engineering Sciences Data Unit, 2000.
4. Tong Chao, “*Effect of layout options on flying wing airliner structural loads*”, MSc Thesis,Cranfield University,2012